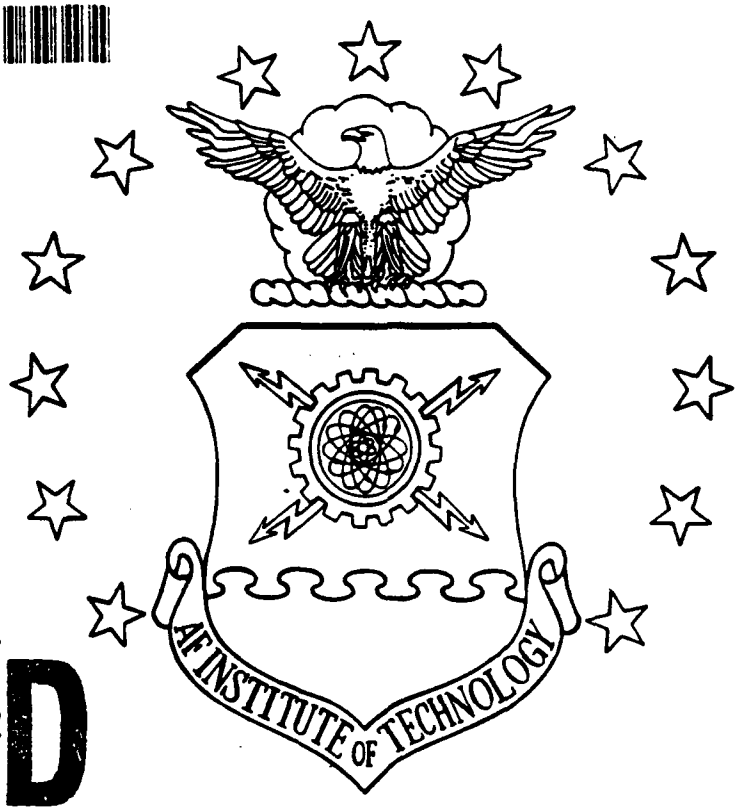

DEPARTMENT OF THE AIR FORCE

AIR UNIVERSITY

AIR FORCE INSTITUTE OF TECHNOLOGY

Wright-Patterson Air Force Base, Ohio

AFIT/GE/ENG/91D-56

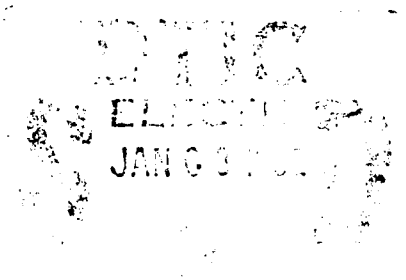

ELECTROMAGNETIC SCATTERING FROM DIELECTRIC PYRAMIDAL TIPS

THESIS

Albert D. Tyson, IV, Captain, USAF

AFIT/GE/ENG/91D-56

AFIT/GE/ENG/91D-56

ELECTROMAGNETIC SCATTERING FROM DIELECTRIC PYRAMIDAL TIPS

THESIS

Presented to the Faculty of the School of Engineering
of the Air Force Institute of Technology
Air University
in Partial Fulfillment of the
Requirements for the Degree of
Master of Science in Electrical Engineering

Albert D. Tyson, IV, B.S.E.E.
Captain, USAF

December 1991

Approved for public release; distribution unlimited

Acknowledgements

A thesis is more than a document. A thesis represents the thought processes involved in solving a problem and the knowledge gained by investigating a phenomenon. I have been fortunate enough to be engaged in this thesis process, and my life will forever be changed.

I would like to thank the many people who made this thesis possible. First, I would like to extend my appreciation to the United States Air Force for giving me the opportunity to gain this knowledge.

I would like to extend my appreciation to Dr (Captain) Philip Joseph. I consider myself fortunate to have had the opportunity to work with him. His advice and insight during the course of this thesis effort, and during my time at AFIT, were invaluable.

I would like to thank the AFIT faculty and staff for their professionalism. I want to thank the staff of the AFIT anechoic chamber, Captain Dan Mullinix, and Mr Bob Lindsay, for having the chamber "up and running" whenever I needed it. I also want to thank all of the men at the AFIT model shop, who took my ideas and gave them form.

I want to express my gratitude and thanks to my family. I want to thank my mother and father, who taught me to pursue every educational opportunity. I want to thank my children, TJ and Alison, who were understanding when I couldn't be disturbed because "daddy's doing homework."

Finally, I want to recognize the sacrifices and the support of my wife Joni. Words cannot express my gratitude at the way she held us together as a family. She read the books and played the games when I could not. Without her support, this thesis would not have been possible.

Albert D. Tyson, IV

Table of Contents

Page

List of Figures

Abstract

This thesis investigated the electromagnetic scattering from conducting, lossless dielectric, and lossy dielectric (absorber) pyramids. The backscatter from pyramids was measured and a time gate was applied to isolate the scattering from the tips. The measured results were compared to predictions from an approximate Uniform Theory of Diffraction (UTD) solution for scattering by a dielectric corner. The accuracy of the corner diffraction solution was found to be dependent on the polarization of the incident electric field. The accuracy of the UTD solution was also dependent on the aspect angle to the pyramid: the UTD solution gave a nominally correct answer within 25 degrees of nose-on incidence; at other angles the accuracy was better or worse depending on field polarization. The accuracy of the corner diffraction solution when applied to a dielectric was primarily dependent on the tip angle of the pyramid, with more acute angles giving the least accurate results. At incidence angles near nose-on to absorber pyramids, scattering from internal inhomogeneities was the dominant scattering mechanism. At incidence angles away from nose-on, the UTD solution provided reasonably accurate results. The approximate UTD dielectric corner solution was found to be accurate for many engineering applications.

ELECTROMAGNETIC SCATTERING FROM DIELECTRIC PYRAMIDAL TIPS

I. Introduction

1.1 Background

The electromagnetic scattering from a perfectly-conducting corner (such as a vertex of a cube or the tip of a pyramid) is a canonical problem for which there is yet no rigorous high-frequency solution. The scattering from a lossy dielectric corner is a much more complex problem and one of great practical interest. One example is the tip scattering of the pyramidal radar absorber material used to line the walls of modern anechoic chambers. The radar absorbing material typically consists of a dielectric foam which has been carbon-loaded to provide a loss mechanism. Several studies have been made on the subject of electromagnetic scattering by pyramidal radar absorber [1, 2, 3, 4]. These efforts have done much to increase our knowledge of the scattering mechanisms of pyramidal absorber.

The cross-section of a wall of pyramid absorber is shown in Figure 1. Some of the expected ray mechanisms are illustrated: these include rays which penetrate the absorber, rays which scatter from the tip, and rays which reflect from the pyramid surfaces. DeWitt [1,5] made

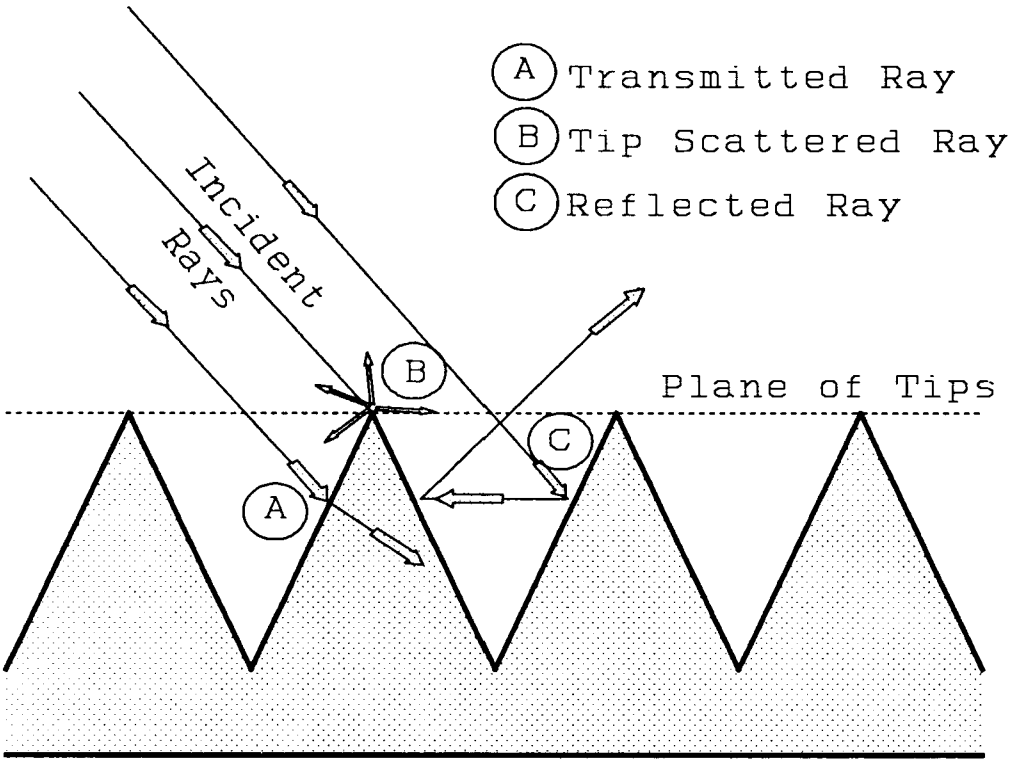

Figure 1. Cross-Section of Pyramidal Absorber Wall

extensive measurements on pyramidal absorber and concluded that tip scattering is the dominant scattering mechanism as either the incident or scattering direction approaches the plane of the tips. Joseph [2] developed an approximate solution to predict the scattering from a lossy dielectric corner. Joseph's approximate solution is based upon the Uniform Theory of Diffraction (UTD), and is a computationally efficient closed-form solution. Joseph applied this solution to the specific case of scattering by absorber pyramids. The validity of his solution was tested in several absorber scattering experiments [2, 3]. These experiments included backscatter measurements from a single

absorber pyramid illuminated by a plane wave, bistatic measurements from a section of a wall of absorber pyramids illuminated by a plane wave, and bistatic measurements from a section of a wall of absorber pyramids illuminated by the edge of a compact range reflector. Overall, the agreement between measurements and predictions provide a general validation of the theory. The weakest agreement was for the case of backscatter from a single absorber pyramid. This may have been because the backscattered signal was too weak to be accurately measured, the tip scattering was not the dominant mechanism in the orientations measured (near nose-on incidence), or the theory behind the approximate solution does not work well around the nose-on orientation.

Joseph [2] modeled the absorber pyramid as a homogeneous, lossy dielectric material. However, the absorber is likely an inhomogeneous material [4,5], due to manufacturing processes used to load the absorber material with carbon. Such inhomogeneities would give rise to an additional scattering mechanism not modeled in [2] (see Figure 2). The solution of [2] predicts the weakest backscattered signal from the pyramidal tip in the region of nose-on incidence. Thus, the weak agreement in the case of near nose-on backscatter may have been due to the presence of much stronger scattering from inhomogeneities.

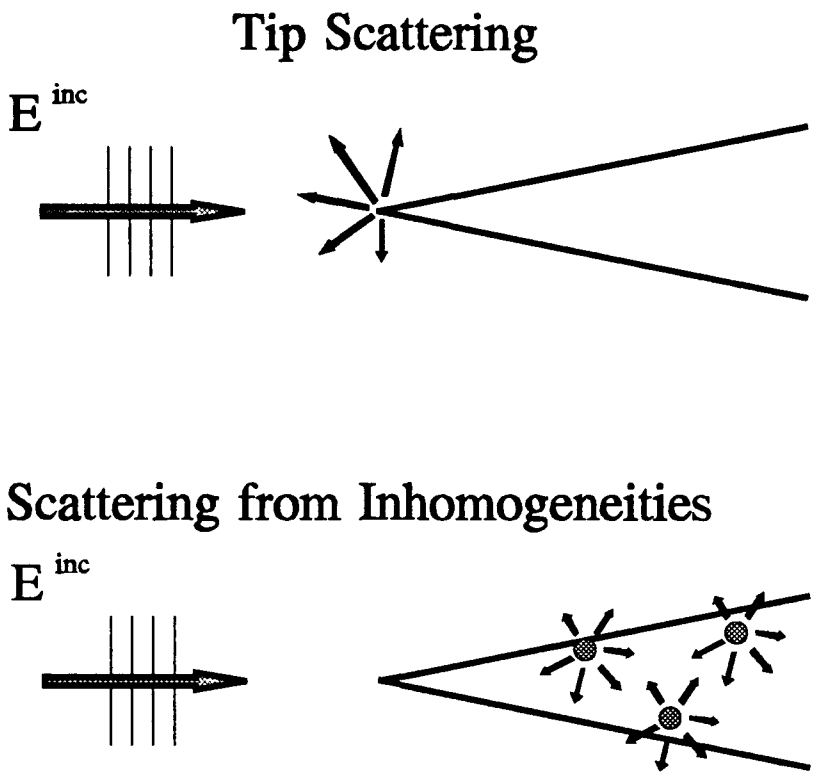

Figure 2. Scattering Mechanisms in Absorber Pyramid

1.2 Literature Search

Geometrical Optics (GO) was developed to describe the propagation of electromagnetic waves at high frequency. GO applies to isotropic, lossless, inhomogeneous media, and assumes electromagnetic energy travels along properly directed rays. GO accounts for incident, reflected and refracted (or transmitted) rays; however, GO fails to account for diffraction. Kouyoumjian and Pathak [6] developed the UTD, which corrects this shortcoming. UTD considers a set of diffracted rays in addition to the incident, reflected, and transmitted rays of GO.

Kouyoumjian and Pathak's solution predicts the diffraction by an edge in a perfect electrically conducting (PEC) surface. The geometry of a two-dimensional conducting wedge is shown in Figure 3. GO predicts discontinuous fields at the incident shadow boundary (ISB) and reflection shadow boundary (RSB), since the incident field and reflected field stop abruptly at these locations, respectively. The UTD provides a diffracted field which radiates from the edge, causing the total field to be continuous at both shadow boundaries and to be non-zero in region III.

Sikta, *et al* [7] presented and evaluated an extension to the UTD for the case of diffraction by a corner of a flat PEC plate. This solution is based upon an evaluation of the equivalent edge currents that would exist in the absence of the corner. The corner diffraction coefficient is then obtained by appropriately (but empirically) modifying the result. This extension successfully predicted the fields diffracted by a corner for several plate structures.

Burnside, Wang and Pelton [8] extended the work of Sikta [7] to the case of a corner formed by the intersection of three (or more) edges. A corner of a cube exemplifies this type of corner. However, the solution developed in [8] still assumed a PEC scatterer.

Burnside and Burgener [9] developed a UTD solution for edge diffraction by a thin, lossless dielectric slab. This solution is based on a modification of the UTD solution for

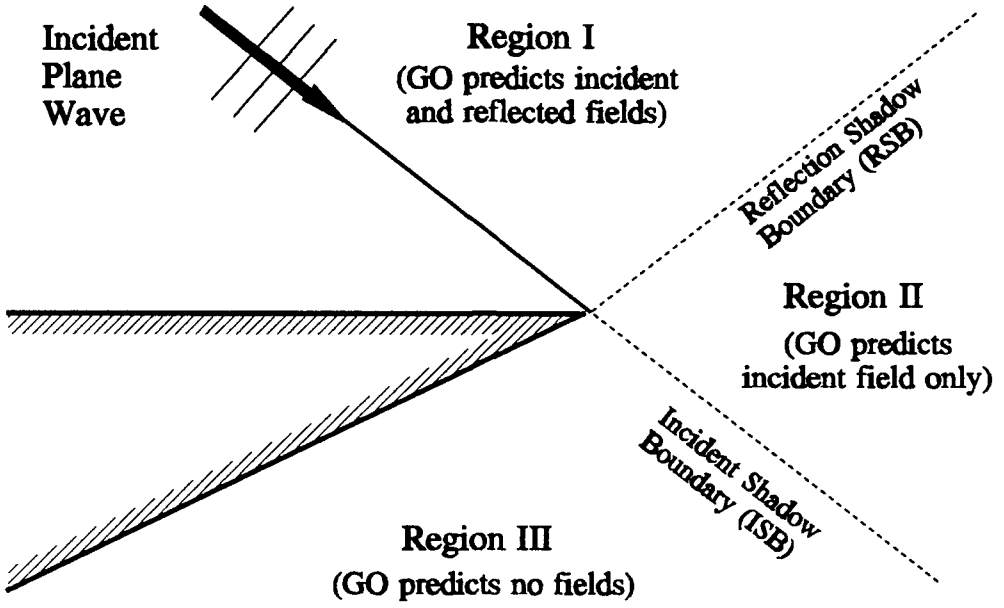

Figure 3. Shadow Boundaries Associated with a Conducting Wedge.

a conducting half-plane. In the case of a lossless dielectric, the shadow region is illuminated by a transmitted field; thus, the diffracted field of [9] was chosen to eliminate the discontinuity between incident and transmitted fields instead of the discontinuity between the incident and zero fields. Likewise at the RSB, the diffracted field of [9] must eliminate a discontinuity which differs from that of a PEC edge, due to the non-perfect reflection of the dielectric.

DeWitt [1] extended the work of [9] for edge diffraction by a two-dimensional lossy dielectric wedge.

The dielectric wedge solution was based on the GO field discontinuities, similar to the process used in [9]. However, due to the complexity of the GO field itself for the lossy dielectric wedge, DeWitt made two simplifying assumptions. The first assumption was that the reflection from an illuminated face could be approximated by the initial external (Fresnel) reflection coefficient. The second assumption eliminated the portion of the diffracted field associated with the GO discontinuity at the ISB, since the vanishing thickness of the wedge near the edge would lead to a transmitted field that gradually increases to the strength of the incident field as an observer approaches the ISB from region III.

Joseph [2], using these same two simplifying assumptions, developed a solution for diffraction by a lossy dielectric corner. As mentioned earlier, comparisons between predictions and experiment had good overall agreement [2]. However, it was postulated that scattering from inhomogeneities could be dominant in the near nose-on region.

Several studies raise the possibility that scattering from inhomogeneities may indeed occur. DeWitt and Burnside [5] found that panels of absorber material scatter from different internal regions. They also found (by physically cutting open some absorber panels) that electrical properties varied rather abruptly in some regions. The

scattering centers formed by these scattering centers were found to appear randomly within the absorber, with the net effect of increasing the panel scattering level.

Brumley [4] also examined the topic of absorber inhomogeneity. Three-dimensional imaging techniques were used to graphically depict the inhomogeneities within and among several panels of pyramidal absorber. Scattering variations of up to five decibels were found among pyramids on the same panel; scattering amplitude variation of over twelve decibels were found between different panels. These findings make it clear that the experimental results based on a single absorber pyramid are critically dependent on the individual pyramid used.

1.3 Problem Statement

As stated earlier, the dielectric corner diffraction solution showed poor agreement with experimental measurements for the case of a single absorber pyramid [2]. One possibility is that the dielectric corner solution is invalid. A second possibility is that the backscattered signal from the absorber pyramid was too weak to be measured accurately. A third possibility is that the absorber pyramid used may have had significant inhomogeneities which dominated the return signal. In any case, further study is warranted.

This study proposes to check the validity of the dielectric corner solution. This will begin with

experimental verification of the PEC corner diffraction solution itself, since the dielectric solution is based on the PEC solution. Next, the calculations will be compared with measurements of pyramids constructed from homogeneous dielectrics. Finally, pyramidal absorber will be measured to learn more about the scattering from inhomogeneities. The conclusions of these comparisons shall address the range of applicability of the dielectric corner solution.

1.4 Approach

Chapter two presents the UTD dielectric corner diffraction solution, and discusses the application of the dielectric corner solution to the geometry of a pyramid.

Chapter three focuses on the experimental procedures used to perform this study. The issues involved in the design of the test bodies are discussed. The radar measurement system equipment and configuration are described. The various post-processing techniques used to positively isolate the pyramid tip returns, determine the proper time gate to apply, and compensate for antenna beamwidth are described.

Chapter four presents the experimental results. The techniques for processing and manipulating the experimental and predicted data are presented. The experimental results are compared to predicted values. Findings of the comparisons are discussed.

Chapter five summarizes the findings of this study. Conclusions indicated by the findings are presented. Finally, areas of further study suggested by the findings and conclusions are proposed.

II. Theory

2.1 Introduction

This chapter presents the UTD dielectric corner diffraction solution, discusses the associated geometry, and presents a sample calculation.

2.2 Dielectric Corner Diffraction Solution [2]

The far zone corner diffracted field associated with one edge of a dielectric corner illuminated by a spherical wave is given by [2]

$$\begin{bmatrix} E^c_{\beta_{oc}}(s) \\ E^c_{\phi}(s) \end{bmatrix} \sim \begin{bmatrix} C_a(Q_E) & C_b(Q_E) \\ C_c(Q_E) & C_d(Q_E) \end{bmatrix} \begin{bmatrix} E^i_{\beta_c}(Q_C) \\ E^i_{\phi'}(Q_C) \end{bmatrix} \frac{e^{-j\pi/4}}{\sqrt{2\pi k}} \times \frac{\sqrt{\sin\beta_c \sin\beta_{oc}}}{\cos\beta_{oc} - \cos\beta_c} F[kL_c a(\pi + \beta_{oc} - \beta_c)] \frac{e^{-jks}}{s} \tag{1}$$

where

$$\begin{aligned} C_a(Q_E) = {} & (R_{\parallel}\cos^2\alpha_n - R_{\perp}\sin^2\alpha_n)\, C_n(\phi + \phi') \\ & + (R_{\parallel}\cos^2\alpha_o - R_{\perp}\sin^2\alpha_o)\, C_o(\phi + \phi') \quad , \end{aligned} \tag{2}$$

$$\begin{aligned} C_b(Q_E) = {} & (R_{\parallel} + R_{\perp})\sin\alpha_n\cos\alpha_n\, C_n(\phi + \phi') \\ & + (R_{\parallel} + R_{\perp})\sin\alpha_o\cos\alpha_o\, C_o(\phi + \phi') \quad , \end{aligned} \tag{3}$$

$$\begin{aligned} C_c(Q_E) = {} & -(R_{\parallel} + R_{\perp})\sin\alpha_n\cos\alpha_n\, C_n(\phi + \phi') \\ & - (R_{\parallel} + R_{\perp})\sin\alpha_o\cos\alpha_o\, C_o(\phi + \phi') \quad , \end{aligned} \tag{4}$$

$$\begin{aligned} C_d(Q_E) = {} & (R_{\perp}\cos^2\alpha_n - R_{\parallel}\sin^2\alpha_n)\, C_n(\phi + \phi') \\ & + (R_{\perp}\cos^2\alpha_o - R_{\parallel}\sin^2\alpha_o)\, C_o(\phi + \phi') \quad , \end{aligned} \tag{5}$$

and

$$C_n^o(\beta) = \frac{-\exp(-j\pi/4)}{2n\sqrt{2\pi k}\sin\beta_o} \cot\left[\frac{\pi \mp \beta}{2n}\right] \times$$
$$F[kLa^{\pm}(\beta)]\left|F\left[\frac{La^{\pm}(\beta)/\lambda}{kL_c a(\pi+\beta_{oc}-\beta_c)}\right]\right| . \quad (6)$$

Several of the quantities in the preceding equations are illustrated in Figure 4, which depicts the geometry for the corner diffracted field associated with one edge of the pyramidal tip. The corner diffraction point is labeled Q_C, while the edge diffraction point (that would exist if the edge continued upwards) is labeled Q_E. The incident field E^i is expressed in terms of its $\hat{\beta}_c$ and $\hat{\phi}'$ components, while the corner diffracted field E^c is expressed in terms of its $\hat{\beta}_{oc}$ and $\hat{\phi}$ components; these unit vectors are defined in Figure 4. The angles β_c, β_{oc}, and β_o and the distances s, s', s'', and s_c are shown in Figure 4; the angles ϕ, ϕ' are defined as in three-dimensional edge diffraction [6]. The distance parameters L and L_c are defined in terms of the distances s, s_c, s', and s'' by [2]

$$L = \frac{s's''}{s'+s''}\sin\beta_o \text{ , and} \quad (7)$$

$$L_c = \frac{s_c s}{s_c + s} . \quad (8)$$

The function $F(X)$ is the transition function and is defined by [6]

$$F(X) = 2j\sqrt{X}\exp(jX)\int_{\sqrt{X}}^{\infty}\exp(-j\tau^2)\,d\tau \quad (9)$$

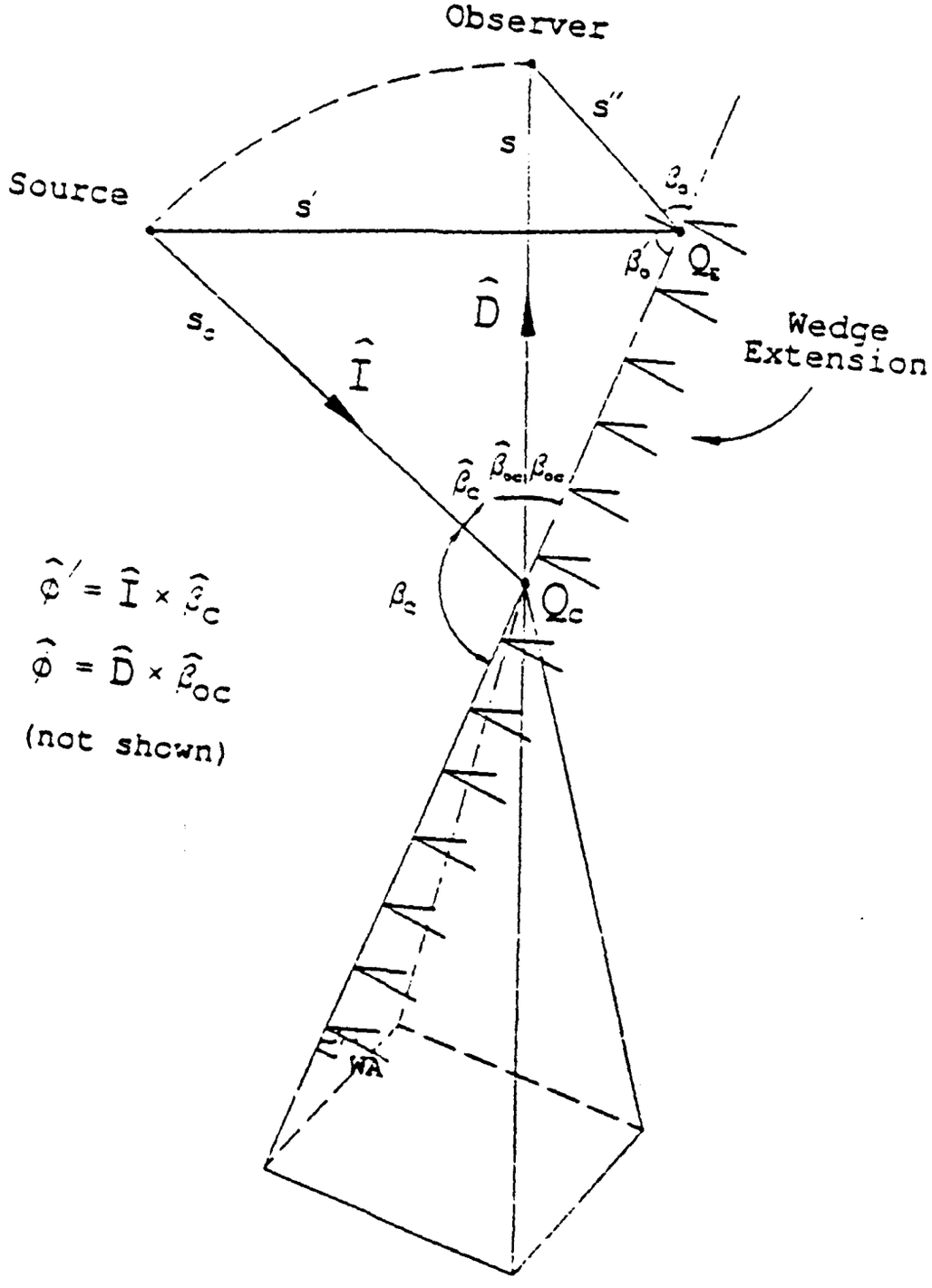

Figure 4. Pyramid Tip Diffraction Geometry [2].

in which one takes the principal (positive) square root. The reflection coefficients are given by [9]

$$R_{\perp} = \frac{\cos\theta_i - \sqrt{(\epsilon_2/\epsilon_1) - \sin^2\theta_i}}{\cos\theta_i + \sqrt{(\epsilon_2/\epsilon_1) - \sin^2\theta_i}} \quad \text{and} \tag{10}$$

$$R_{\parallel} = \frac{(\epsilon_2/\epsilon_1)\cos\theta_i - \sqrt{(\epsilon_2/\epsilon_1) - \sin^2\theta_i}}{(\epsilon_2/\epsilon_1)\cos\theta_i + \sqrt{(\epsilon_2/\epsilon_1) - \sin^2\theta_i}} \tag{11}$$

where θ_i is half the angle between the incident and scatter directions, ϵ_2 is the complex permittivity of the pyramid, and ϵ_1 is the permittivity of the lossless dielectric surrounding the pyramid. Note that, for a conductor, the reflection coefficients are set to ± 1. k is the wavenumber of the medium surrounding the corner. The variable $\alpha_{o,n}$ is the angle between the edge-fixed plane of incidence (defined by the edge and the ray from the source to Q_E) and the ray-fixed plane of incidence (defined by the normal to the o-face or n-face and the ray from the source to Q_E). The o and n subscripts to α indicate whether the ray-fixed plane of incidence is based on the o-face or n-face normal.

WA is the wedge angle. The wedge angle is used to define n as

$$n = 2 - WA/\pi \ . \tag{12}$$

The function $a^{\pm}$ is defined by [6]

$$a^{\pm}(\beta) = 2\cos^2\left(\frac{2n\pi N^{\pm}-\beta}{2}\right) \qquad (13)$$

in which $N^{\pm}$ are the integers which most nearly satisfy the equations

$$2\pi nN^{\pm}-\beta=\pm\pi . \qquad (14)$$

$a(\beta)$ is defined by [6]

$$a(\phi\pm\phi') = 2\cos^2\left(\frac{\phi'\pm\phi'}{2}\right) . \qquad (15)$$

Since more than one edge comprise a corner, it is necessary to apply the edge diffraction solution to each edge of the corner. In the case of the pyramids used in this study, this meant applying the edge diffraction solution 4 times to obtain the tip diffracted field from a single pyramid. The field contributions from each edge are summed to obtain the total scattered field. The co-polarized backscatter is obtained from

$$\vec{E}_{s_{CP}} = \left(\frac{\vec{E}_{s_{TOT}}\cdot\vec{E}_i}{|\vec{E}_i|^2}\right)\vec{E}_i . \qquad (16)$$

2.3 Sample Calculations

The calculations presented in the preceding section were implemented into an "Absorber code." Sample calculations are presented in Figure 4. This figure shows the predicted co-polarized backscatter for three pyramid

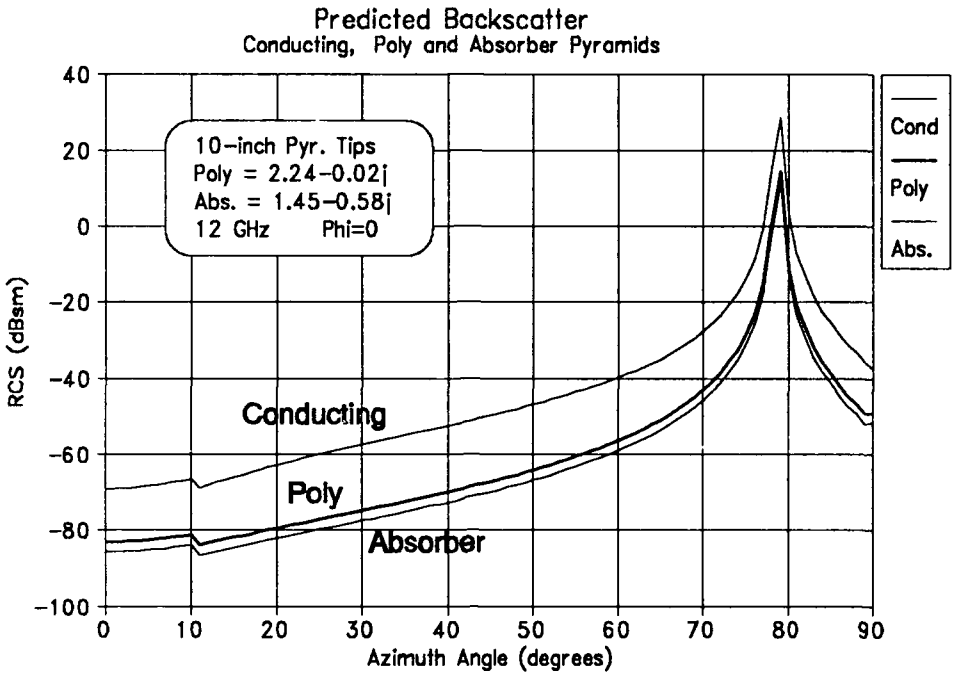

Figure 5. Predicted Backscatter from 10-inch Conducting, Polyethylene, and Absorber Pyramid Tips as Azimuth Varies (HH Pol.).

tips of same size but differing materials: conducting, lossless dielectric (polyethylene), and lossy dielectric (absorber). The predictions are made for 12 GHz as the tips are rotated in azimuth. The conducting pyramid tip (top trace) shows a discontinuity at θ=11 degrees as the rear pyramid face is shadowed. False shadow boundaries exist for the associated edges of this face. At θ=79 degrees, the pyramid face is broadside to the source/observer and a singularity occurs. This singularity is due to the far-zone approximations used to implement the computer code.

The middle trace is the lossless dielectric pyramid tip prediction. The relative permittivity used was 2.24-0.02j, the measured dielectric constant for polyethylene. The discontinuity and singularity seen in the conducting tip predictions are again evident; since these are geometrically related phenomena, they are expected to repeat at the same angles. The backscatter level of the lossless dielectric tip is consistently lower than that of the conducting tip. This is also expected since the reflection from a dielectric is less than that of a perfect conductor.

The bottom trace is the predicted backscatter from a lossy dielectric (absorber) pyramid tip. The relative permittivity used was 1.45-0.58j, a typical figure for medium loaded absorber [1]. Again the geometric aspects are predicted. The predicted scattering is less than that of both the conducting and lossless dielectric pyramid tips.

The prediction code is discussed further in the next section and is then compared in Chapter IV to measured backscatter.

III. Procedure

3.1 Introduction

One goal of this thesis is to validate the approximate UTD solution for diffraction by a lossy dielectric corner which was developed in [2]. Towards this goal, scattering predictions for various pyramid tips were made and experimental results were obtained. This chapter details the experiments performed and the operation of the tip scattering prediction program. The design considerations of the test bodies are discussed. The method of isolating and calculating the pyramid tip return is presented. Finally, the operation and modifications to the tip scattering prediction program are detailed.

3.2 Test Body Design Considerations

Three different types of materials were measured: conductors, lossless dielectrics, and lossy dielectrics. Each material possesses particular properties which must be considered in the design of the test body.

3.2.1 Conducting Test Bodies. Two test bodies were used for the measurement of the conducting pyramid tips. Each conducting test body was 40 inches long. Each test body was formed by two pyramids connected at their bases to a common shaft of square cross section. The pyramid bases and the shaft sides were each 4 inches from edge to edge. Figure 6 shows the side and end views of the conducting test

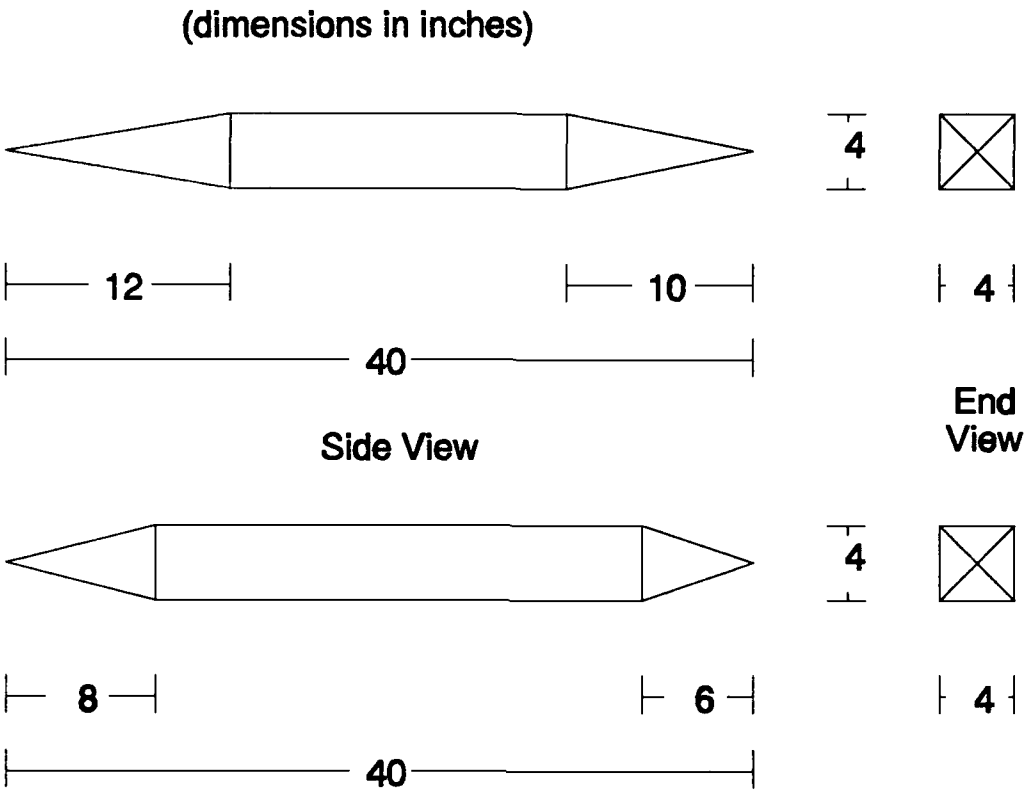

Figure 6. Side and End Views of the *Conducting Pyramid Tip* Test Bodies

bodies. As the figure shows, 4 different pyramids were built; these pyramids were 12, 10, 8 and 6 inches tall from tip to base. To reduce weight and facilitate fabrication, the conducting test bodies were of a hollow plywood construction and painted with an electrically conducting paint.

The design of the test bodies should physically isolate the scatterer of interest from other scattering sources. In the case of the conducting test bodies there are two primary scattering sources which must be physically isolated. These scatterers are other features of the test body itself and

the target support pedestal upon which the test body rests during measurement. Physical isolation of scatterers is measured by the elapsed time between the returned signals of those scatterers. A threshold is set based upon the measurement system resolution. For the purposes of the initial test body design, the threshold was set at 0.25 nanoseconds. This translates to 1.5 inches downrange distance. Given this threshold, the design of the test body, and the location of the other scatterers, a domain of measurement may be determined.

The geometry of the test body relative to the target support pedestal is shown in Figure 7. There is some range of θ_{uTS} for which the tip return is expected to be unambiguously identifiable *from* the target support. This range of θ_{uTS} is given by

$$\begin{aligned} 20\cos\theta_{uTS} &\geq 12+1.5 \text{ , or} \\ |\theta_{uTS}| &\leq 47.5^\circ \text{ .} \end{aligned} \tag{17}$$

Thus, for all test body aspect angles from 0 degrees (nose-on) incidence to 47.5 degrees incidence, the pyramid tip return should be clearly distinguishable from the scattering by the target support. In addition, the target support pedestal scattering is reduced through background subtraction. While measurements may be made for angles greater than 47.5 degrees incidence, the accuracy will depend on how well the subtraction procedure eliminates the scattering of the target support.

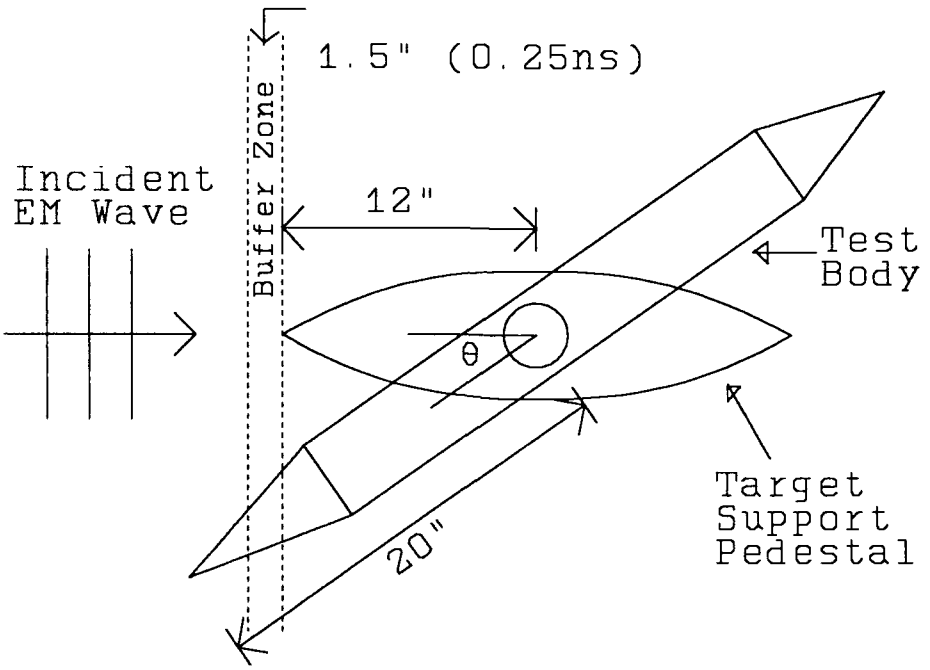

Figure 7. Relative Geometry of the Test Body and the Target Support Pedestal.

The other scatterer to be isolated is on the test body itself. Simple analysis of the test body shows the nearest scattering center is the base of the pyramid. The relative geometry of the pyramid tip and base is shown in Figure 8. There exists some domain of angles θ_{uPB} where the tip scattered return occurs more than the threshold ahead of the base scattered return. This range of θ_{uPB} is given by

$$20\cos\theta_{uPB} \geq (20-h)\cos\theta_{uPB} + 2\sin\theta_{uPB} + 1.5 \ . \qquad (18)$$

Solving for θ_{uPB} for the pyramids used, the domains of θ_{uPB} are given in Table 1. Unlike the target pedestal scattering, the test body scattering cannot be subtracted

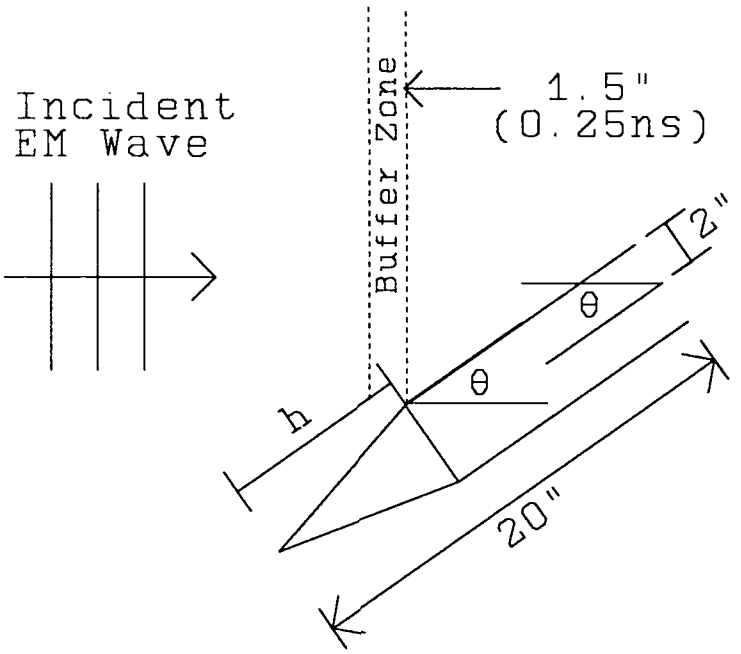

Figure 8. Relative Geometry for the Calculation of Pyramid Tip Isolation From Base Scattering.

out. The values in Table 1 therefore may be considered absolute limits to the domain of measurable angles.

3.2.2 Lossless Dielectric Test Bodies. Two test bodies were used for the measurement of lossless dielectric pyramid tips. Each of the test bodies were similar in shape to those used for the conducting pyramid tip measurements. For the case of a lossless dielectric test body, two additional measurement considerations apply. These are scattering from material inconsistencies and scattering from material interfaces.

Table 1. Maximum Azimuth Angle for 0.25ns Separation Between Pyramid Tip and Base Scattering.

Pyramid Height (inches)	Maximum θ_{uPB} (degrees)
12	73.5
10	70.2
8	65.5
6	57.8

Material inconsistencies (inhomogeneities) are dependent on the actual choice of material used. Inhomogeneities may be determined by making a time domain analysis of a sample of the material under consideration. Figure 9 shows a time domain analysis of a sample of polyethylene type "A" (Poly). This analysis shows no identifiable inhomogeneities. The two peaks are the expected returns from the front and back faces of the sample.

Material interfaces result from the physical construction of the target. These interfaces could be either Poly-Poly or Poly-air. Poly-Poly interfaces typically occur at glued junctions. Poly-air interfaces would occur if the target were of a hollow construction. These interfaces can be eliminated by fabricating each test body from a single bulk piece of dielectric.

The other concerns which factored into the choice of lossless dielectric were cost, availability, weight,

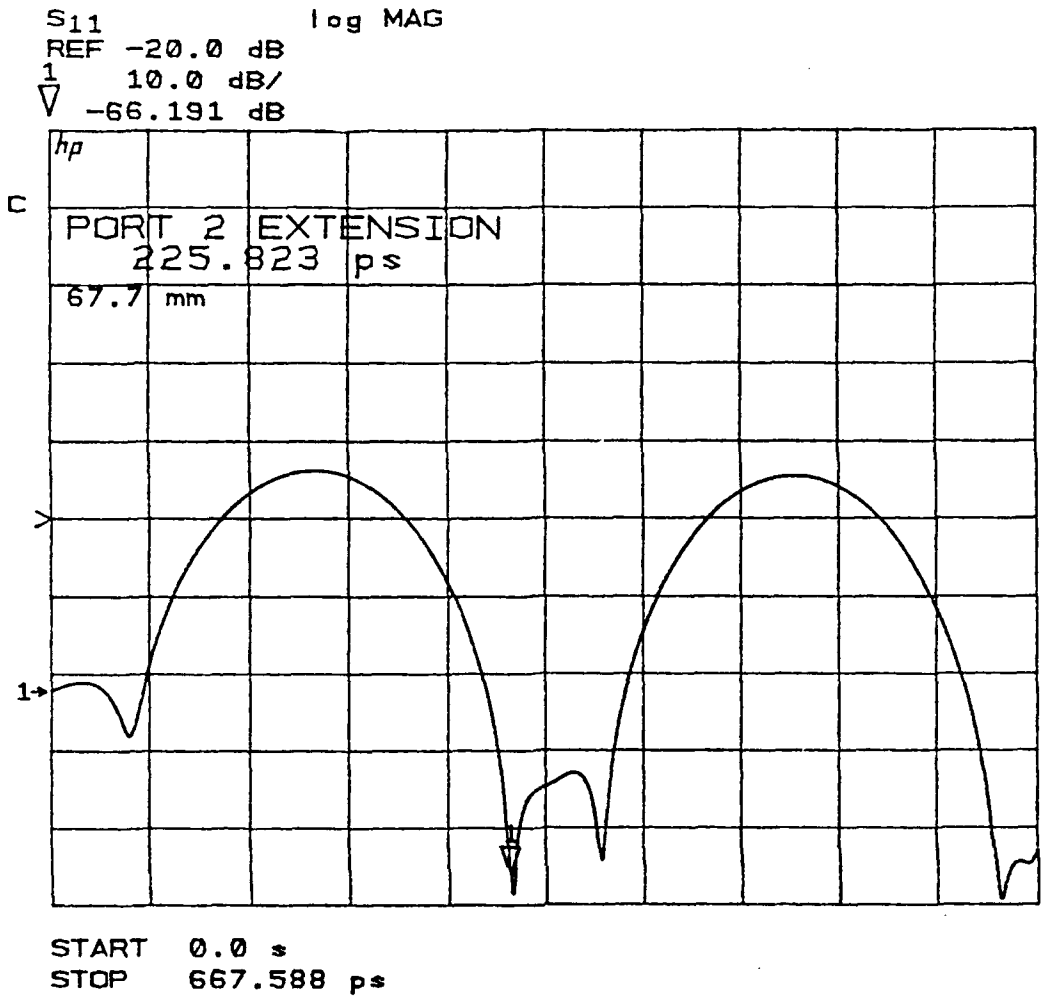

Figure 9. Time Domain Analysis of a Sample of Polyethylene Type "A".

machinability, and relative permittivity. The first four concerns are obvious; the relatively high dielectric constant is desired, since this will increase the level of the scattered return. The material chosen was polyethylene type "A" (which is referred to in this report as *Poly*). Poly has a measured relative permittivity of 2.28 at 12 Ghz, with no appreciable loss. Due to material constraints (discussed later), the total length of each of the test

bodies was just less than 40 inches; however, by offsetting the test body during measurements, the 20 inch radius arc of the conducting pyramid tips was maintained. Thus, the calculations for the domain of unambiguous measurements still apply.

3.2.3 Lossy Dielectric Test Bodies. The scattered signal level from the lossless dielectric pyramids was extremely small, and the scattered signal from the lossy (absorber) dielectric pyramids was expected to be smaller still. In an attempt to raise the backscattered signal of the lossy dielectric pyramid above the noise floor of the measurement system used, the absorber tips to be measured are mounted in a 2×2 pattern with the tips co-planar with the incident wave front. With perfect alignment each tip scatters in-phase, resulting in a 12 decibel increase in the scattered return. Any alignment error will detract from this 12 decibel gain. Besides raising the scattering level, the co-planar tips allow the tip return to be time gated. This test body can only be used for measurements at fixed angles ($\theta=0^\circ$, $\theta=40^\circ$); any rotation of the test body would move the plane of the pyramid tips relative to the plane of the incident wavefront, preventing accurate time gating and in-phase addition.

The test body for the lossy dielectric pyramid tips is shown in Figure 10. The pyramids are 18 inches tall on 6 inch square bases. The pyramids have been mounted onto a

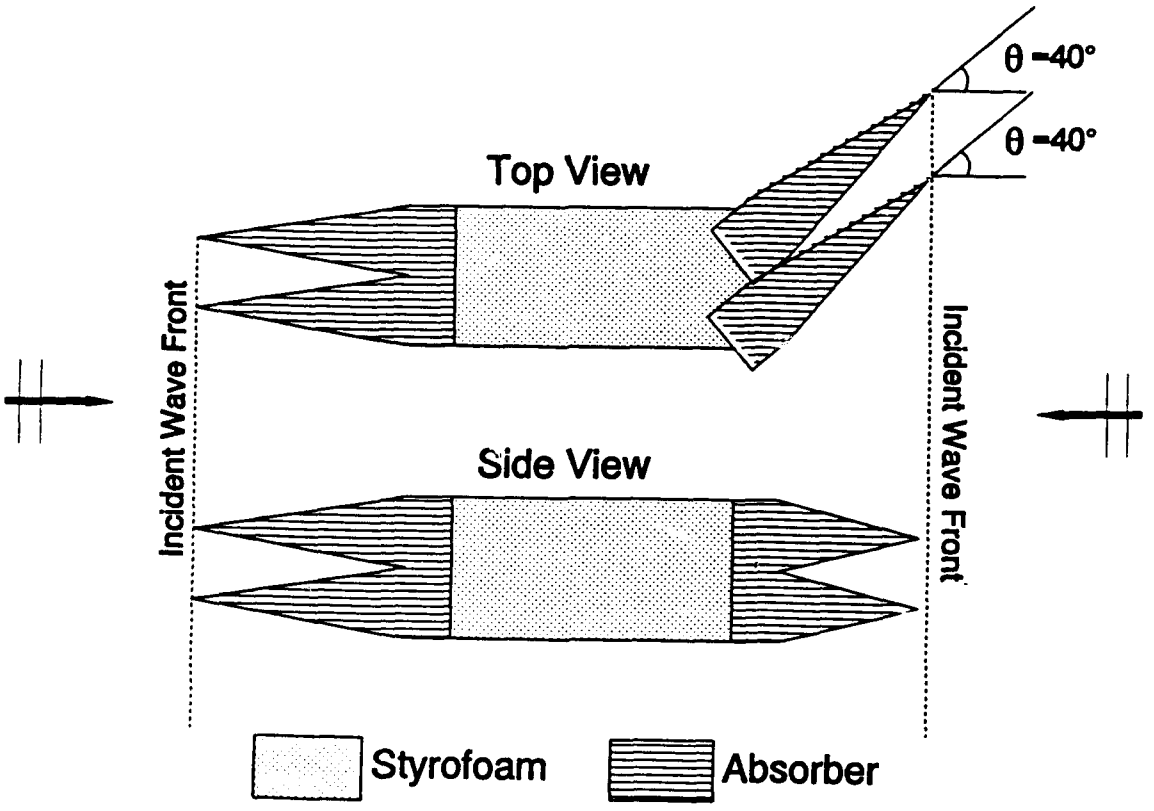

Figure 10. Test Body for Measurement of Lossy Dielectric Pyramid Tip Scattering.

1×1×2 foot block of styrofoam. The unmodified pyramids at one end are seen at nose-on (θ=0°) incidence. The angled pyramid tips are co-planar at an angle of 40 degrees. This is well within the domain of unambiguous measurement for all scattering mechanisms, except possibly for the scattering from inhomogeneities.

3.3 Measurement and Post-Processing

This section discusses the measurement facility which was used to perform the experimental portion of this research, and the post-processing which was performed on the measured data to obtain useful results.

3.3.1 Radar Cross Section (RCS) Measurement System. A block diagram of the system used for the measurement of the pyramid tip scattering is shown in Figure 11. Measurements are controlled by a PC/AT (80286 based) computer. This computer controls the actions of the network analyzer, directs the movement of the target azimuth positioner, and records and tags the measured data. The network analyzer, in turn, controls the signal generation and measurement equipment. The RCS measurement system is capable of frequency generation and measurement from 6 Ghz to 18 Ghz. The radar signals are transmitted and received through two co-polarized, narrow-beam diagonal horn antennas. The signal polarization (horizontal or vertical) is controlled by a positioner physically rotating both antennas. Measured data is transferred to the PC/AT computer which temporarily saves the data along with administrative tag information such as target identification, azimuth angle, and polarization. The measurements and data tags are then transferred to a DEC Mini-VAX for post-processing and printing. The Mini-VAX was used for all of the measurement post-processing, but not manipulation. The capabilities of this system permit the swift isolation and measurement of the pyramid tip returns.

3.3.2 Isolation of the Pyramid Tip Frequency Response. The first step in post-processing the raw measured data is calibration. The standard calibration equation used is

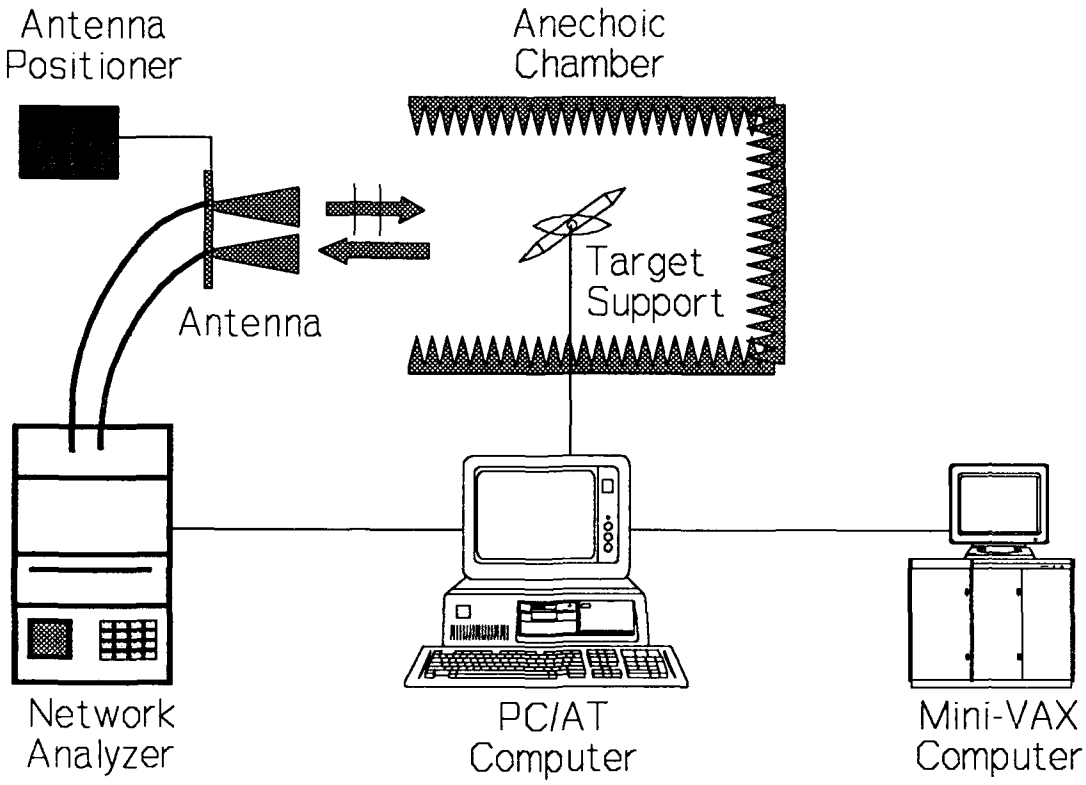

Figure 11. Radar Cross Section Measurement System Block Diagram.

$$T_c(f) = E(f)\frac{T(f) - B_t(f)}{S(f) - B_s(f)} \qquad (19)$$

where: T_c is the calibrated target RCS and phase; T is the complex return signal measured from the target; S is the calibration sphere measurement; B_t is the target background measurement; B_s is the sphere background measurement; and E is the calculated RCS and phase of a sphere. The variable f indicates that the calibration is done on a point-by-point basis for each frequency measured. All measurements were made from 6 Ghz to 18 Ghz at 0.01 Ghz intervals.

Since the calibrated data has both amplitude and phase information, it may be used to find the time domain response of the target. The time domain response of the test body is found by performing an inverse fast Fourier transform on the calibrated data. Figure 12 shows the time domain response (top) and frequency domain response (bottom) of a test body. The time domain response is useful for identifying specific scattering mechanisms. In Figure 12, the following scattering can be identified: scattering from the 6-inch pyramid tip occurs at -3.4 nanoseconds; scattering from the 6-inch pyramid base occurs at -2.4 nanoseconds; pyramid base-to-base double diffractions occur at approximately -2.1 nanoseconds; scattering from the base of the 8-inch pyramid (at the rear end of the test body) occurs from +0.7 to +1.0 nanoseconds and include single and double diffractions; and the 8 inch pyramid tip diffraction is seen as a small spike at +2.4 nanoseconds. The scattering between -2.0 and +0.5 nanoseconds is attributed to interactions between the target and the support pedestal, or higher order mechanisms. The scattering after +2.7 nanoseconds is attributed to higher order mechanisms, including multiple internal reflections of the test body.

Having identified the pyramid tip return, the next step is to apply a *time gate*. The time gate eliminates (ignores) any time domain response data which does not occur within the specified time. Figure 13 shows the time domain

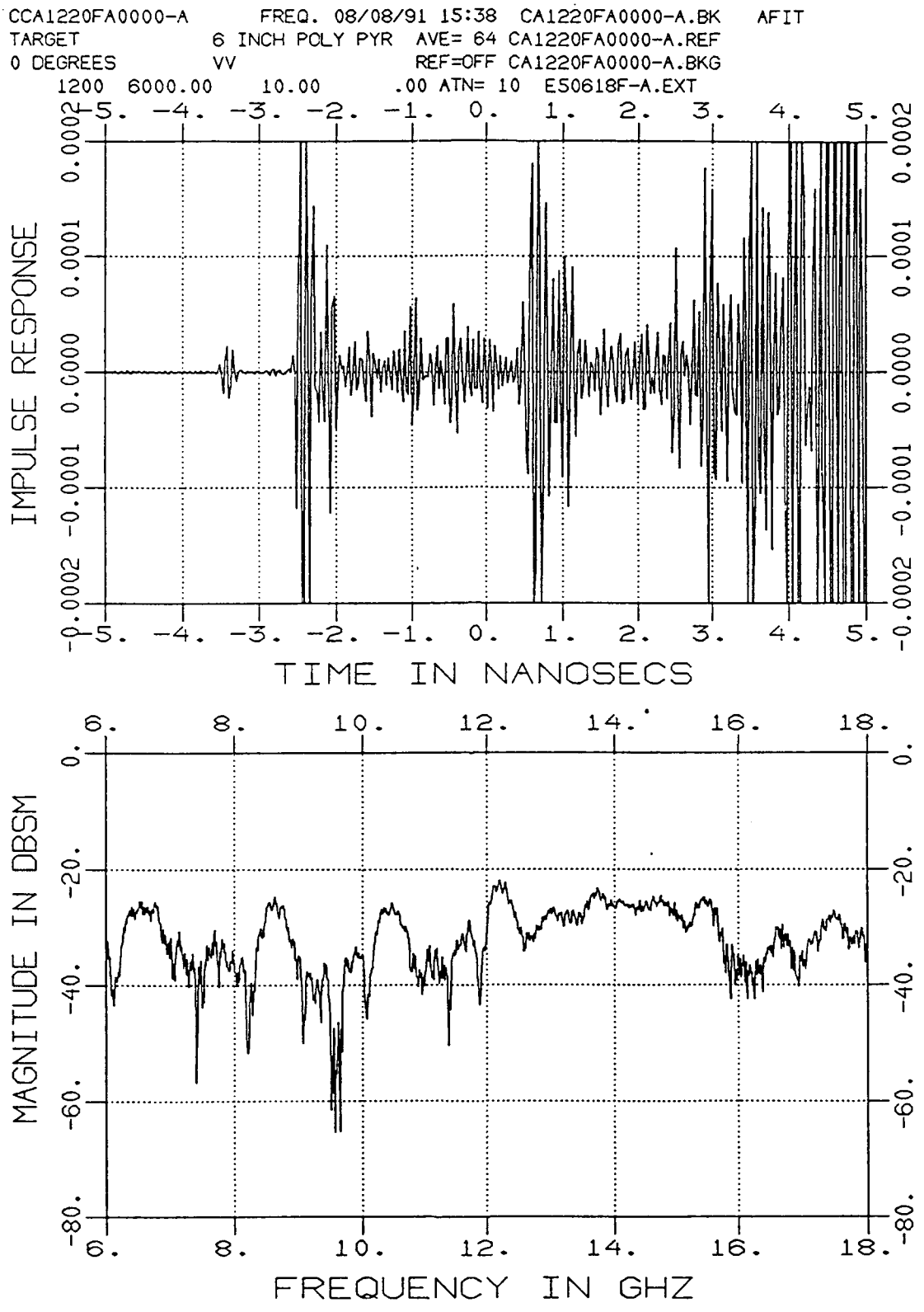

Figure 12. Time and Frequency Domain Response of the 6-inch Poly Test Body at Nose-On (θ=0°) Incidence.

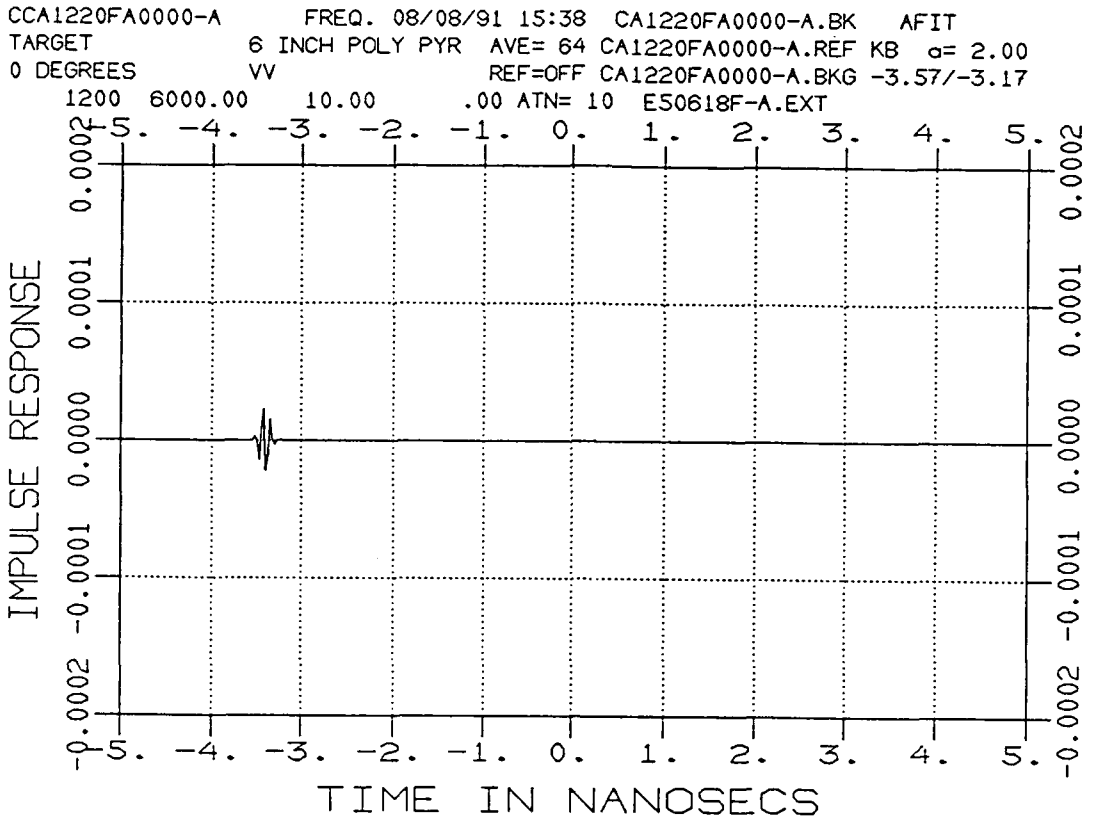

Figure 13. Time Domain Response of 6-Inch Poly Test Body at Nose-on Incidence with Time Gate Applied.

response of the test body shown in Figure 12 with a time gate applied from -3.57 to -3.17 nanoseconds. A comparison of the two figures shows that this time gate captured the entire pyramid tip return without including any other scattering mechanisms.

A Kaiser-Bessel weighting function (time gate) is applied, then a fast Fourier transform is performed to obtain the frequency response of the pyramid tip. The frequency response of the pyramid tip is shown in Figure 14.

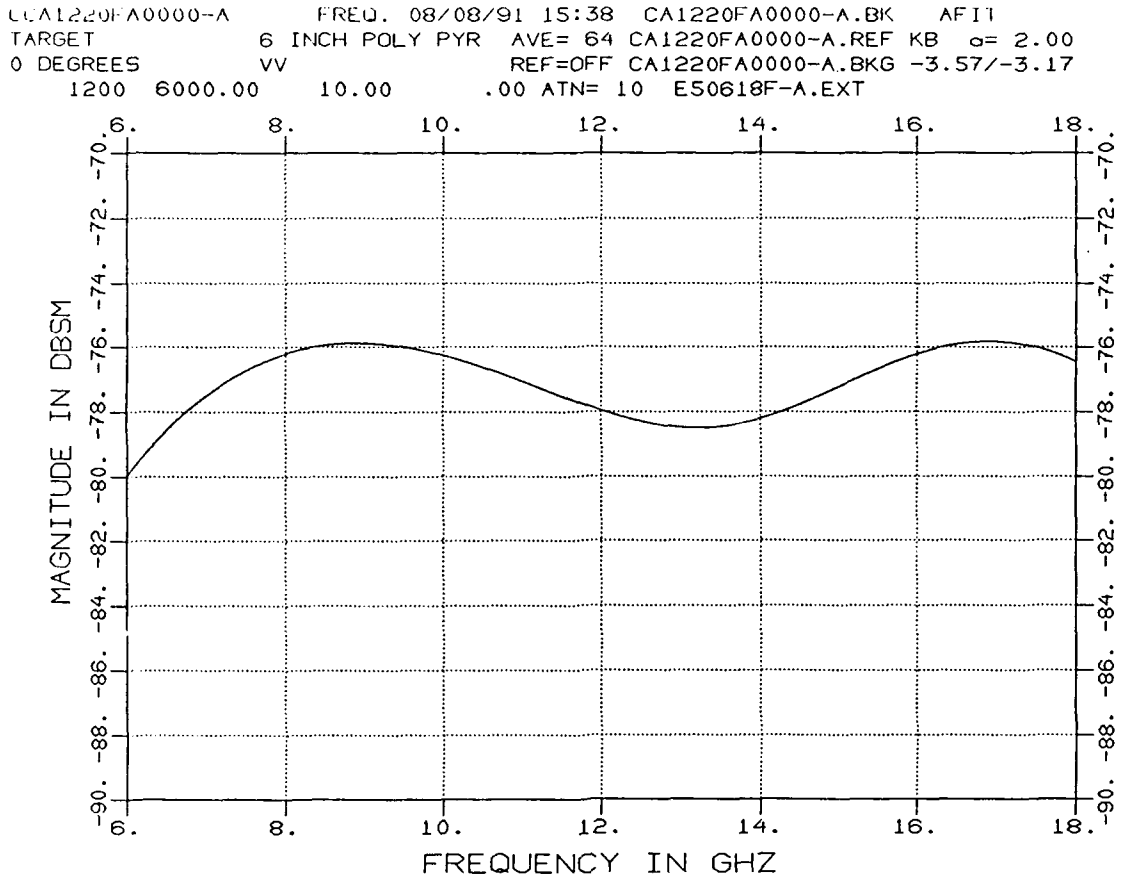

Figure 14. Frequency Response of the 6-Inch Poly Pyramid Tip after Time Gating.

This procedure for obtaining the tip response was used for both the conducting and dielectric test bodies. However, the time gate to apply was determined differently.

3.3.3 Determination of the Time Gate. Proper determination of the time gate to apply is essential for accurate measurements of the pyramid tip scattering. For the case of conducting test bodies, the level (amplitude) of the returns and the distinct scattering observed allowed the time gate to be visually determined. However, the levels of

the tip returns of the dielectric test bodies often were less than one-fifth of the corresponding conducting test body. The level of the interactions between the dielectric test body and the target support pedestal were much greater relative to the level of the tip scattering. The dielectric scattering mechanisms were less distinct when compared to the conducting scattering bodies. First attempts to time gate the dielectric pyramid tips clearly showed that "eyeballing" would not produce satisfactorily accurate or repeatable results. A more systematic approach was found.

3.3.3.1 Determination of Time Gate Width. The accuracy of the frequency response is a function of the width (duration) of the time gate used. The goal is to find a time gate width which is wide enough to provide accurate frequency response data, yet not so wide as to include other scattering mechanisms. In order to find this optimal time gate width, the tip return of a 6-inch Poly pyramid was post-processed using various time gates. The time gates were centered about the tip return midpoint (-3.38 nanoseconds), and gate widths from 0.04 to 0.80 nanoseconds were applied. The gated time domain data was transformed back to the frequency domain, and the RCS value at 12 Ghz was noted. Figure 15 shows these values as a function of the time gate width applied. This plot shows that at a gate width of 0.40 nanoseconds the scattered signal magnitude levels off. Gate widths greater than 0.40 nanoseconds

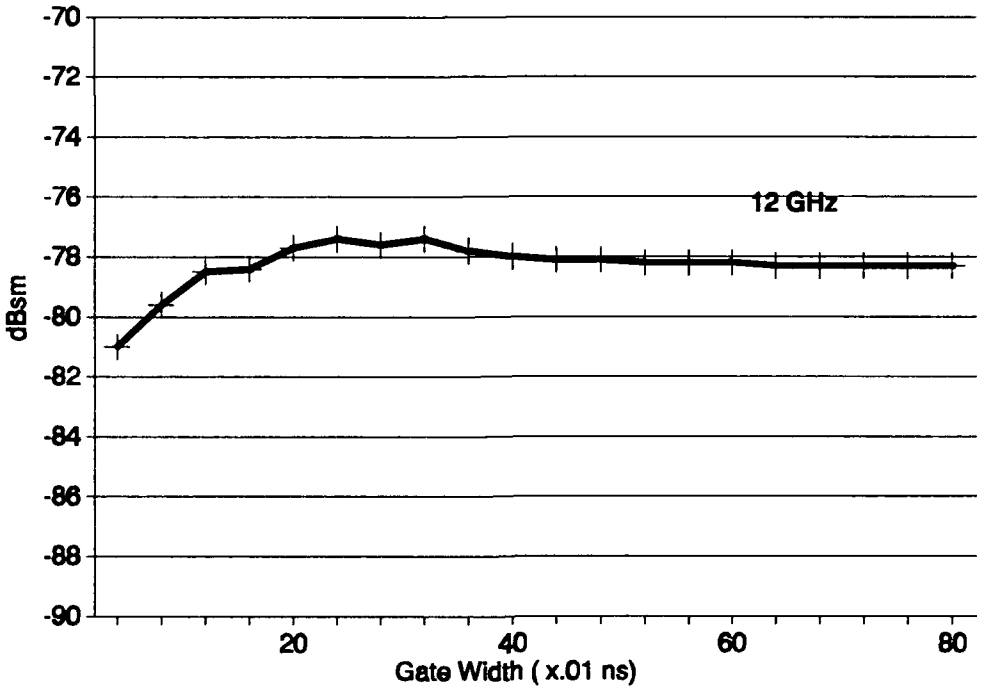

Figure 15. Time Gate Width Variation Effects on 6-Inch Poly Pyramid Tip Scattering Level at 12 GHz.

produce no appreciable increase in accuracy. Gate widths less than 0.20 nanoseconds were completely inaccurate. Gate widths between 0.20 and 0.40 nanoseconds were within 0.5 dBsm of the final value. Similar plots at 10 Ghz and 14 Ghz confirm the stability of the magnitude for gate widths of 0.40 nanoseconds and more. Thus, the gate width was established.

3.3.3.2 Determination of Time Gate Center. Having determined the width to use for the time gate, the next step was to determine the time gate center.

Geometrical approximation had been used for the conducting pyramids using

$$t_c = -3.39\cos\theta \text{ (ns)}. \qquad (20)$$

3.39 nanoseconds corresponds to 20 inches downrange which is the distance of the pyramid tip from the chamber reference point (pedestal axis). One option would be to use the same gate centers as were used for the conducting test bodies. Since differences as small as 1.5 mm would change the gate center, this method was not pursued.

Instead, the 6-inch Poly pyramid tip was post-processed using the 0.40 nanosecond gate width with different gate centers. The pyramid tip backscatter was recorded for gate centers varying from -3.49 to -3.29 nanoseconds. This data was plotted for the center frequency (12 Ghz) and for 10 Ghz and 14 Ghz. This plot is shown in Figure 16. It was found by moving the time gate forward and backward, the center frequency (12 Ghz) response was characterized by a peak (or plateau) approximately 0.03 nanoseconds wide which dropped off quickly and distinctly on either side. The center of this plateau was determined as the time gate center. In practice, the time gate center was found by first using the geometrical approximation to get near the gate center. The time gate was then moved forward and backward to locate the points there the center frequency response of the pyramid tip dropped off. The midpoint was then chosen as the gate center.

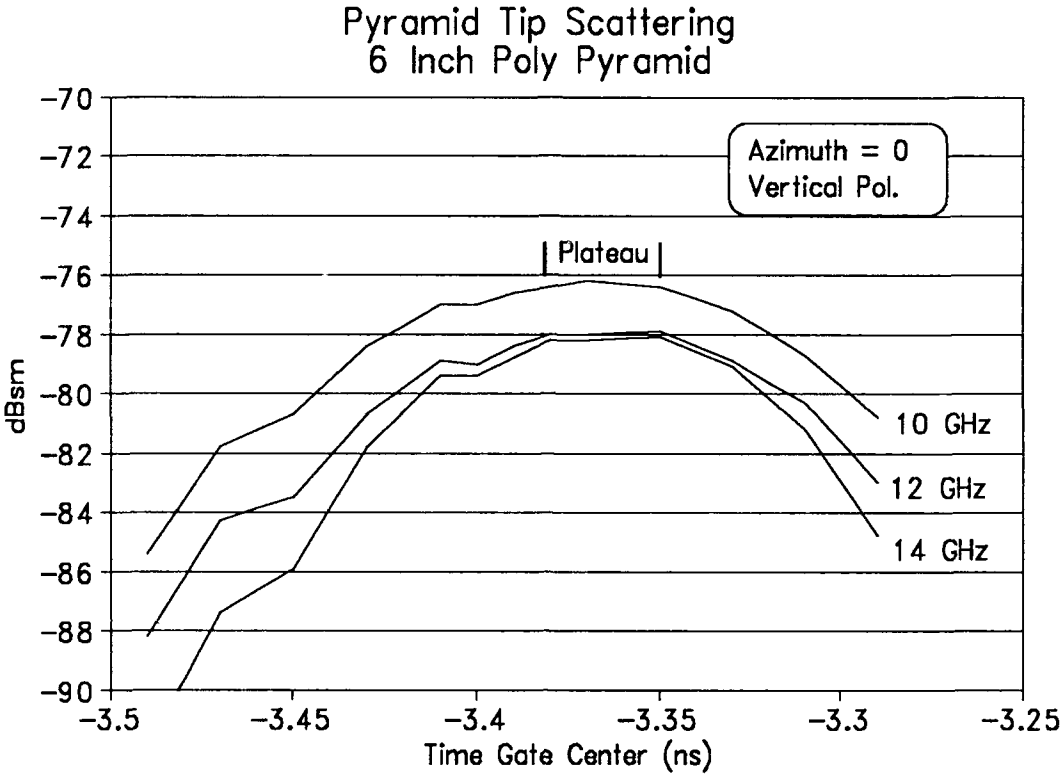

Figure 16. Time Gate Center Variation Effects on 6-Inch Poly Pyramid Tip Scattering Level.

3.3.4 Calibration for Antenna Beamwidth. The antennas in the RCS measurement chamber are characterized by very narrow beamwidths. To calibrate for the signal decline as the pyramid tips move out of the main beam, calibration curves were made for each polarization. These calibration curves were made by measuring the scattering from a small (2-inch diameter) conducting sphere. This sphere was placed on a mount which placed the sphere center at the same height and radial distance (20 inches) as the pyramid tips. Frequency scans were made from 0 degrees azimuth to 90 degrees at 5 degree intervals.

The sphere measurement at some angle θ, S_θ, and the sphere measurement at $\theta=0^\circ$, S_0, are used to generate a calibration factor C_θ, which is defined by

$$C_\theta(dB) = S_0(dBsm) - S_\theta(dBsm) \tag{21}$$

The calibrated tip scattering is then given by

$$T_{c,\theta}(dBsm) = T_{m,\theta}(dBsm) + C_\theta(dB) \tag{22}$$

where $T_{m,\theta}$ is the measured value of tip scattering at some angle θ along the 20 inch radius arc. The calibration curves for three frequencies are shown in Figure 17. The upper plot is for vertical polarization, while the lower plot is for horizontal polarization.

These calibration curves apply directly to a single pyramid tip moving along a 20 inch radius arc, which was the case for the conducting and lossless dielectric pyramids. The remainder of this section is devoted to the application of these calibration curves to the absorber pyramids of Figure 10.

A single measurement of the absorber pyramid test body gives a combined scattering value for four pyramid tips. Two complications arise when using the calibration curves of Figure 17 to calibrate this measurement. The first complication is that the four tips do not lie on the 20 inch radius arc which the calibration sphere traveled. The second complication is that the four tips are in different physical locations, so that, in general, different

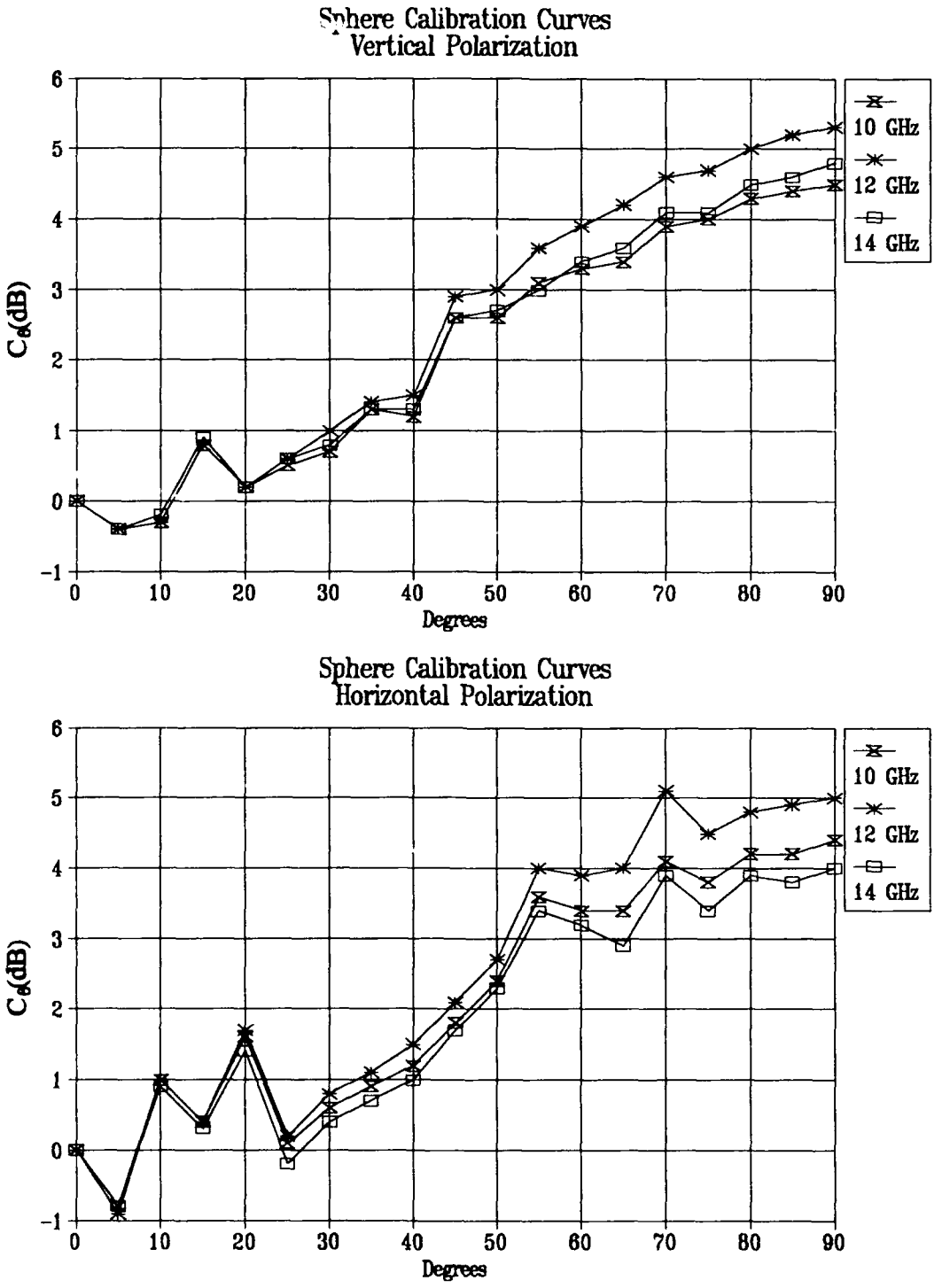

Figure 17. Calibration Curves for 10, 12 and 14 Ghz for Vertical and Horizontal Polarization for a Target at 20-Inch Radial Distance.

calibration factors apply. Obviously these different calibration factors cannot simply be applied to the individual measured returns, since the receiver senses the total return.

The first complication is dealt with fairly easily. The calibration factor C_θ accounts for two effects: the radial distance (r) from the antenna to the target, and the angular location (ϕ) of the target in the antenna radiation pattern as shown in Figure 18. Since the antenna is known to have a narrow beamwidth, the effect of the angular location is assumed to be the dominant effect. By this assumption, the calibration factor C_θ to be applied to a particular tip is that which corresponds to the same angular location ϕ of the antenna's radiation pattern. Since the positions of the absorber tips are known, the calibration term C_θ is approximated by projecting those points back onto the calibration arc as shown in Figure 18.

The second complication can be dealt with now that the value for C_θ for each tip is determined. One side of the absorber target body presents four pyramids at nose-on incidence to the radar. Since all four tips are symmetrically placed about the antenna centerline, it can be shown that the calibrated (single) tip scattering is given by

$$T_c(dBsm) = T_m^{TOT}(dBsm) + C_\theta(dB) - 12dB \qquad (23)$$

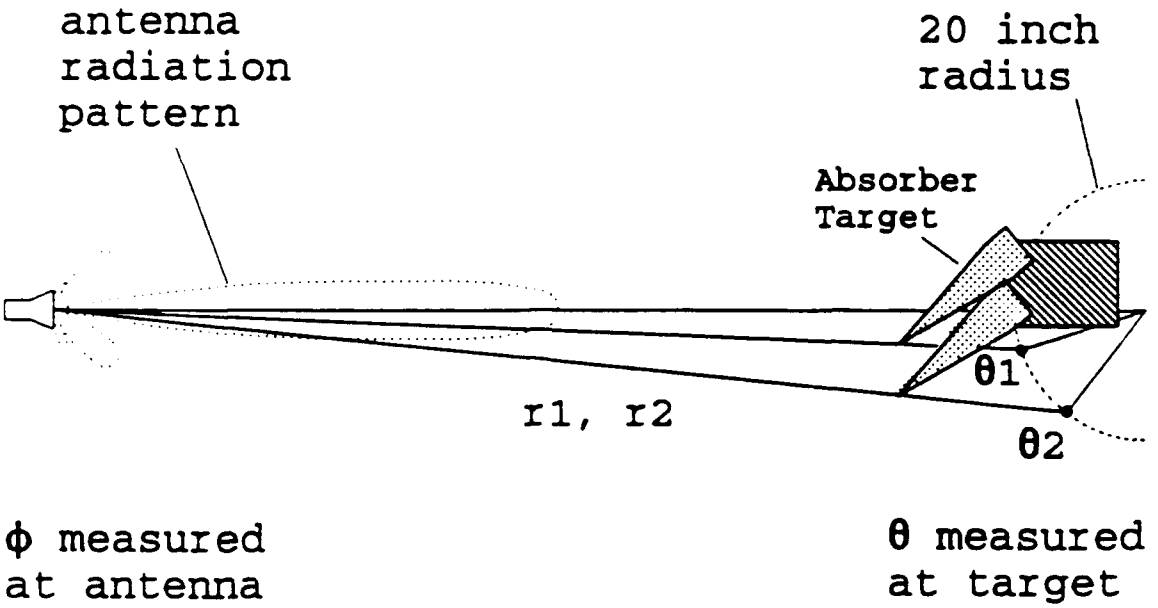

Figure 18. The Calibration Term C_θ Accounts for Radial Distance and Angular Location of the Target

where T_m^{TOT} is the measured return from the absorber tips at nose-on incidence, C_θ is the appropriate calibration factor for the pyramid tips, and the 12 decibel term accounts for the fact that four tips added (approximately) in phase.

The other side of the absorber target presents four pyramids each oriented 40 degrees from nose-on incidence. One calibration value applies to two tips, while a second value applies to the remaining two tips. It can be shown that the single calibrated tip scattering is given by

$$T_c(dBsm) = T_m^{TOT}(dBsm) + 10\log\left\{\frac{4C_{\theta 1}C_{\theta 2}}{C_{\theta 1}+2\sqrt{C_{\theta 1}C_{\theta 2}}+C_{\theta 2}}\right\} - 12\,dB \qquad (24)$$

where T_m^{TOT} is the measured return from the absorber target, and $C_{\theta 1}$ and $C_{\theta 2}$ are the appropriate calibration factors for each of the two pairs of pyramids. Note that in equation (24) $C_{\theta 1}$ and $C_{\theta 2}$ are multiplicative factors and not decibels.

3.3.5 Manipulation of Pyramid Tip Response Data. The frequency responses of the conducting and lossless dielectric pyramids are measured at various azimuth angles. After appropriate time gating, the measured data is transformed back to the frequency response format. The frequency response (after time gating) was also obtained for both sides of the absorber (lossy dielectric) target, and for the 2-inch calibration sphere (at a 20-inch arc radius) at various azimuth angles. All of the frequency response graphs were manually digitized at 2 Ghz frequency intervals, and entered into a spreadsheet. Through proper combination of the various spreadsheets on a cell-by-cell basis, virtually any response of the calibrated pyramid tip data can be presented.

3.4 Prediction of Tip Scattering

An interactive FORTRAN code, based on the equations and geometry developed in Chapter II, was used for predictions on lossless and lossy dielectric pyramids. This program allowed bistatic prediction for any size pyramid at a given frequency or frequencies. The predictions for conducting pyramid tips were made through a modification to the

dielectric pyramid code, where the reflection coefficients were set to ±1, depending on polarization.

After predicting the pyramid tip backscatter levels, conversion into spreadsheet format is a simple matter. The same manipulations of measured data may then be performed on the predicted data. Having established procedures for the measurement and prediction of the tip scattering by pyramid tips, comparisons may be made. This is the subject of the next chapter.

IV. Data and Conclusions

4.1 Introduction

The purpose of this study is to validate a dielectric corner diffraction solution, and to investigate the scattering nature of absorber pyramids. It was decided to do the validation using the corner defined by the tip of a pyramid. Measurements were made using conducting, lossless dielectric and lossy dielectric pyramids, as described in the previous chapter. Although the measurements were made via frequency sweeps at various azimuth angles, the results are presented here as RCS versus azimuth angle. Measured data is compared to computer predictions based on the corner diffraction solution of [2].

4.2 Conducting Pyramid

Recall that the dielectric corner diffraction solution makes two major assumptions: the portion of the diffracted field associated with the ISB is negligible; and the total reflection from an exposed face may be approximated by the initial external Fresnel reflection coefficient. In applying this solution to a conductor, the second assumption (reflection coefficient) certainly holds. The first assumption (negligible ISB term) was based on the observation that the dielectric material and vanishing thickness of the corner would result in no discontinuity at

the ISB. This is not the case for a conducting corner: the conductor should give rise to a significant discontinuity at the ISB. However, the measurements which were made in this study are all backscatter measurements, and the observer is always a large angular distance from the ISB. Thus, *for the purposes of this study*, the assumption of a negligible diffraction contribution from the ISB discontinuity is also valid.

4.2.1 Solution Accuracy as Aspect Angle Varies. This section is concerned with the agreement between prediction and measurement for a fixed size conducting pyramid at a fixed frequency as the azimuth angle is varied.

Figure 19 shows the predicted and measured backscatter for a 6-inch conducting pyramid at 12 Ghz with the incident field horizontally polarized. This response is typical of different size pyramids under horizontal polarization as azimuth varies. This particular figure shows that the agreement with prediction overall is very close. The agreement is less close at and near nose-on incidence (θ=0) than at moderate angles. Overall agreement between measured and predicted values is within 2 decibels. The average difference is less than 1 decibel if the azimuth range is restricted to between 20 and 50 degrees. For this size pyramid, the base scattering begins to affect the response at angles greater than 50 degrees.

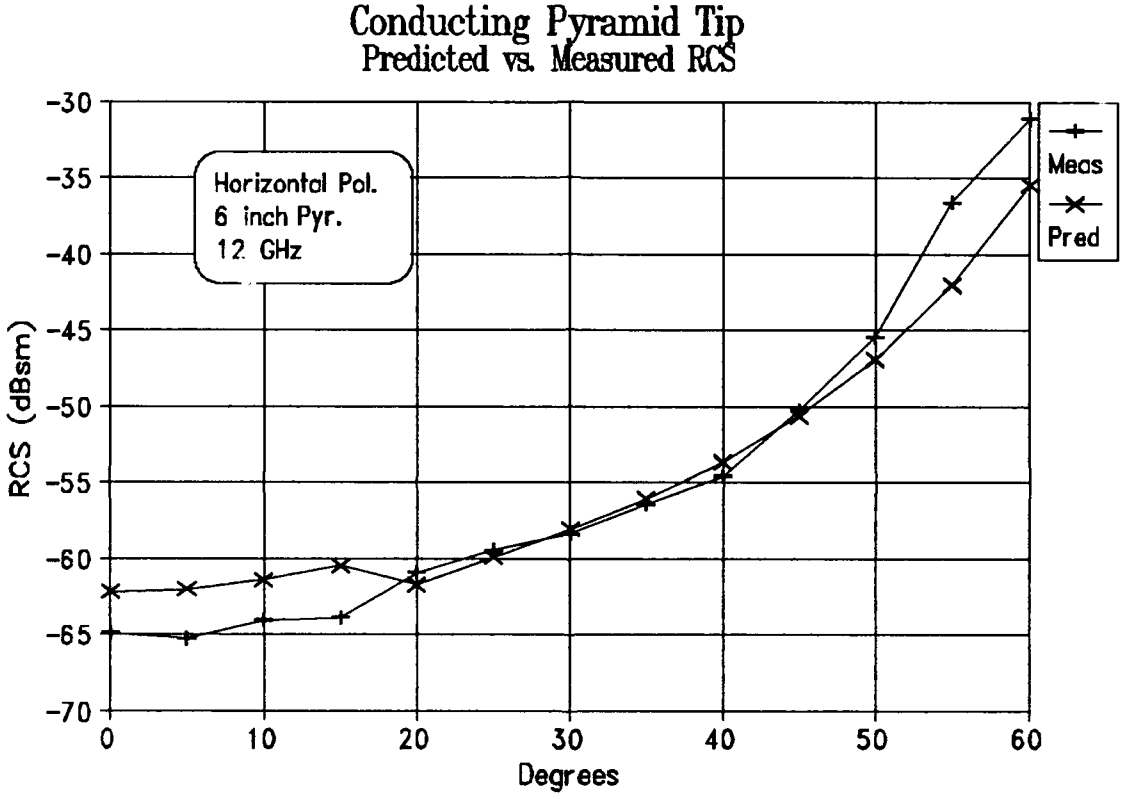

Figure 19. Predicted and Measured Backscatter from a 6-inch Conducting Pyramid as Azimuth Varies (12 Ghz, HH Pol.).

Figure 20 shows the predicted and measured scattering from a 12 inch pyramid as azimuth varies for a horizontally polarized incident field. Even though there is more error introduced (primarily due to signal levels being nearly 10 decibels less), the agreement is unmistakable. This figure shows that the agreement extends over the entire range of unambiguous measurement.

By contrast, prediction and measurement have their best agreement at azimuths near nose-on incidence for vertical polarization. This is shown in Figure 21 and Figure 22. Figure 21 shows the predicted and measured tip scattering for a conducting 6-inch pyramid at 12 Ghz with the incident field vertically polarized. The average difference again is under 2 decibels from 0 to 25 degrees. The predicted and measured values diverge at greater azimuths. This pattern is seen also in Figure 22. The difference increases steadily over the range from 10 to 30 degrees. For azimuths from 30 degrees to approximately 7 degrees below the maximum unambiguous azimuth measurement angle, the measurement is approximately 10 decibels below the prediction. It is seen that the difference is fairly constant over that region; the shape of the prediction is correct, but the level is wrong. This property is also seen in Figure 21, if the anomaly at 40 degrees is discounted.

The accuracy of the prediction of the azimuth response thus appears to depend on the actual azimuth region and the

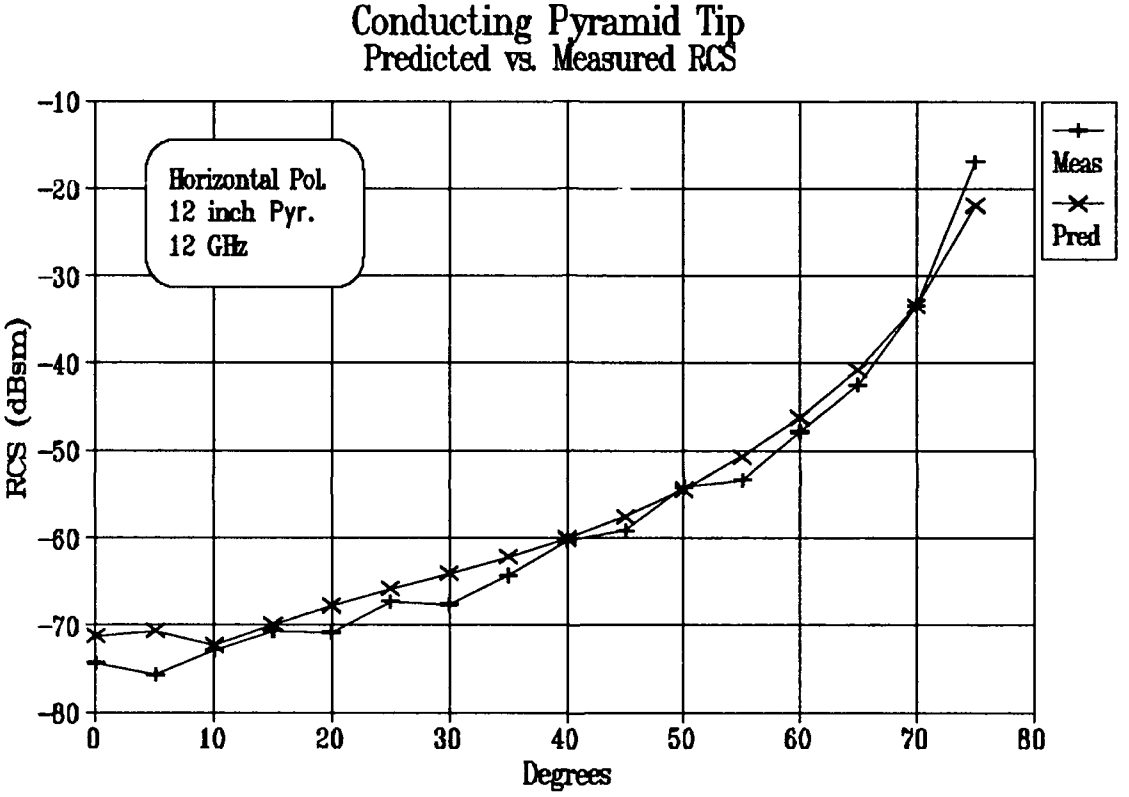

Figure 20. Predicted and Measured Backscatter from a 12-inch Conducting Pyramid as Azimuth Varies (12 Ghz, HH Pol.).

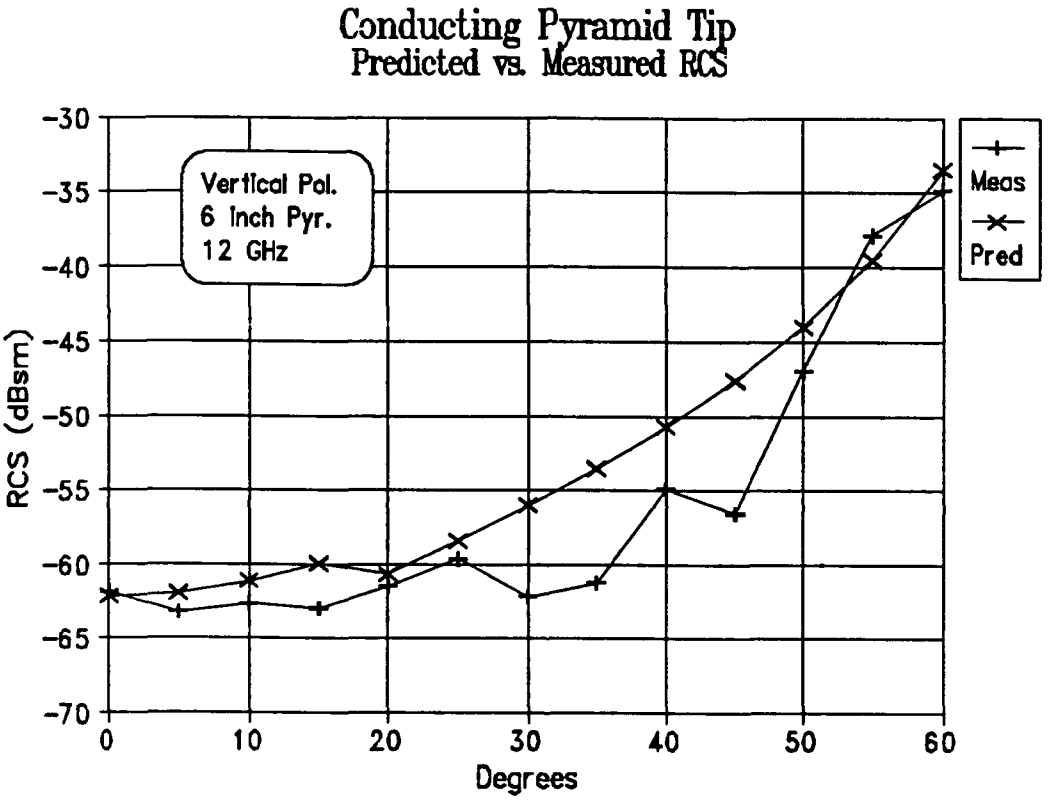

Figure 21. Predicted and Measured Backscatter from a 6-inch Conducting Pyramid as Azimuth Varies (12 Ghz, VV Pol.).

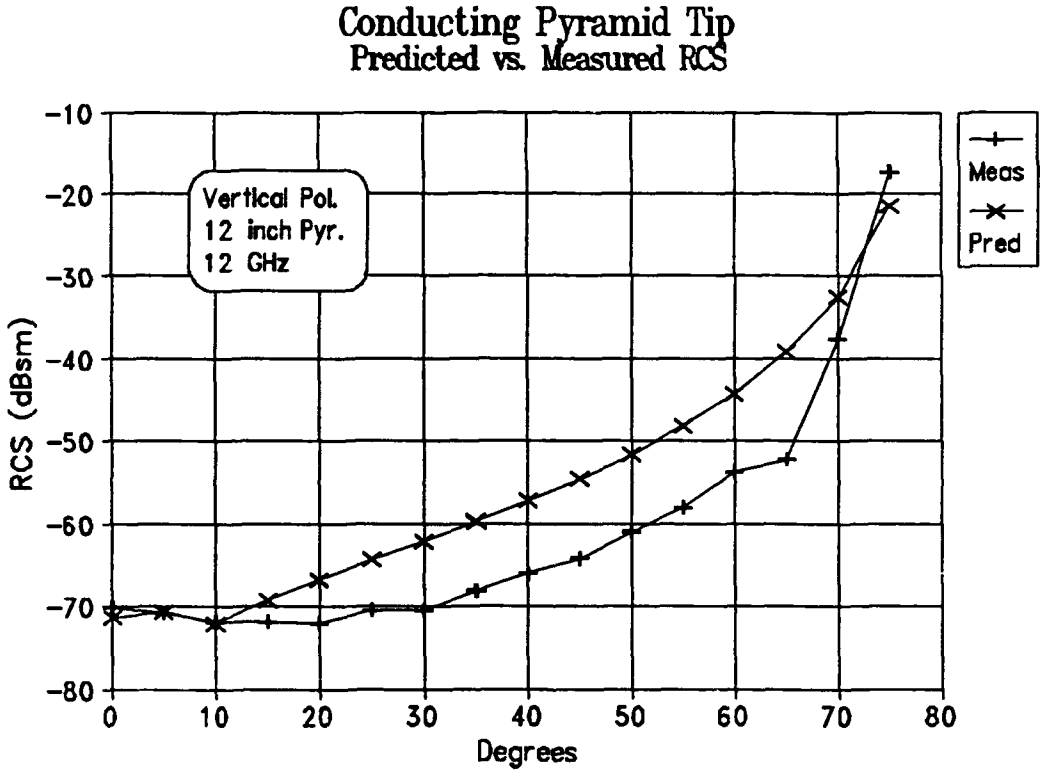

Figure 22. Predicted and Measured Backscatter from a 12-inch Conducting Pyramid as Azimuth Varies (12 Ghz, VV Pol.).

polarization of the incident field. In the region near nose-on incidence, for the size pyramids measured and at center frequency, both polarizations give predictions accurate to within 3 decibels. In the region away from nose-on incidence (beginning at about 20 to 25 degrees) the accuracy of the response is better or worse depending on the polarization of the incident field: horizontally polarized fields match the prediction even better than in the nose-on region; vertically polarized fields differ quite substantially from the predictions, yet still follow the overall prediction pattern.

4.2.2 Solution Accuracy as Pyramid Tip Angle Varies. This section is concerned with the agreement between prediction and measurement as pyramid size (angle) varies for a given fixed frequency, at a given incidence angle.

Figure 23 shows how the average accuracy of the predictions vary with pyramid size and for two azimuth sectors for horizontally polarized fields. The relative accuracy in the higher azimuth sector under horizontal polarization is evident in this figure as well. The only finding is that the 10 inch pyramid gave the least accurate results. This could be due to alignment error during measurement however, and does not necessarily indicate a trend.

Figure 24 shows how the average accuracy of the predictions vary for the same two azimuth sectors for

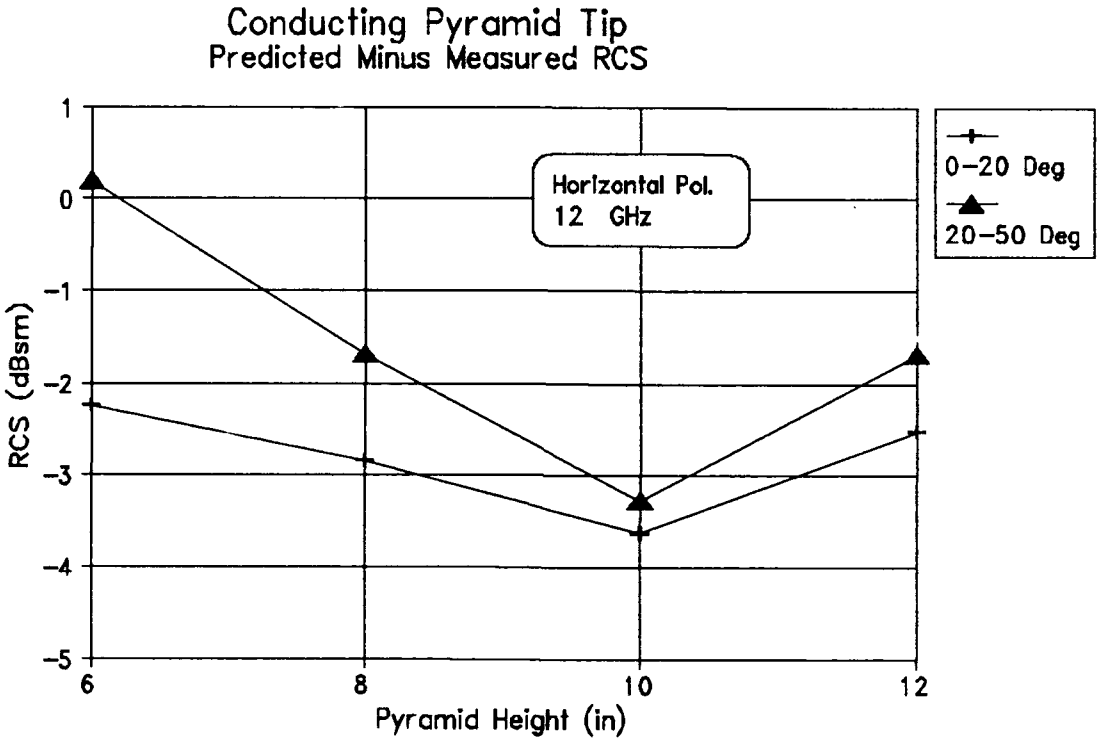

Figure 23. Average Difference Between Predicted and Measured Backscatter as Pyramid Size Varies (Conducting, 12 Ghz, HH Pol.).

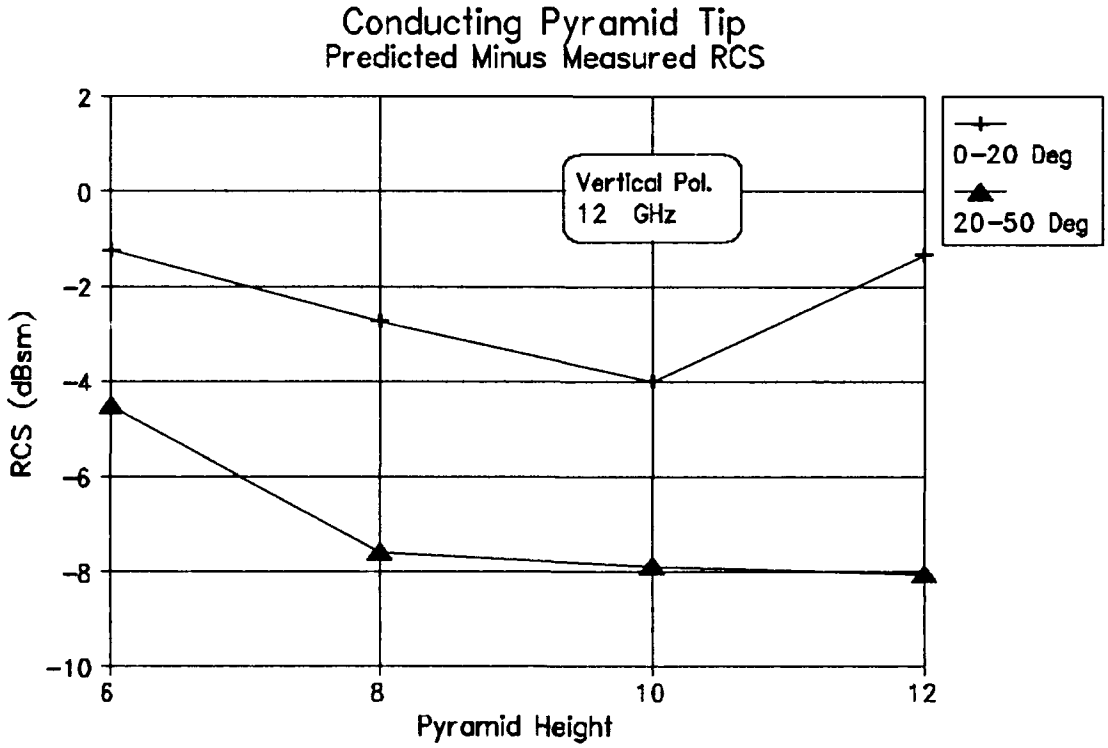

Figure 24. Average Difference Between Predicted and Measured Backscatter as Pyramid Size Varies (Conducting, 12 Ghz, VV Pol.).

vertically polarized fields. Note however that the scaling is twice that of Figure 23. Again, no solid relationship between pyramid height and accuracy is evidenced.

Figure 25 shows the predicted scattering for both polarizations at nose-on incidence. The horizontal scattering nearly exactly follows the prediction, but at a level 3 decibels lower. The vertical measurement is approximately equal to the prediction for the 6 inch pyramid, diverges from the prediction for the 8 inch and 10 inch pyramids, and exceeds the prediction for the 12 inch pyramid. No conclusion is made about the vertically polarized scattering results other than to take notice of the overall inaccuracy.

4.2.3 Solution Accuracy as Frequency Varies. Figure 26 shows the predicted backscatter for different size conducting pyramids at nose-on azimuth as frequency varies. This response is monotonic, decreasing as frequency increases. The relative values of this response are invariant; if the predicted response for a given pyramid size, azimuth and frequency are known, the frequency response for any other frequency may be found by scaling these curves to the value at the given frequency.

Figure 27 and Figure 28 show the predicted and measured frequency responses of the 12 inch pyramid for horizontal polarization at 5 degrees and 50 degrees azimuth. The low aspect angle comparison shows that the measured value is a

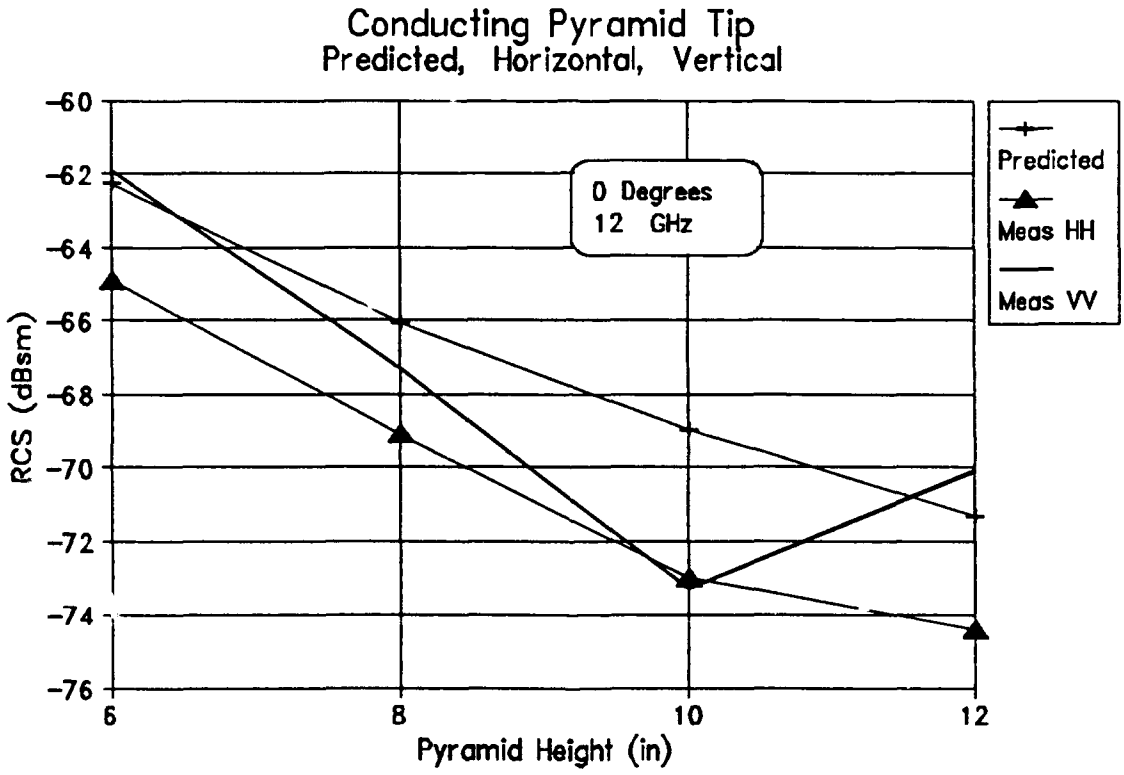

Figure 25. Predicted and Measured Backscatter at Nose-on Incidence for Various Height Conducting Pyramids.

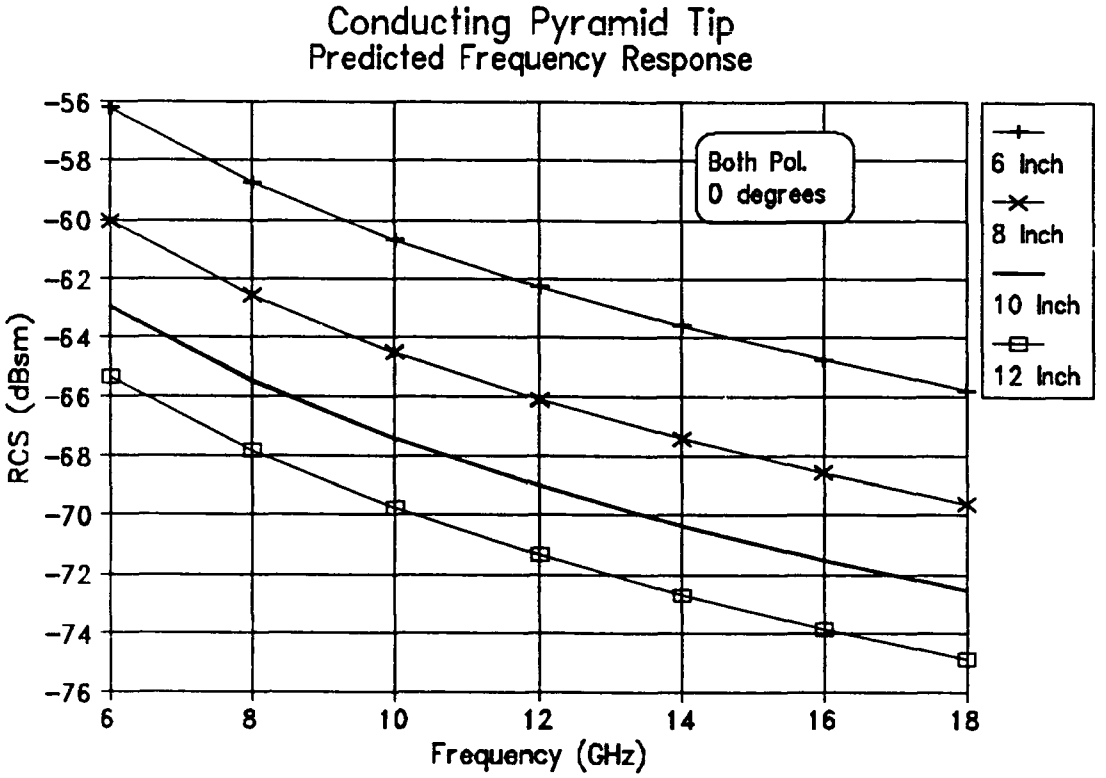

Figure 26. Predicted Frequency Response for Various Height Conducting Pyramids at Nose-on Incidence (Either Pol.).

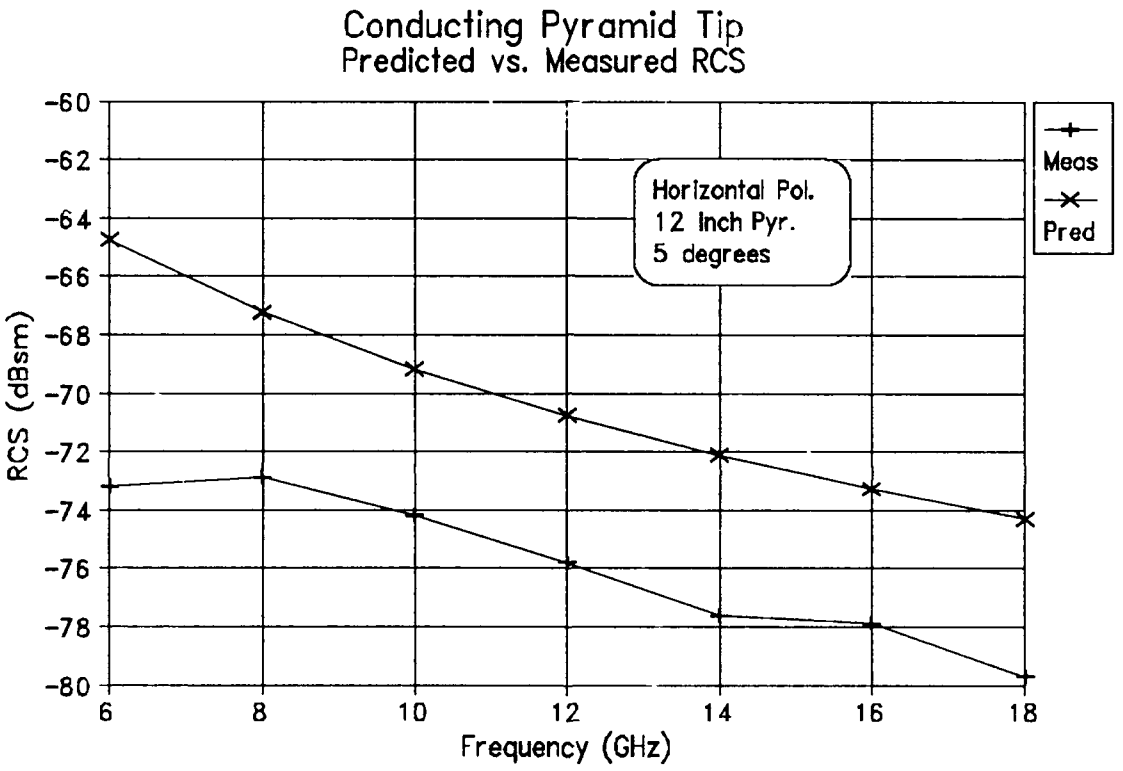

Figure 27. Predicted and Measured Frequency Response for a 12 Inch Pyramid at 5 Degrees Azimuth (HH Pol.).

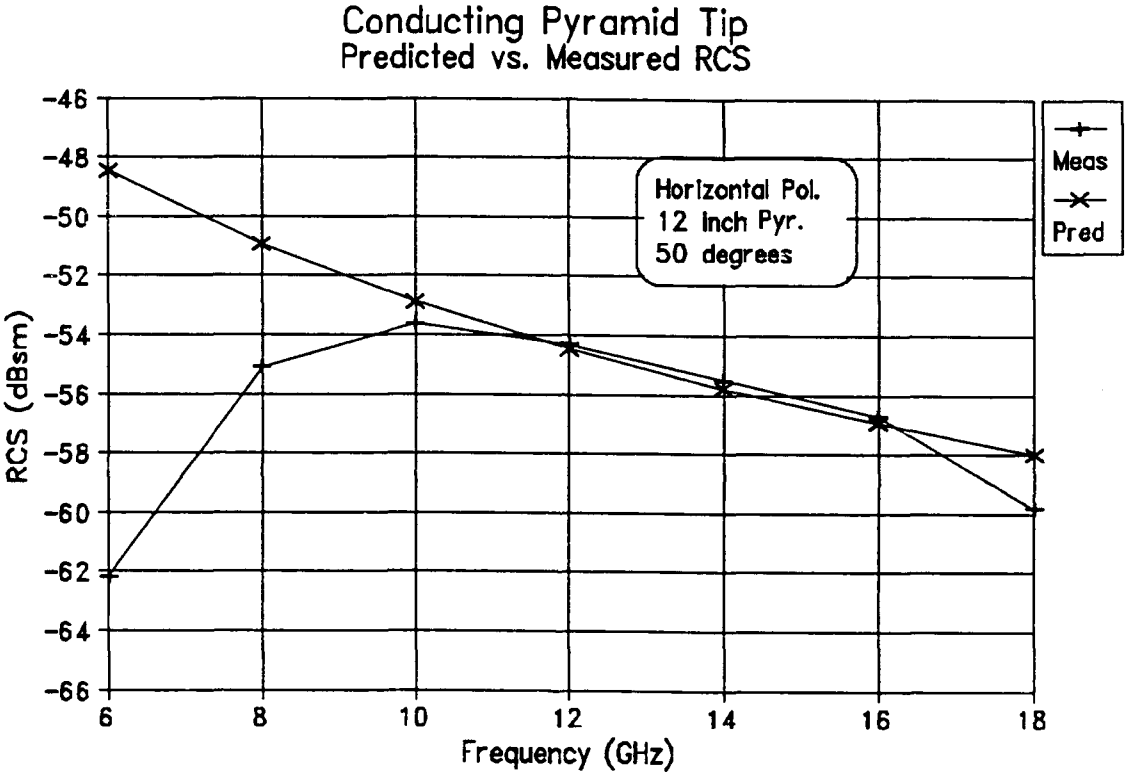

Figure 28. Predicted and Measured Frequency Response for a 12 Inch Pyramid at 50 Degrees Azimuth (HH Pol.).

nearly constant 5 decibels less than the prediction. Some roll-off is seen at both ends of the frequency spectrum; this is due to the fact that the frequency response is time gate limited. Figure 28 shows excellent (within 1 decibel) agreement for horizontally polarized fields incident at larger aspect angles. The frequency roll-off is much more evident at the lower frequencies. At first it was believed that the steeper roll-off might be due to a narrower time gate, since a narrower time gate is expected to produce more error at the extreme frequencies. In fact, the time gate used in Figure 28 was 0.39 nanoseconds, almost 40 percent longer than the gate used in Figure 27. The reason for the severe rolloff at low frequencies in Figure 28 is not known.

Figure 29 and Figure 30 use the same size pyramid and azimuth angles as Figure 27 and Figure 28, but with vertical polarization. Figure 29 shows excellent agreement over the entire range of frequencies measured (allowing for roll-off at 6 Ghz and 18 Ghz). However, as Figure 30 shows, the agreement is poor at higher aspect angles. The argument may be made that the measured frequency response still has the same form as the predicted response, but it is a full order of magnitude (10 decibels) lower.

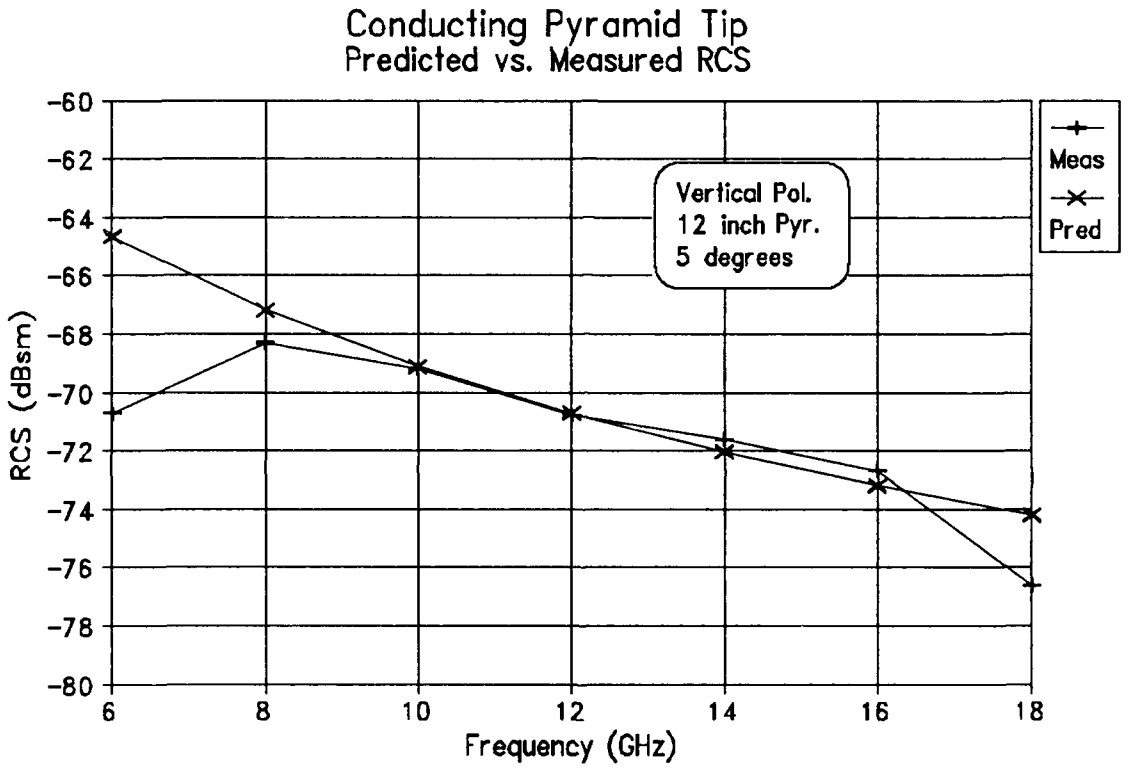

Figure 29. Predicted and Measured Frequency Response for a 12 Inch Pyramid at 5 Degrees Azimuth (VV Pol.).

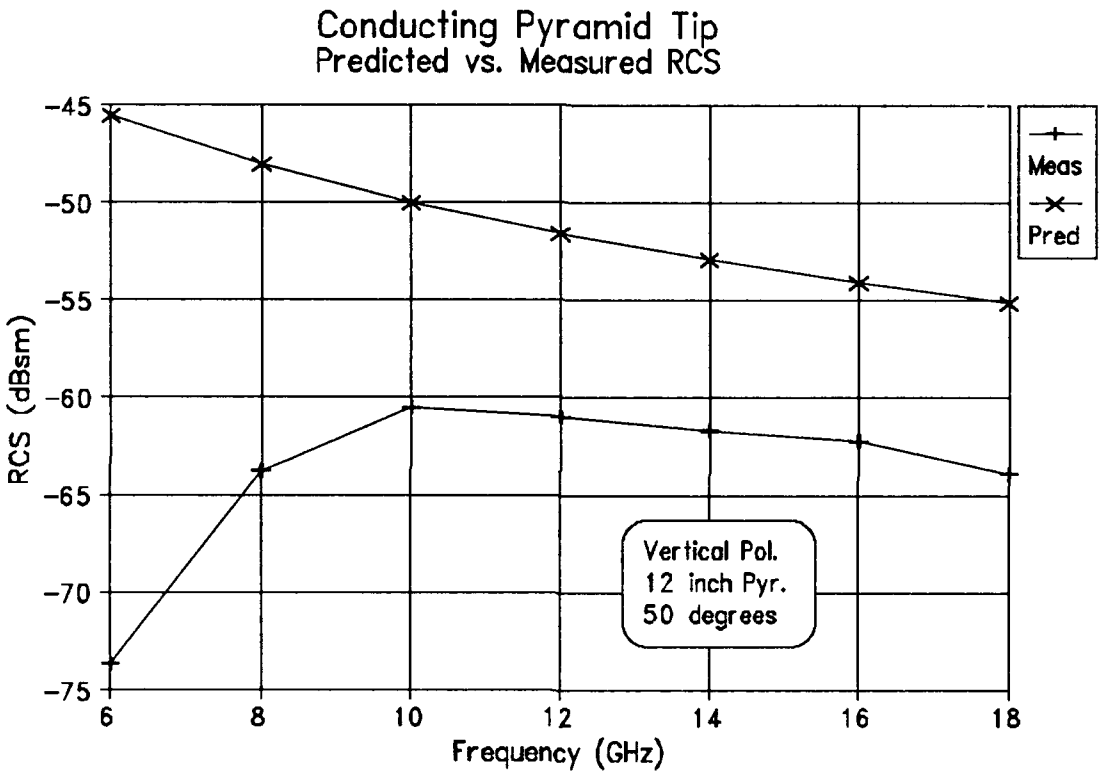

Figure 30. Predicted and Measured Frequency Response for a 12 Inch Pyramid at 50 Degrees Azimuth (VV Pol.).

4.3 Lossless Dielectric Pyramid

This section is concerned with the measurement, prediction and analysis of the scattering from the tips of lossless dielectric pyramids. Through comparison of prediction and measurement for these scatterers, and by relating the comparisons to the results found for conducting pyramid tips, the effect of the dielectric assumptions may be determined.

4.3.1 Solution Accuracy as Aspect Angle Varies. Figure 31 through Figure 34 show the measured and predicted backscatter levels as a function of azimuth for each of the pyramid tips. This data represents the co-polarized return at center frequency (12 Ghz) under horizontal polarization. A review of these figures shows several common characteristics. From nose-on incidence to 20 degrees azimuth the predicted level is nominally (2 to 5 decibels) higher than the measured level of backscatter. An exception to this is seen at 5 degrees azimuth (all figures), where the measured levels diverge from the prediction. In the azimuth region greater than 20 degrees, the measurement tracks the predicted levels, but the level of agreement appears dependent on the pyramid size. (This dependence is discussed more appropriately in Section 4.3.2).

It is interesting to note in Figure 31 that the agreement between prediction and measurement extends past the maximum unambiguous azimuth angle (57.8 degrees) and

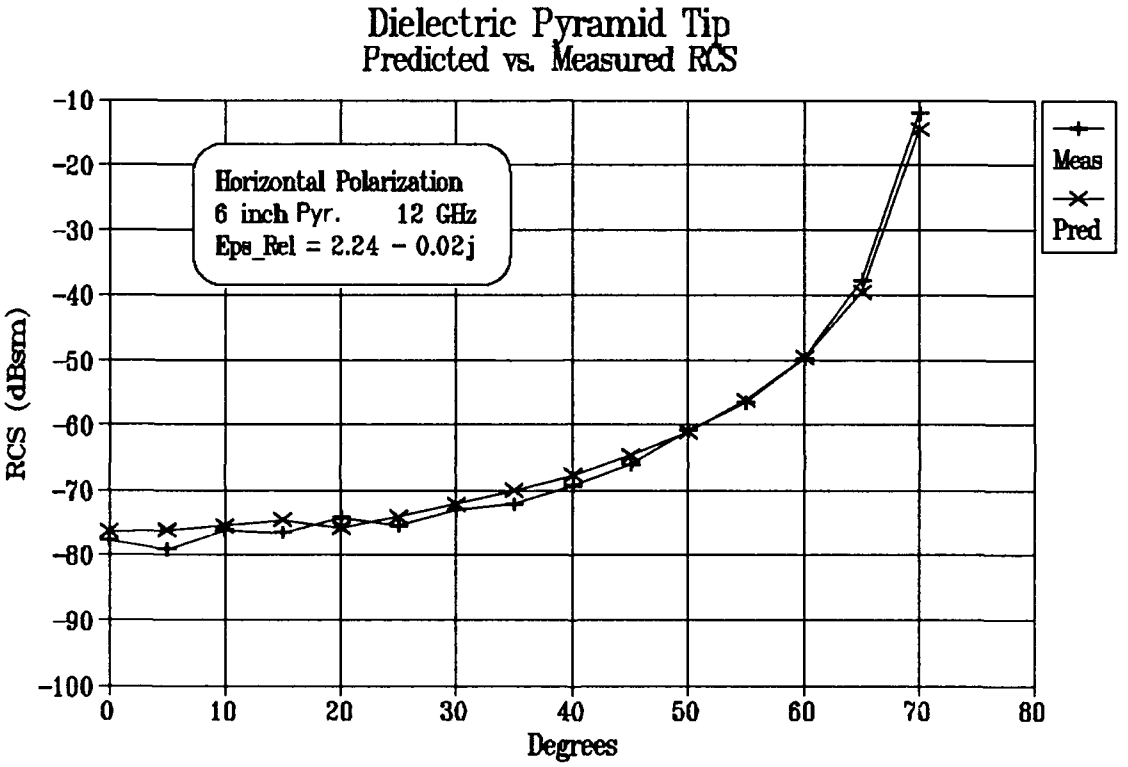

Figure 31. Predicted and Measured Backscatter from a 6-inch Poly Pyramid as Azimuth Varies (12 Ghz, HH Pol.).

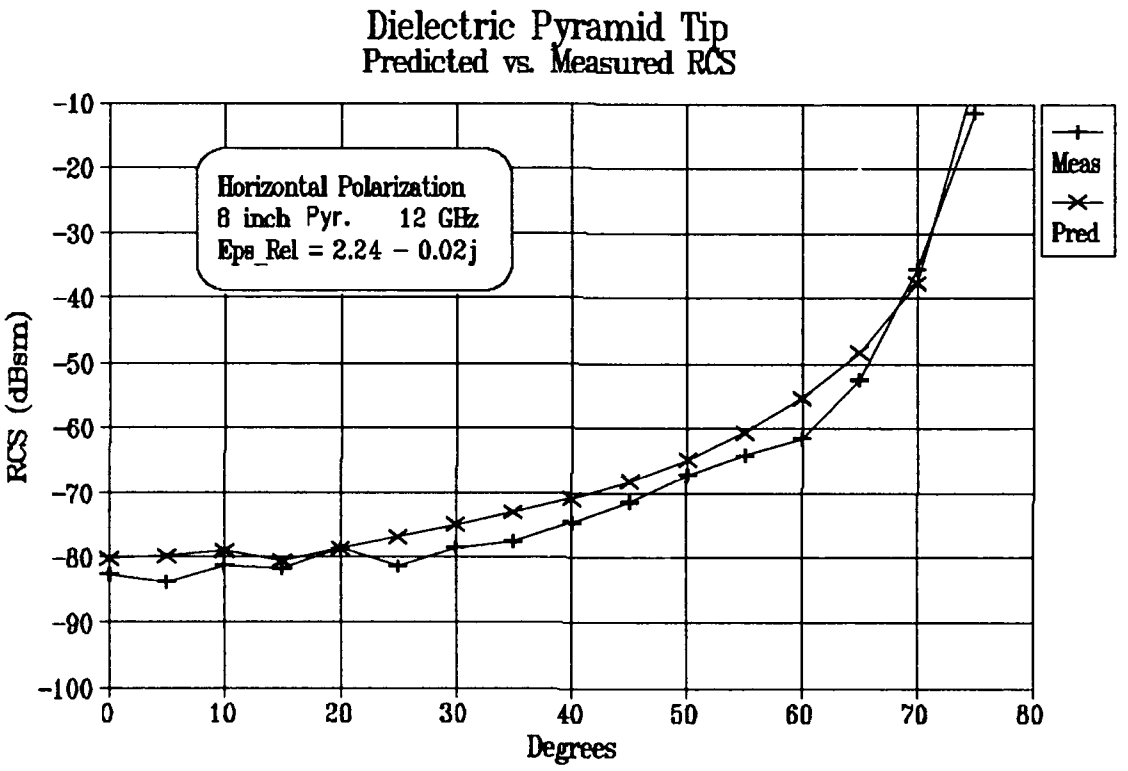

Figure 32. Predicted and Measured Backscatter from an 8-inch Poly Pyramid as Azimuth Varies (12 Ghz, HH Pol.).

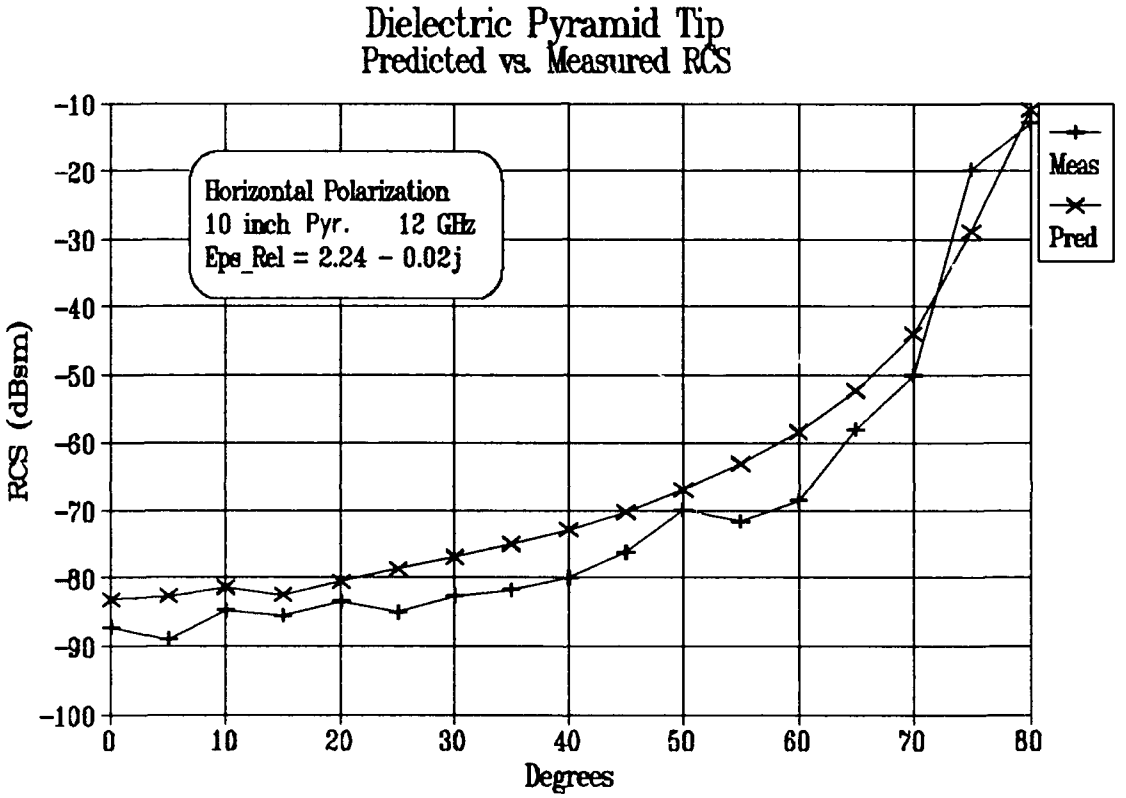

Figure 33. Predicted and Measured Backscatter from a 10-inch Poly Pyramid as Azimuth Varies (12 Ghz, HH Pol.).

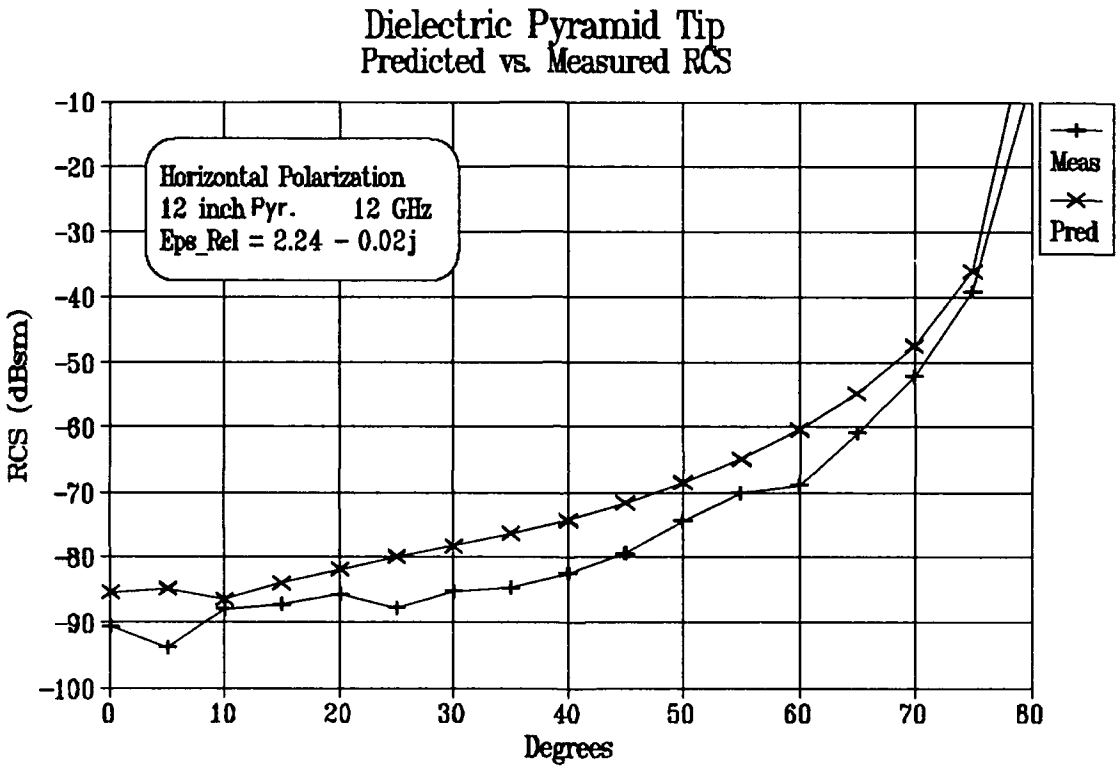

Figure 34. Predicted and Measured Backscatter from a 12-inch Poly Pyramid as Azimuth Varies (12 Ghz, HH Pol.).

agrees up to a point where the tip return and base returns should overlap (70.5 degrees). Beyond 50 degrees the tip return starts to blend in with the base return. Figure 35 shows that it cannot be visually determined with any certainty where the tip return ends and the base return begins. However, the determination of the return time gate is based on locating a relative maximum in the frequency response, not from any visual location of a null in the time domain response. This attests to the autocorrelative nature of the time gate determination process. Of course, while the procedure is apparently centering the time gate on the pyramid tip return, backscattered energy from the pyramid base is also included in the time gate.

The plots of predicted and measured backscatter under vertically polarized fields are shown in Figure 36 through Figure 39. Again, a nominal difference is seen between measurement and prediction the 0 to 20 degree azimuth range. Notably absent in measured values is the dip at 5 degrees seen in each of the horizontally polarized graphs (Figure 31 through Figure 34); the exception, Figure 39 is into the measurement system noise floor. In the azimuth region greater than 20 degrees, the predictions again track the measurements. The distinction between the nominal agreement region and the tracking region for vertical polarization is not as well defined as it is for the case of horizontal polarization. Indeed, if not compared to the

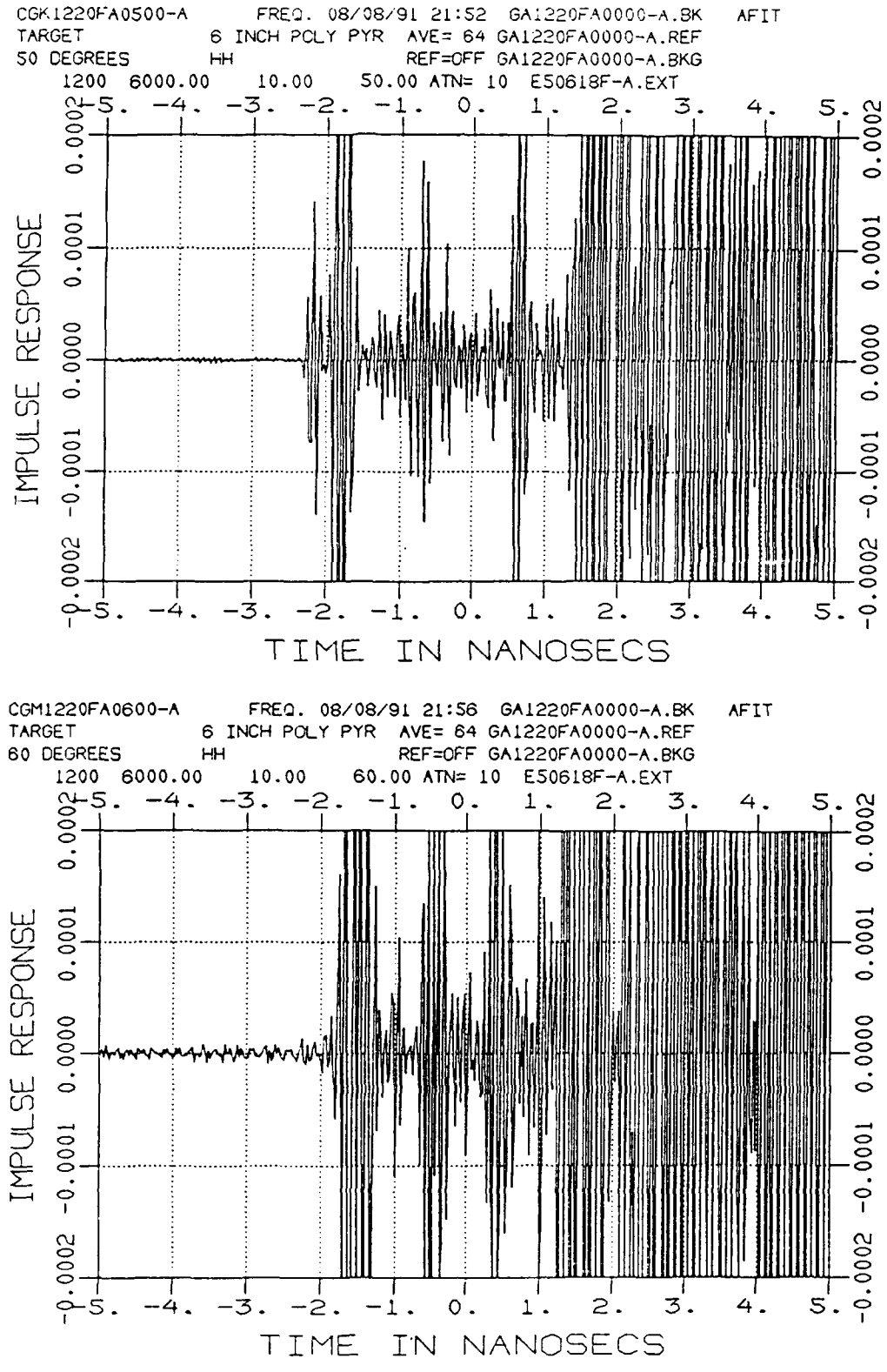

Figure 35. Time Domain Plots of the 6-inch Poly Test Body at 50 and 60 Degrees (HH Pol.).

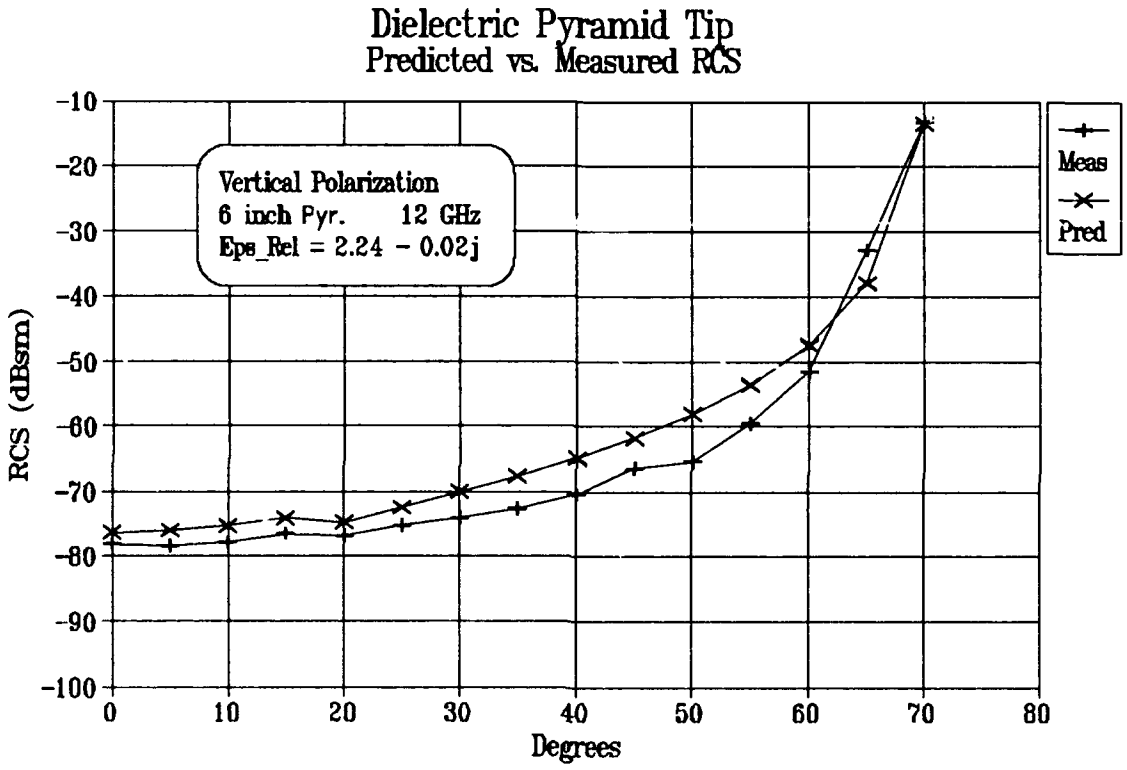

Figure 36. Predicted and Measured Backscatter from a 6-inch Poly Pyramid as Azimuth Varies (12 Ghz, VV Pol.).

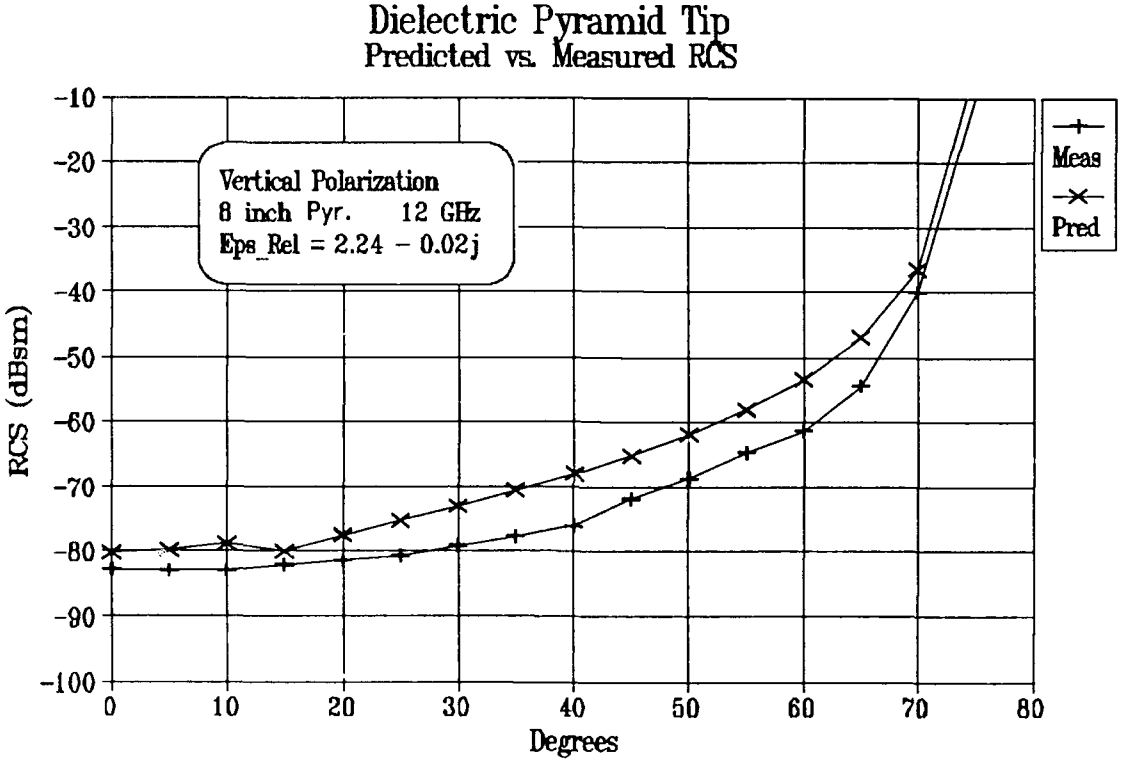

Figure 37. Predicted and Measured Backscatter from an 8-inch Poly Pyramid as Azimuth Varies (12 Ghz, VV Pol.).

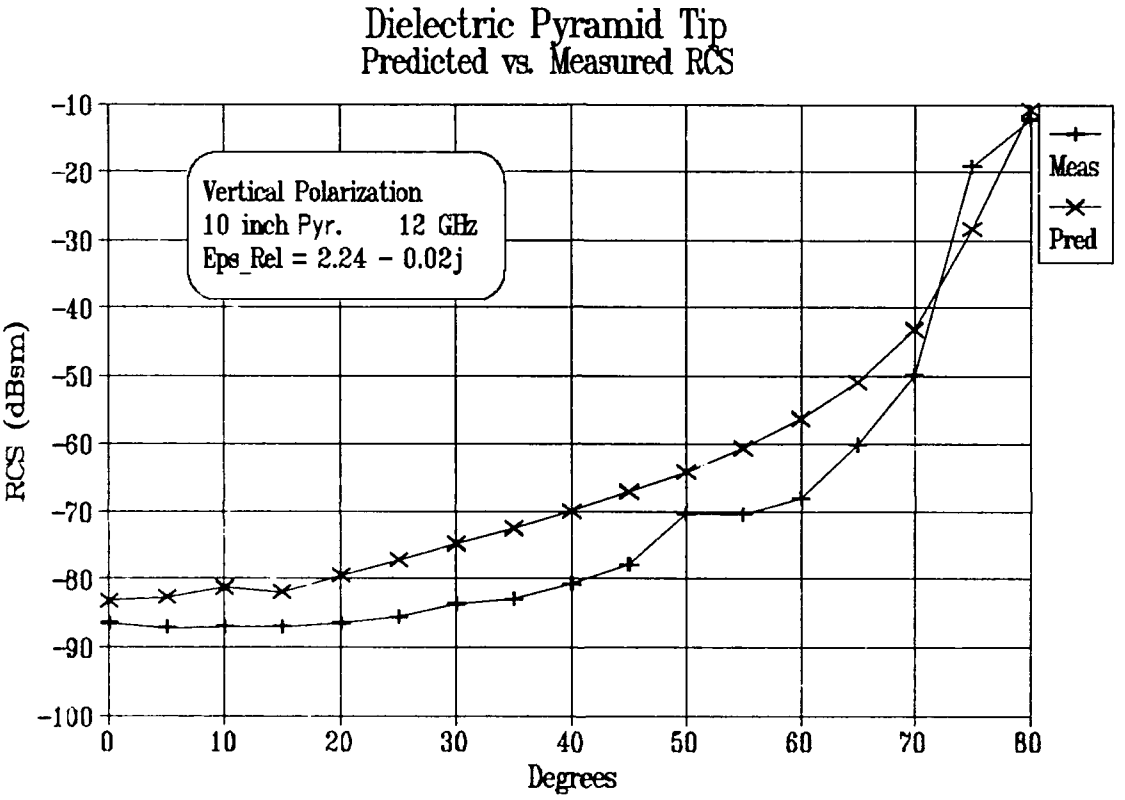

Figure 38. Predicted and Measured Backscatter from a 10-inch Poly Pyramid as Azimuth Varies (12 Ghz, VV Pol.).

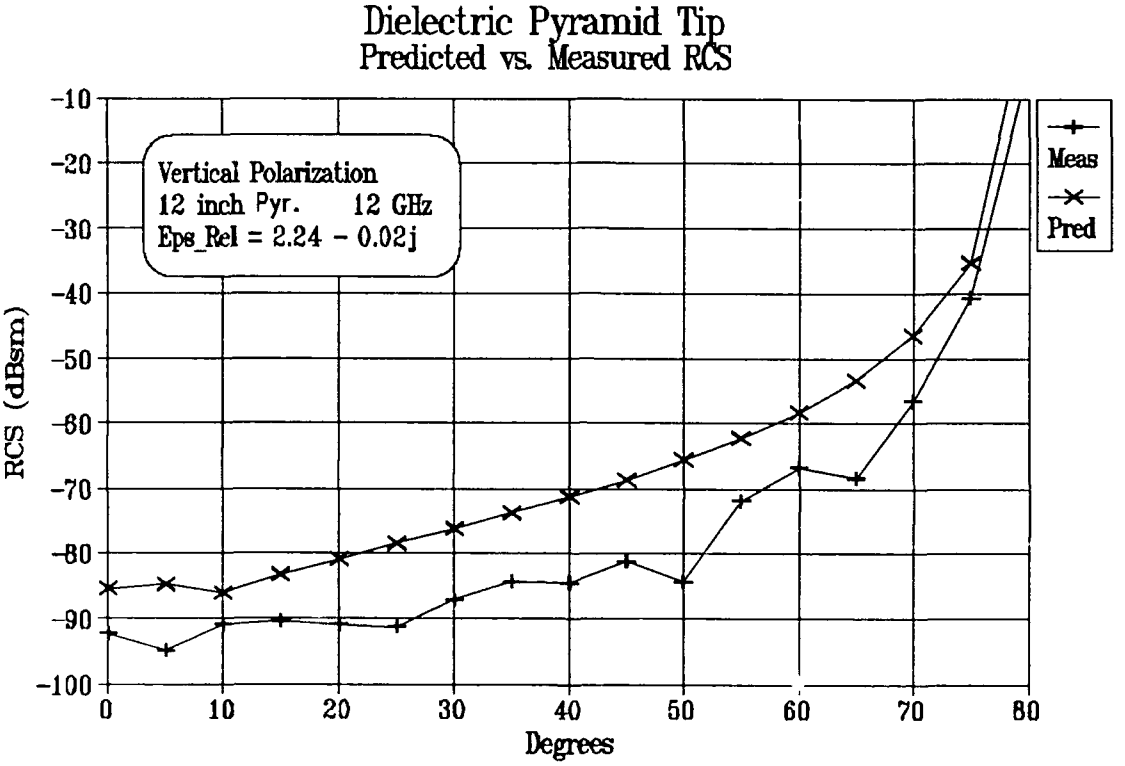

Figure 39. Predicted and Measured Backscatter from a 12-inch Poly Pyramid as Azimuth Varies (12 Ghz, VV Pol.).

horizontal polarization case, the distinction between the regions would probably go unnoticed. Again the agreement between prediction and measurement seems to be a function of pyramid size.

For conducting pyramids at higher azimuths, the predictions for backscatter levels under horizontal polarization were significantly more accurate than the predictions for vertical polarization. The data presented in this section shows that for the case of a dielectric pyramid tip at larger azimuths, although polarization still has some effect, pyramid size (tip angle) is more important in determining the level of agreement between prediction and measurement. This relationship will be explored in the next section.

4.3.2 Solution Accuracy as Pyramid Tip Angle Varies. In the previous section, the observation was made that the prediction accuracy appears to be a function of the pyramid tip angle. This observation is explored further in this section.

Figure 40 shows the average difference between measurement and prediction for horizontal polarization in the two azimuth sectors as a function of pyramid size. This graph shows a clear relationship between pyramid size and accuracy. In the nose-on azimuth sector (0 to 20 degrees) the accuracy steadily declines as the tip angle decreases (pyramid height increases). In the azimuth sector farther

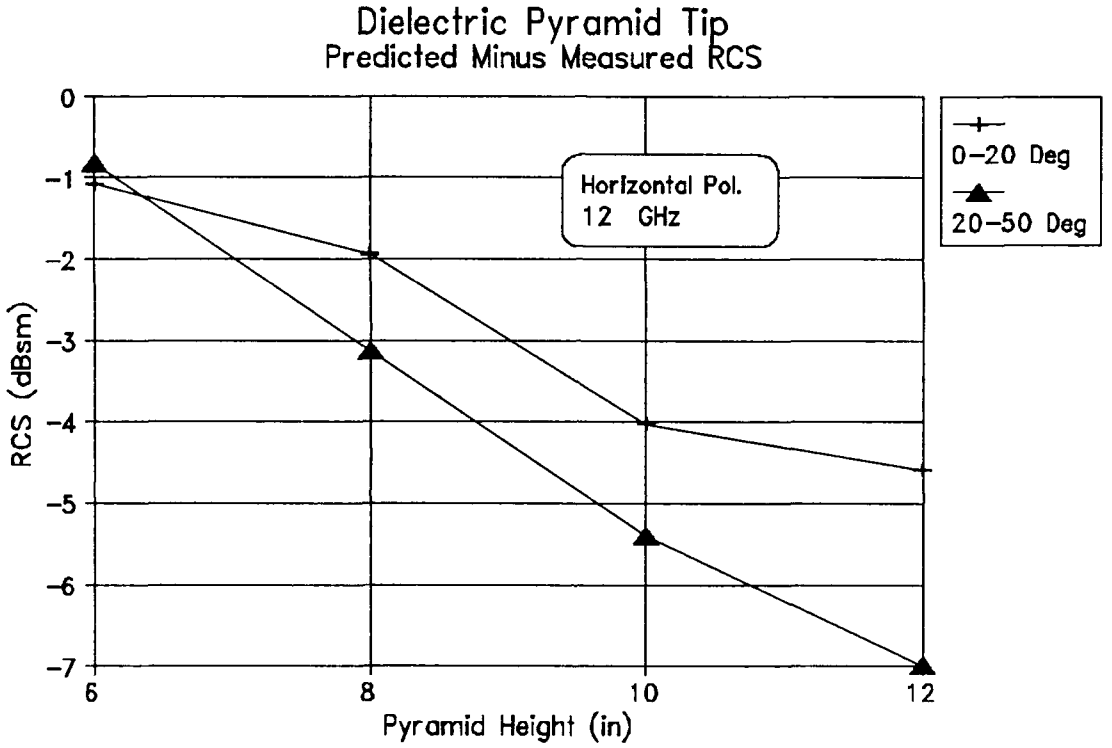

Figure 40. Average Difference Between Predicted and Measured Backscatter as Pyramid Size Varies (Poly, 12 Ghz, HH Pol.).

from nose-on incidence (20 to 50 degrees), the error is nearly a linear function of pyramid height. It should also be observed that for dielectric pyramid tips the prediction in the greater azimuth sector is less accurate than in the near nose-on azimuth sector; this is in direct contrast to the conducting pyramid case (Figure 23) where predictions in the greater azimuth sector are more accurate.

Figure 41 shows the mean error in the same azimuth sectors under vertical polarization. As with the case of a horizontally polarized dielectric pyramid tip, the prediction accuracy steadily degrades as the pyramid tip angle becomes more acute. As with the case of the vertically polarized conducting pyramids, the accuracy is decidedly worse at higher azimuth angles. In the case of vertical polarization incident on the 12-inch dielectric pyramid between 20 and 50 degrees, these two effects reinforce each other; the mean error is nearly 13 decibels.

Figure 42 shows the predicted and measured backscatter for both polarizations at nose-on incidence. As expected from the previous two graphs, the nominal error increases almost linearly with pyramid height. In Section 4.2.2, no conclusion could be made as to any correlation between pyramid tip angle and prediction accuracy for conducting pyramids. Clearly, the effect of degraded accuracy at acute pyramid tip angles is a function of the dielectric material.

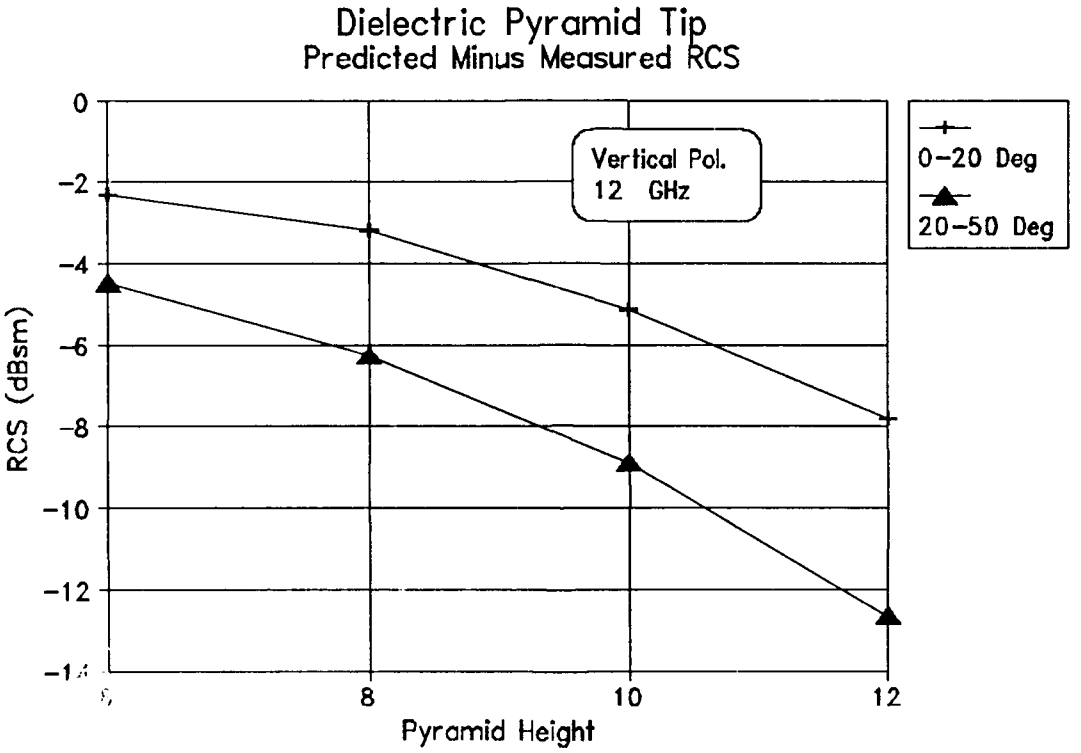

Figure 41. Average Difference Between Predicted and Measured Backscatter as Pyramid Size Varies (Poly, 12 GHZ, VV Pol.).

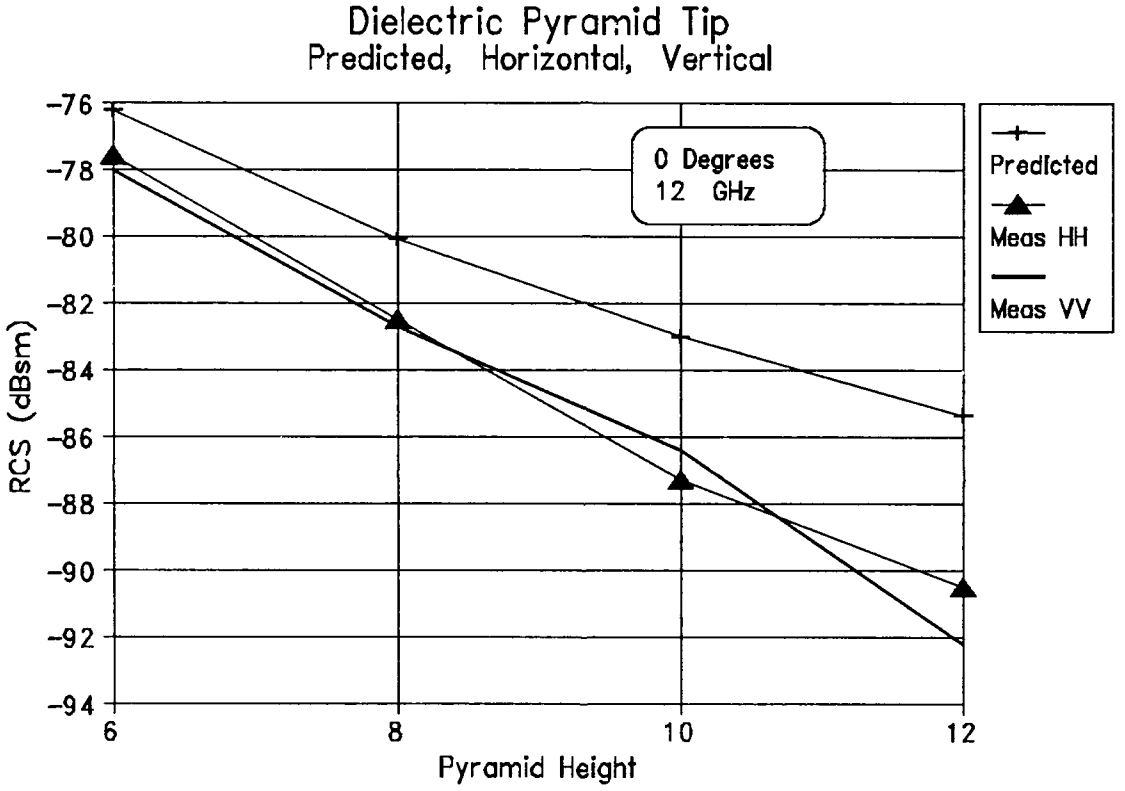

Figure 42. Predicted and Measured Backscatter at Nose-on Incidence for Various Height Poly Pyramids.

4.3.3 Solution Accuracy as Frequency Varies. The predicted frequency response of the 4 dielectric pyramids at nose-on incidence are shown in Figure 43. These curves are similar to those for conducting pyramid tips (Figure 26) but are 14 decibels lower. This overall lowering of the signal levels makes the measurement more susceptible to noise. Figure 44 shows a typical noise floor measurement for the Poly pyramids. As the figure shows, the noise floor level is highest at the high- and low-frequency extremes. This noise is evident in the frequency response graphs shown in this section and is manifested as wildly varying signal levels at the ends of the frequency spectrum (as opposed to the smoother roll-off seen for the conducting tips). However, the noise floor levels in the center frequency band are typically 10 decibels or more below the predicted values for all poly cases. As a result, the frequency response analysis will be limited to the frequency band between 10 Ghz and 14 Ghz.

Figure 45 and Figure 46 show the predicted and measured backscatter for the 6-inch and 8-inch dielectric pyramids under horizontal polarization. The responses are for a 5 degree azimuth angle and are typical of each of the dielectric pyramid tips under horizontal polarization near nose-on azimuth. Figure 45 shows that the 6-inch pyramid tip frequency response tracks the prediction fairly well; Figure 46 shows a dip in the measured response between 10

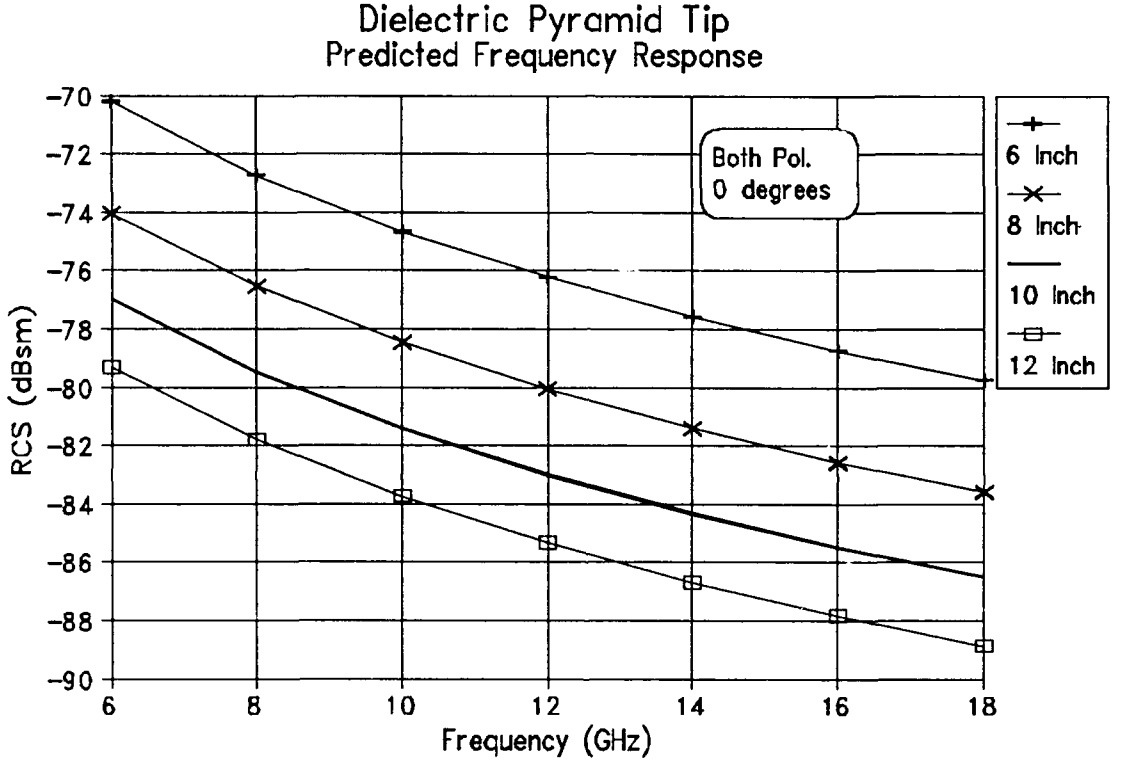

Figure 43. Predicted Frequency Response for Various Height Poly Pyramids at Nose-on Incidence (Either Pol.).

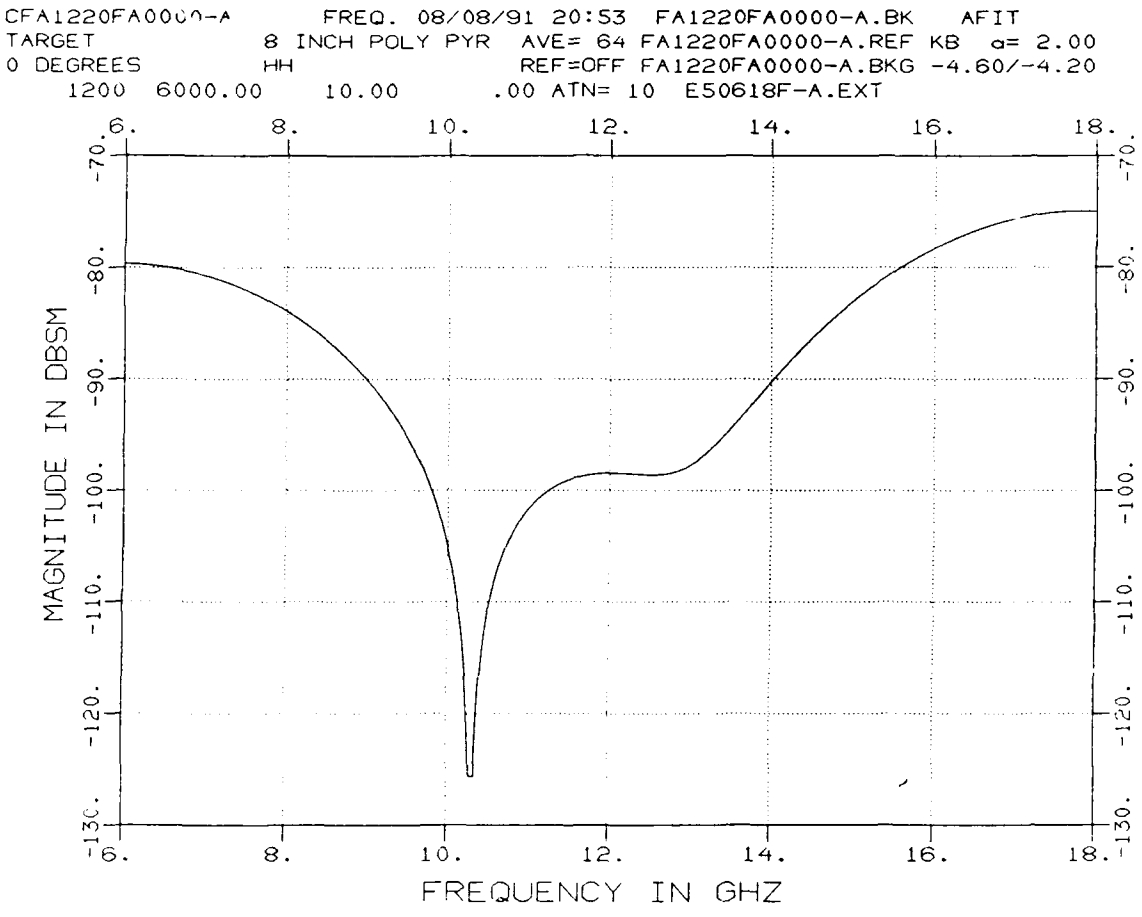

Figure 44. Noise Floor Measurement for 8-inch Poly Pyramid at 0 Degrees Azimuth Using Standard Time Gate Width (HH Pol.)

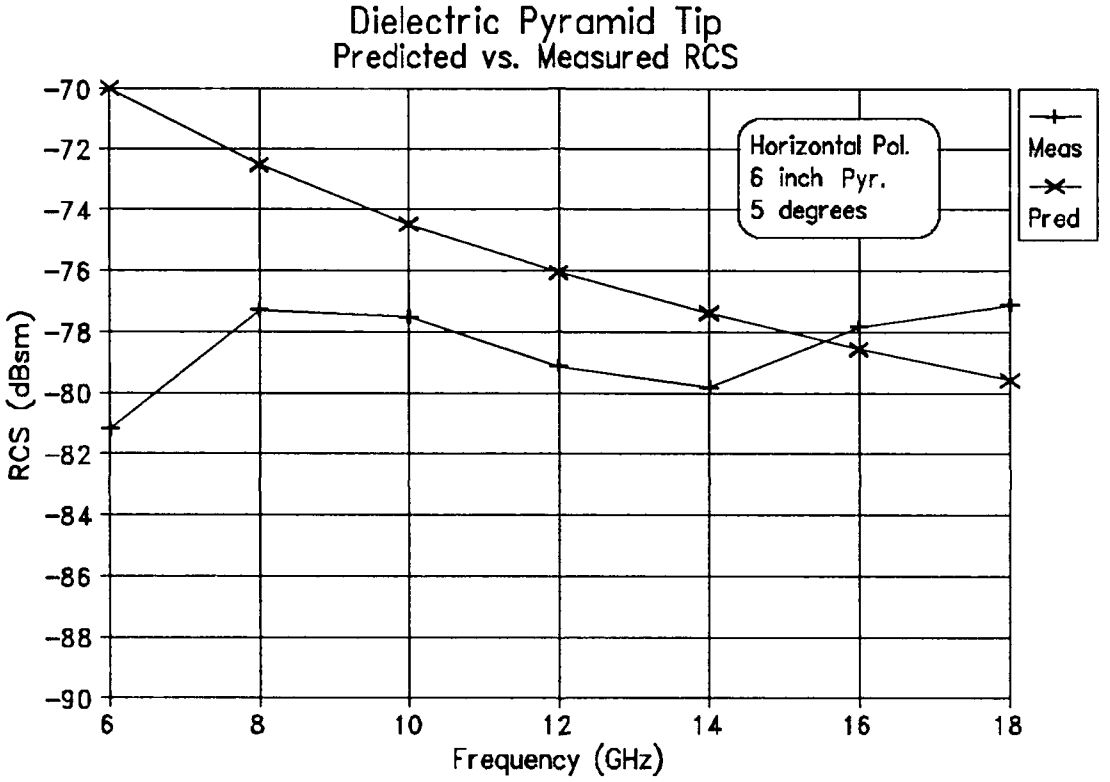

Figure 45. Predicted and Measured Frequency Response for a 6-inch Poly Pyramid at 5 Degrees Azimuth (HH Pol.).

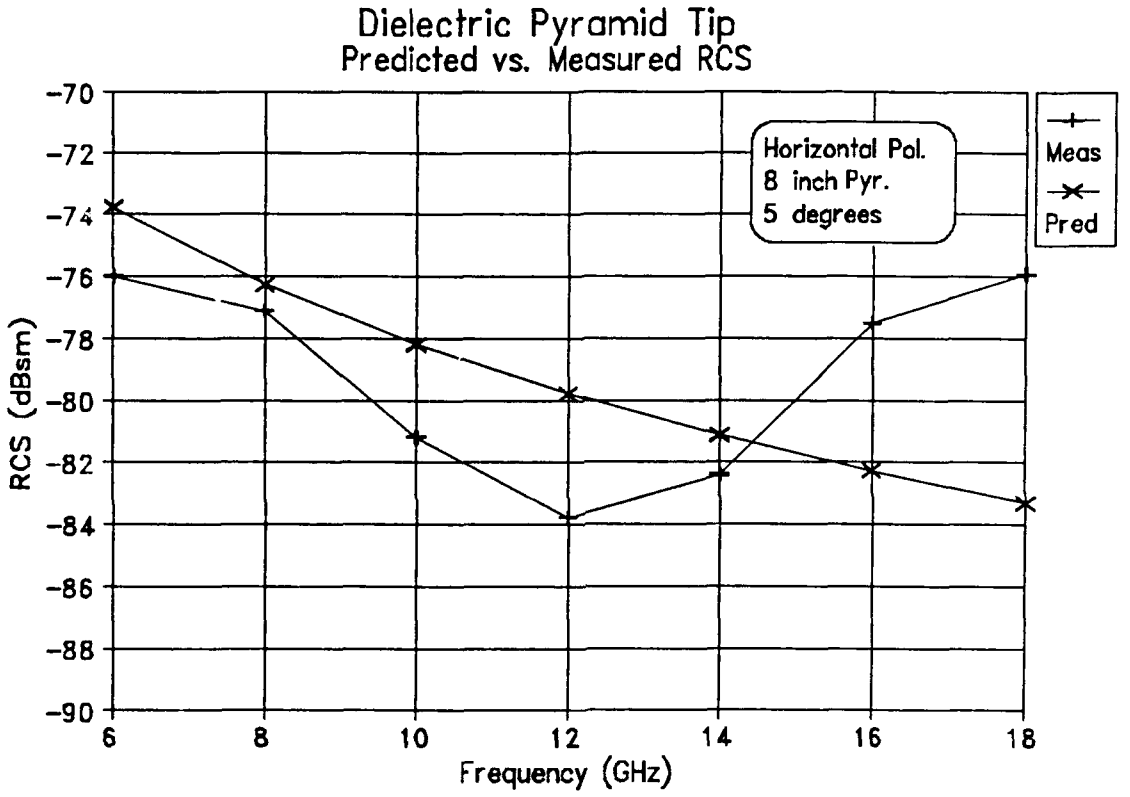

Figure 46. Predicted and Measured Frequency Response for a 8-inch Poly Pyramid at 5 Degrees Azimuth (HH Pol.).

Ghz and 14 Ghz. In this azimuth region, (0 to 20 degrees) under horizontal polarization, some pyramid tip frequency responses track the prediction and others do not track the prediction. There is no pattern or formula to determine if the measurement for a given pyramid tip angle and azimuth angle will track the prediction. This somewhat random tracking appears to be a characteristic of the response in the near nose-on azimuth region under horizontal polarization. The effect of the noise floor at the frequency extremes may be seen by comparing the response from 14 Ghz to 18 Ghz responses of Figure 44 and Figure 46.

Figure 47 through Figure 49 show the typical horizontally polarized frequency response in the larger azimuth range (20 to 50 degrees). In this range, agreement and tracking correspond to the pyramid tip angle. Figure 47 shows the close tracking and agreement between measurement and frequency response prediction for the 6-inch pyramid tip at 50 degrees azimuth. Figure 48 shows the response for a 10-inch pyramid tip; the tracking is less precise for this mid-size pyramid. Figure 49 shows the frequency response measurement and prediction for the 12-inch pyramid tip; the response is nearly flat from 10 Ghz to 14 Ghz. These three figures typify the agreement between measured and predicted frequency response for a horizontally polarized field incident on a dielectric pyramid tip in the greater azimuth range: short (6-inch) pyramids exhibit close agreement in

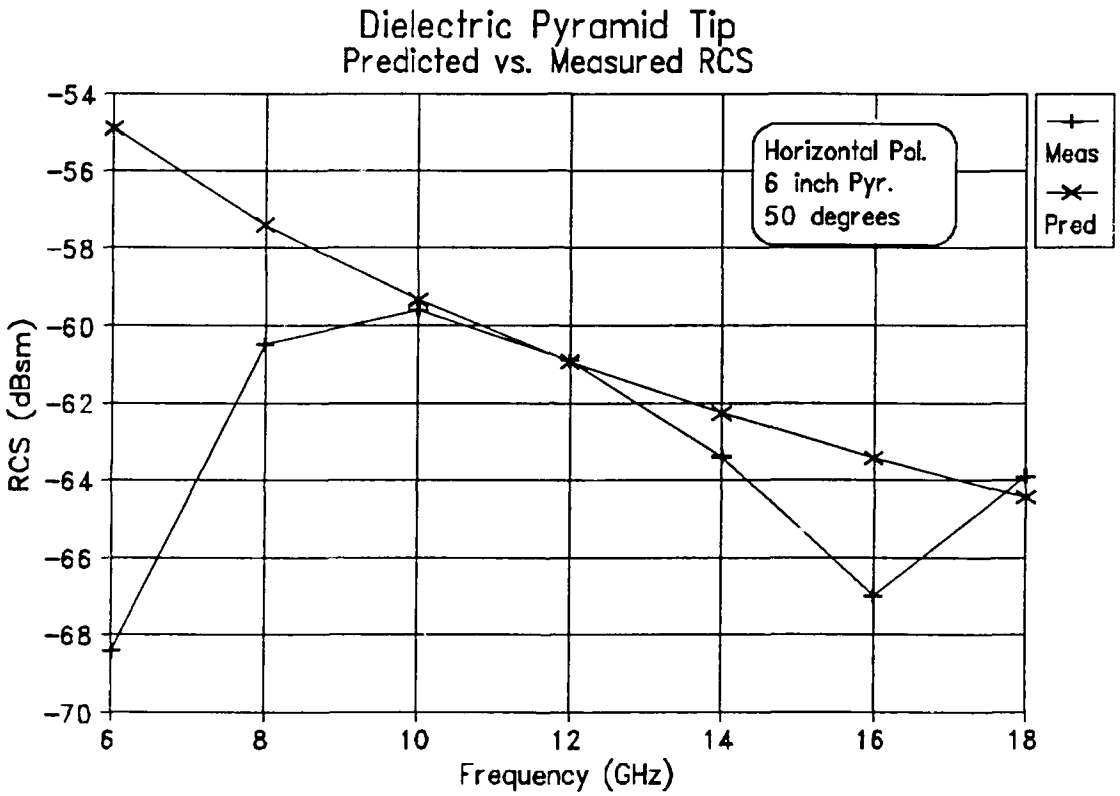

Figure 47. Predicted and Measured Frequency Response for a 6-inch Poly Pyramid at 50 Degrees Azimuth (HH Pol.).

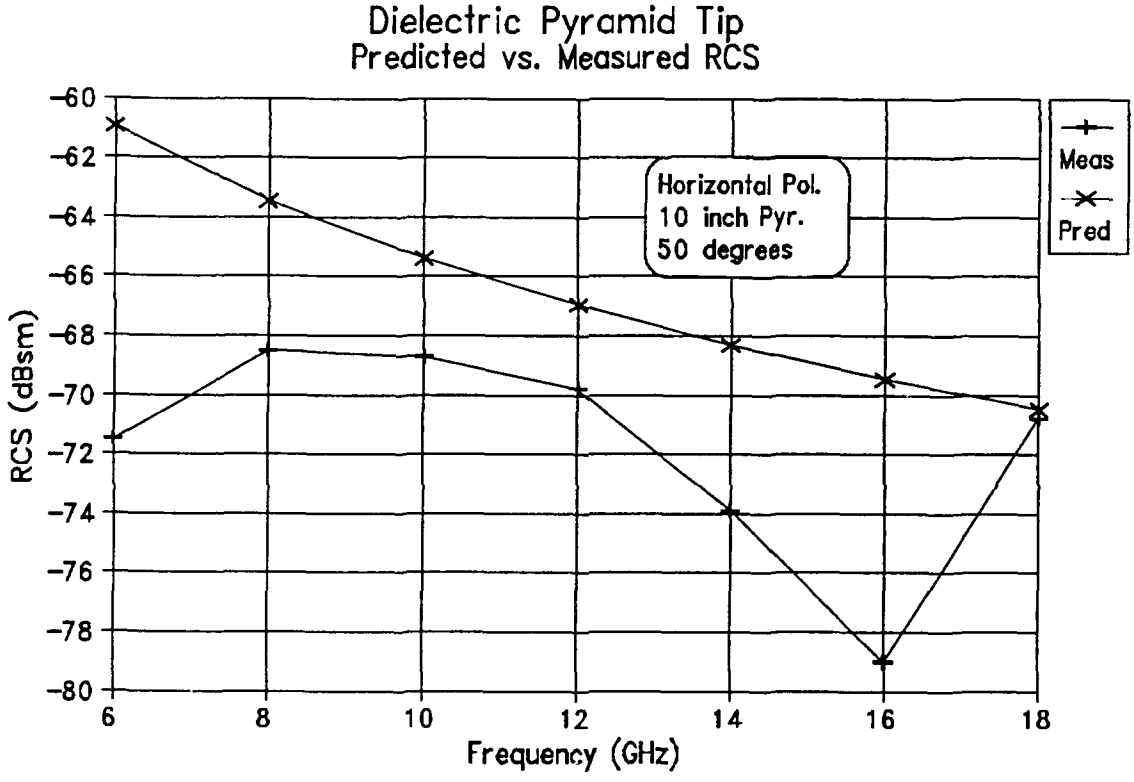

Figure 48. Predicted and Measured Frequency Response for a 10-inch Poly Pyramid at 50 Degrees Azimuth (HH Pol.).

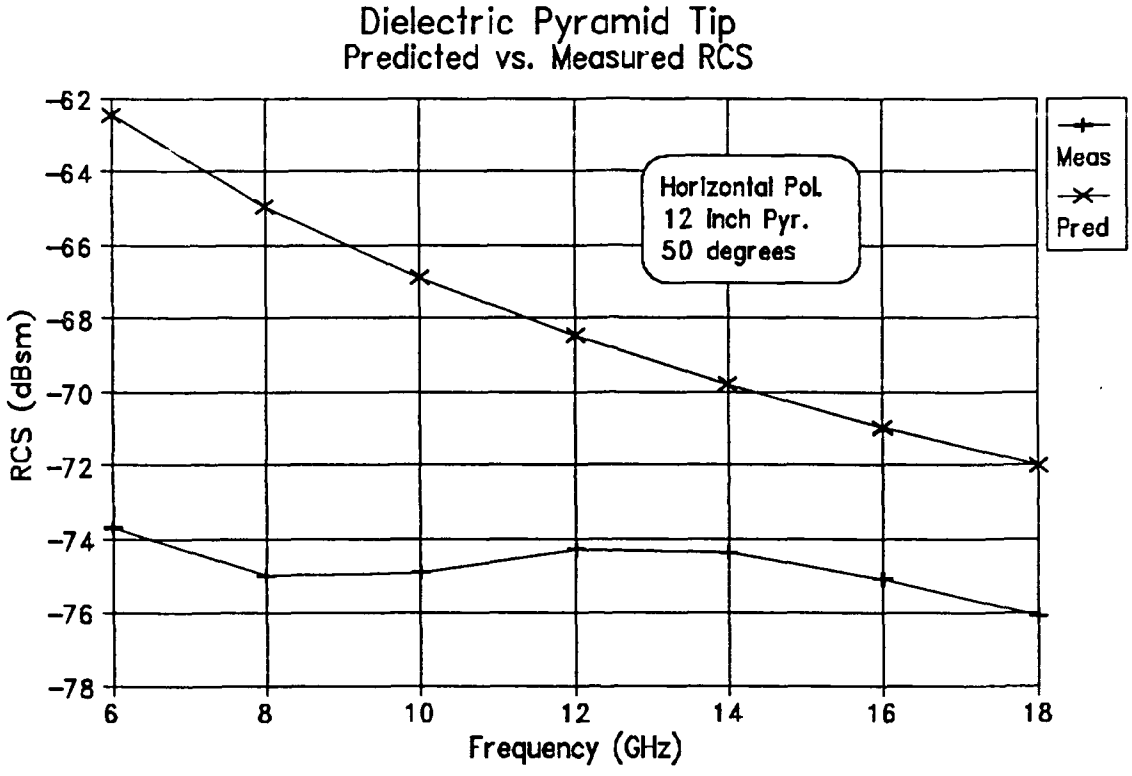

Figure 49. Predicted and Measured Frequency Response for a 12-inch Poly Pyramid at 50 Degrees Azimuth (HH Pol.).

signal level and tracking; medium size (8-inch and 10-inch) pyramids show moderately close agreement in signal level and tracking; and large (12-inch) pyramids display poor agreement in both signal level and tracking.

Figure 50 through Figure 52 show the typical vertical polarization frequency response of dielectric pyramids in the near nose-on region azimuth region. This response is similar to the horizontally polarized dielectric pyramid tip frequency response in the greater azimuth region. Figure 50 shows the predicted and measured frequency response of the 6-inch pyramid tip at 5 degrees azimuth. This figure shows nominal (3 decibels) agreement in signal level and excellent tracking between prediction and measurement. The 10-inch dielectric pyramid tip (Figure 51) shows degraded signal level agreement and degraded tracking compared to the 6-inch pyramid. Figure 52 shows the poor signal level agreement and tracking between the predicted and measured frequency response. This pattern of degraded agreement between measurement and prediction as the pyramid height increases (pyramid tip angle decreases) is typical of the vertically polarized frequency response of dielectric pyramid tips in the near nose-on azimuth region.

Figure 53 shows the vertical polarization frequency response of the 8-inch dielectric pyramid tip at 50 degrees azimuth. Typical of the response in the greater azimuth (20 to 50 degrees) region is that the measured frequency

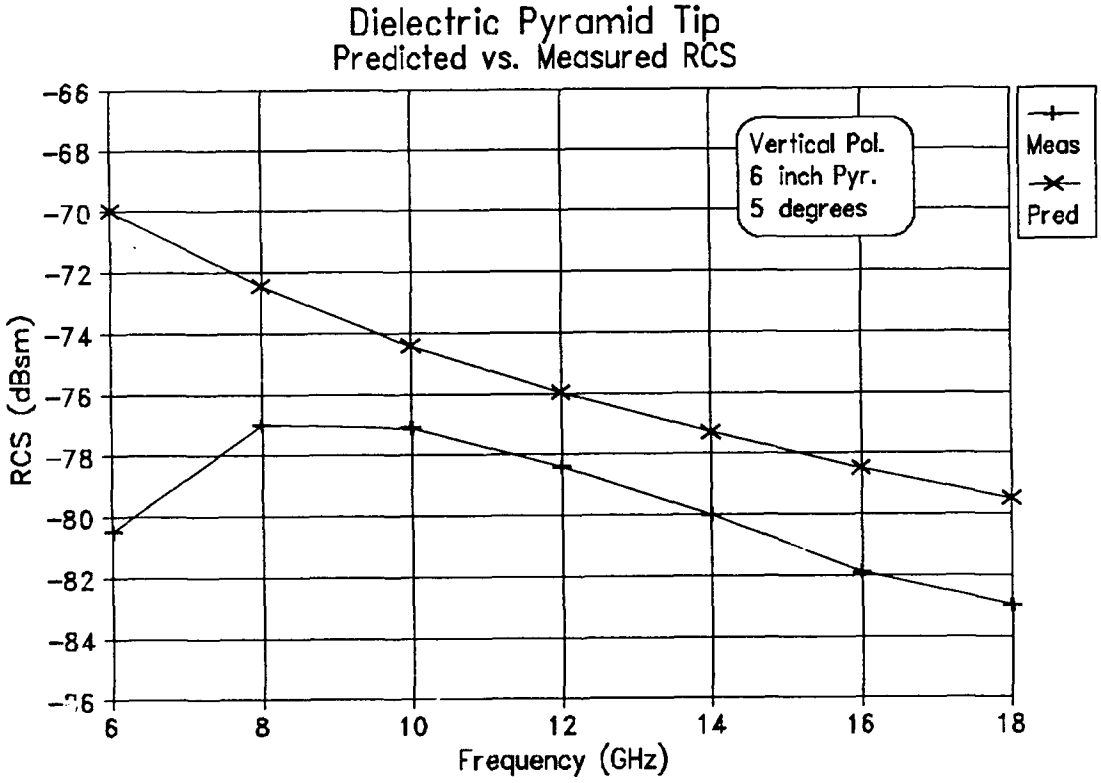

Figure 50. Predicted and Measured Frequency Response for a 6-inch Poly Pyramid at 5 Degrees Azimuth (VV Pol.).

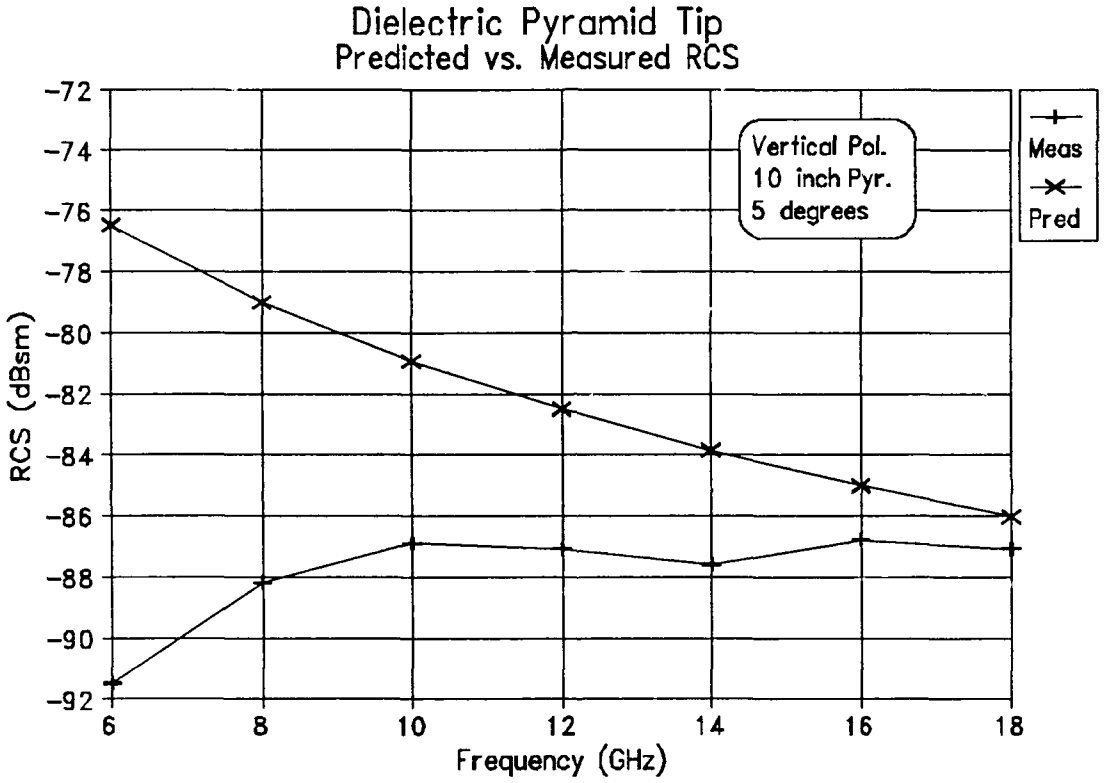

Figure 51. Predicted and Measured Frequency Response for a 10-inch Poly Pyramid at 5 Degrees Azimuth (VV Pol.).

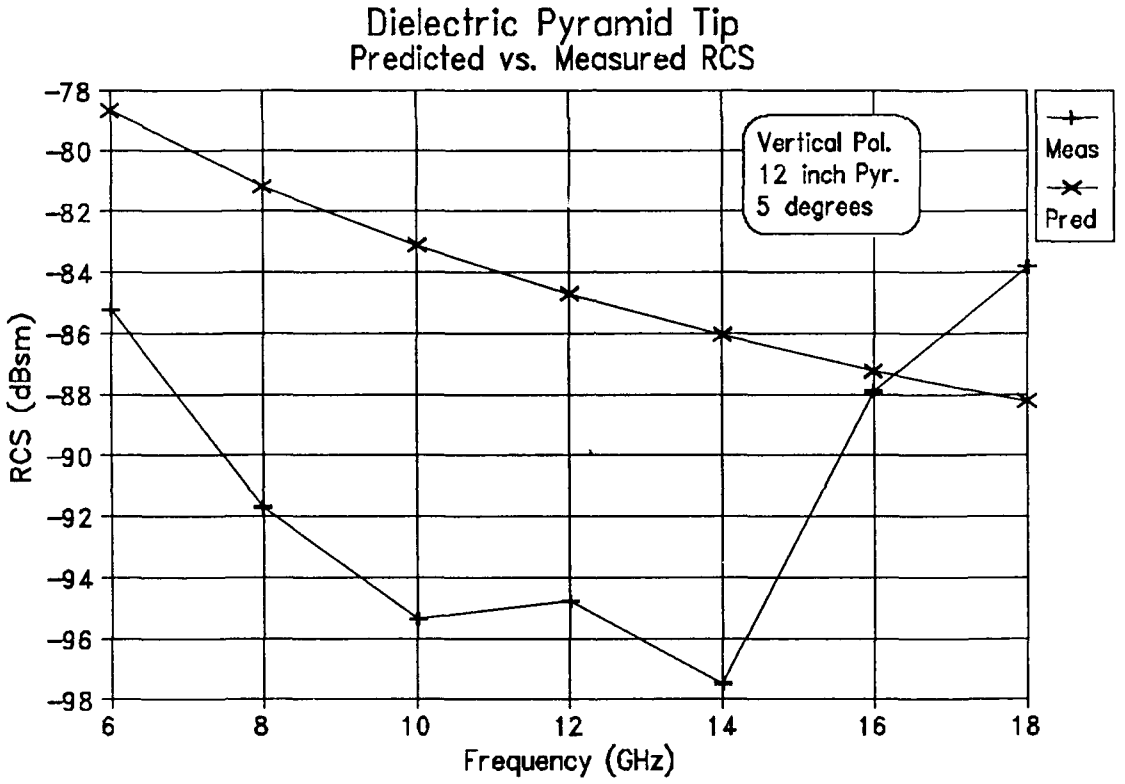

Figure 52. Predicted and Measured Frequency Response for a 12-inch Poly Pyramid at 5 Degrees Azimuth (VV Pol.).

response tracks the prediction fairly well. The agreement between predicted and measured signal levels, however, is very poor. This is shown in Figure 53 in which the measured frequency response is 7 decibels below the prediction. The measured and predicted signal levels continue to diverge as pyramid height increases. Figure 54 shows the predicted and measured vertically polarized frequency response for a 12-inch pyramid in the greater azimuth range. It can be seen in this figure that the measurement generally tracks the prediction well, but with a measured signal level 15 to 18 decibels below the prediction, tracking is insignificant.

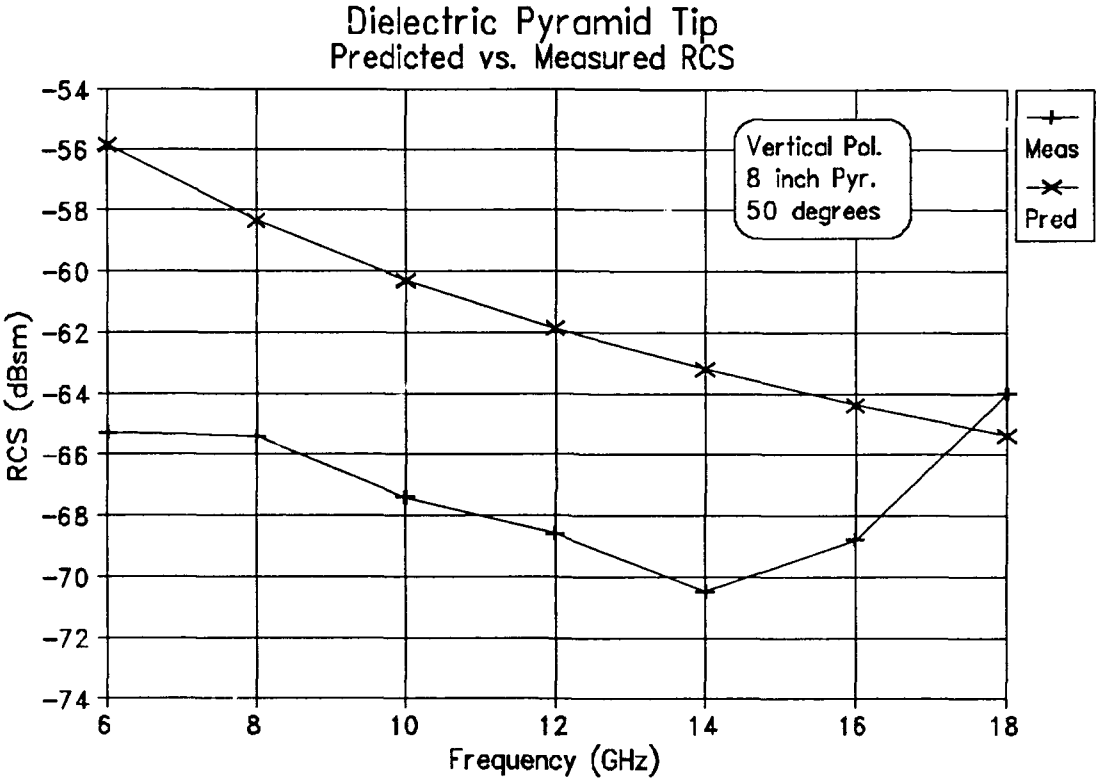

Figure 53. Predicted and Measured Frequency Response for an 8-inch Poly Pyramid at 50 Degrees Azimuth (VV Pol.).

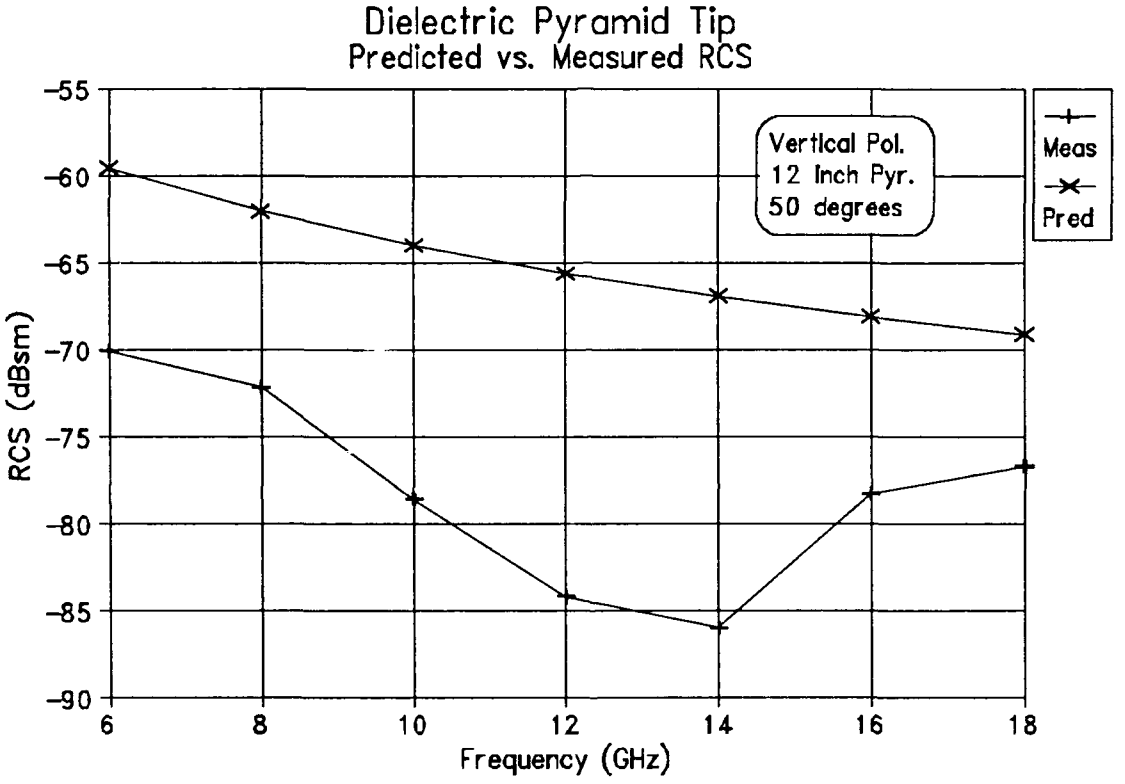

Figure 54. Predicted and Measured Frequency Response for a 12-inch Poly Pyramid at 50 Degrees Azimuth (VV Pol.).

4.4 Lossy Dielectric (Absorber) Pyramid

Recall from Chapter III that either end of the absorber target consists of four pyramid tips mounted co-planar to the incident wavefront. Based on the positions of these tips, a calibration factor is applied to the measured backscatter for the target. This calibrated target backscatter must then be reduced (by 12 decibels) to obtain the calibrated backscatter for a single absorber pyramid tip. Unless specifically indicated otherwise, all data in this section is for a single tip.

Figure 55 shows the measured and predicted horizontally polarized frequency response of an absorber pyramid tip at nose-on incidence. Two features of this graph are significant. The first feature is the measured scattering level. Over the center frequency band (10 Ghz to 14 Ghz), the measurement somewhat exceeds the prediction. For both the conducting pyramids (Figure 27) and Poly pyramids (Figure 45 and Figure 46) the prediction exceeds the measurement. The second feature of Figure 55 is that the frequency response peaks around 14 Ghz. As the figure shows, the prediction declines monotonically. A time gate applied to an ideal response would result in roll-off at the frequency extremes; the result would be a peak frequency response at a frequency below 12 Ghz. Roll-off is clearly evident in the measured response, but the peak frequency response is at a frequency above 12 Ghz.

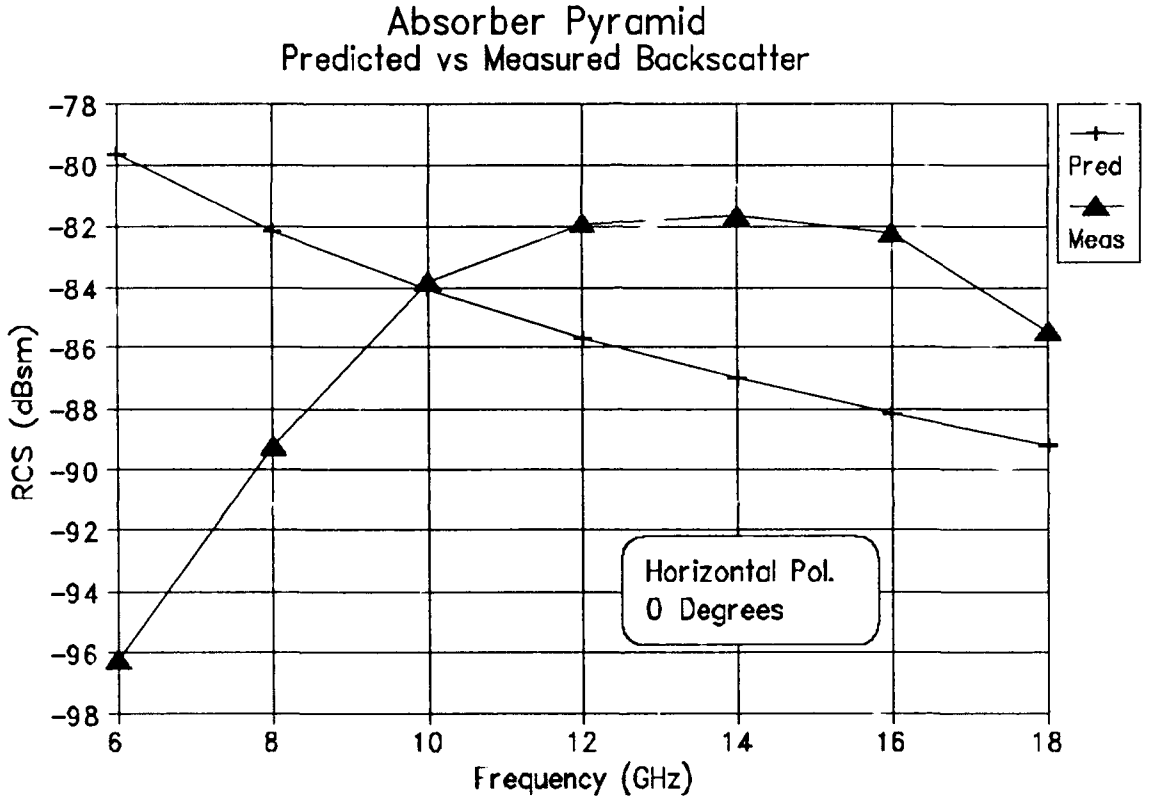

Figure 55. Predicted and Measured Frequency Response for an Absorber Pyramid Tip at Nose-on Incidence (HH Pol.).

Figure 56 shows the measured and predicted horizontally polarized frequency response of an absorber pyramid tip at 40 degrees azimuth. The measured frequency response nearly perfectly matches the predicted response. This measurement and prediction correlation compares favorably with that of a conducting pyramid (Figure 28) or a Poly pyramid (Figure 47) at higher azimuth under horizontal polarization. Clearly, the prediction works well for this orientation.

Figure 57 shows the measured and predicted vertically polarized frequency response of an absorber pyramid tip at nose-on incidence. As in the horizontally polarized absorber case (Figure 55), the peak frequency response occurs at a frequency above 12 Ghz. However, the signal levels are significantly lower than those in Figure 55; over the center frequency range from 10 Ghz to 14 Ghz the average frequency response under vertical polarization is over 7 decibels less than the horizontally polarized case. In Figure 57, the difference between the measurement and prediction steadily decreases as frequency increases, which is not unlike the response of a similar shape (10-inch) Poly pyramid at near nose-on incidence under vertical polarization (Figure 51).

Figure 58 shows the measured and predicted vertically polarized frequency response of the absorber pyramid tips at 40 degrees azimuth. This response shows very good agreement in the center frequency range from 10 Ghz to 14 Ghz: the

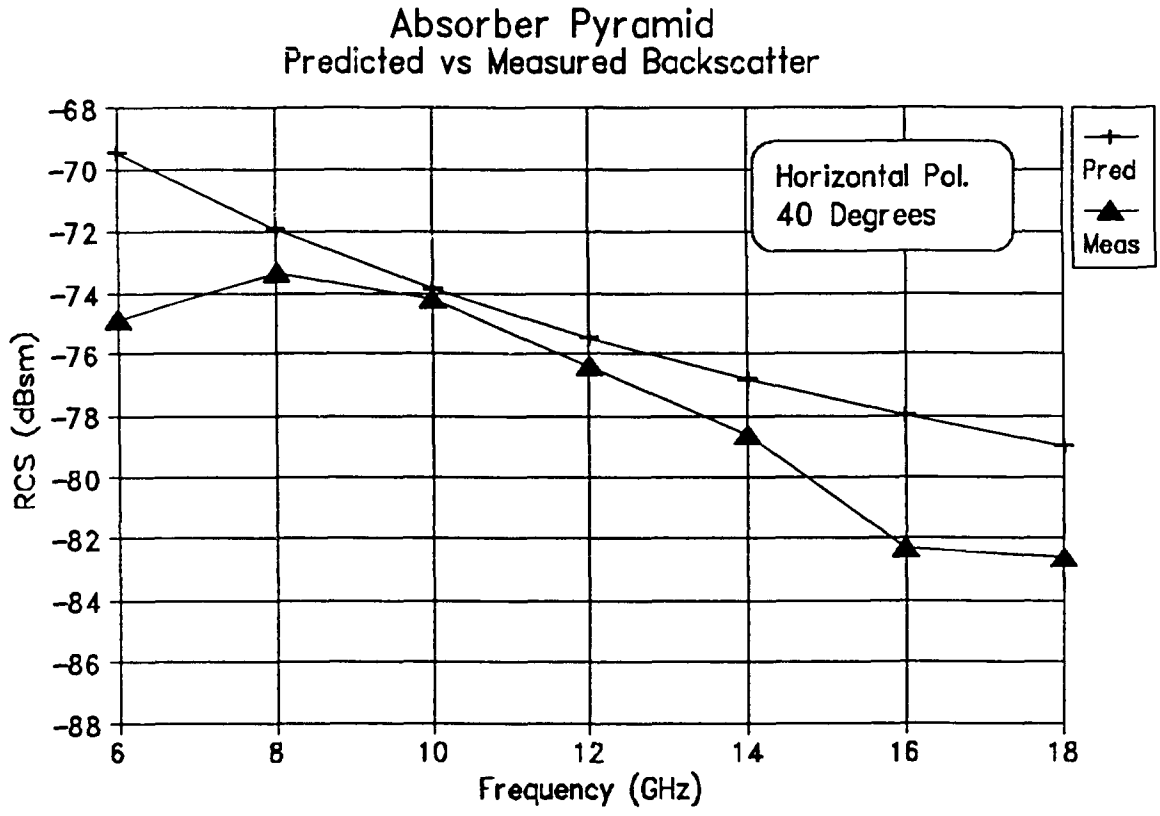

Figure 56. Predicted and Measured Frequency Response for an Absorber Pyramid Tip at 40 Degrees Azimuth (HH Pol.).

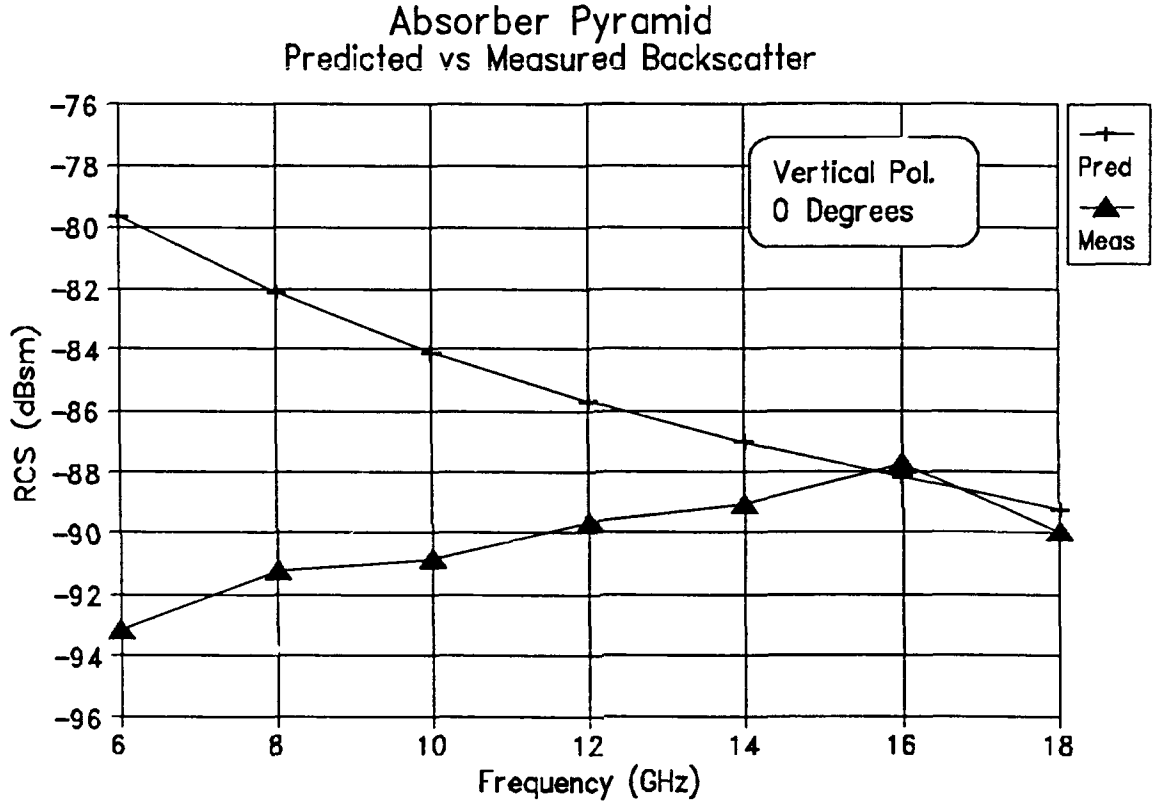

Figure 57. Predicted and Measured Frequency Response for an Absorber Pyramid Tip at Nose-on Incidence (VV Pol.).

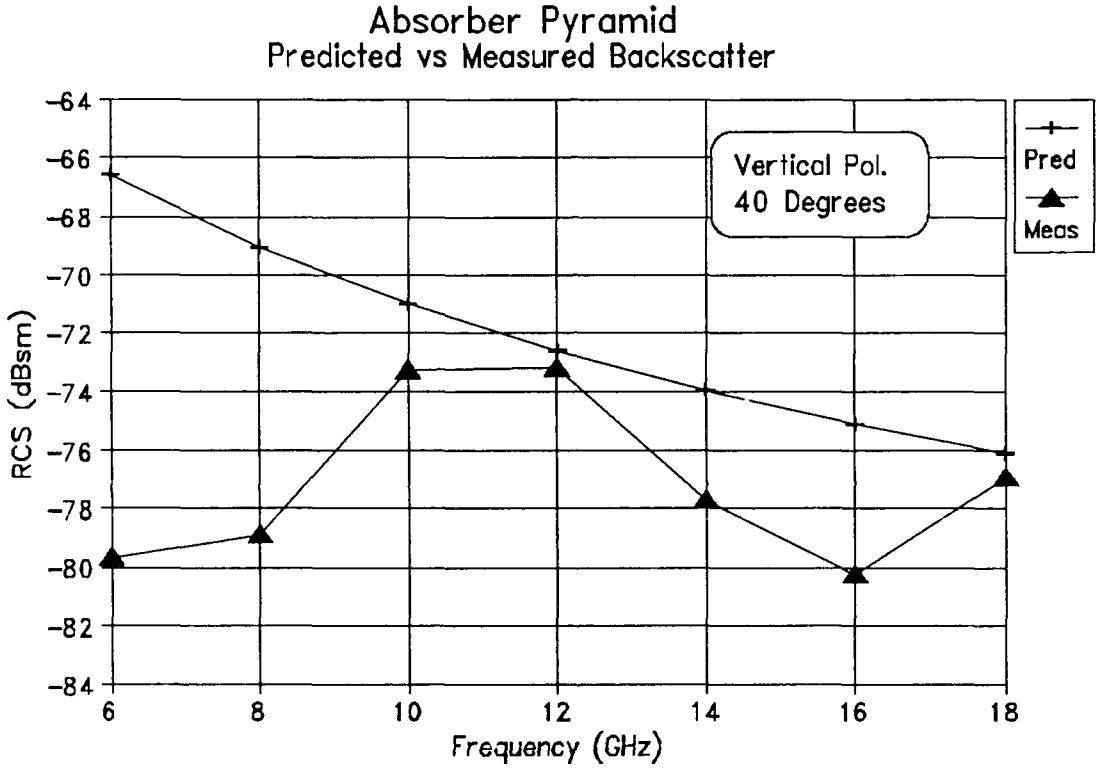

Figure 58. Predicted and Measured Frequency Response for an Absorber Pyramid Tip at 40 Degrees Azimuth (VV Pol.).

average difference is under 2 decibels over this range, and the agreement is within 1 decibel at the center frequency (12 Ghz). While the agreement is not as good as that of the horizontally polarized case (Figure 56), this result is extremely gratifying given the approximate nature of the corner diffraction solution.

The agreement patterns between measurement and prediction for the conducting and Poly pyramid tips do not hold when applied to absorber pyramid tips. In the nose-on region the measured frequency response patterns are quite different from the predicted frequency response patterns. The nominal accuracy achieved in the nose-on region for both conducting and Poly pyramid tips under both horizontal and vertical polarizations validated the geometrical and material assumptions of the approximate solution (in the nose-on region). Apparently some other scattering dominates in this region for the absorber pyramids. Figure 59 shows the time domain responses of the 10-inch Poly test body (top) and the absorber test body (bottom) at nose-on incidence. The time domain response of the Poly test body shows a tip response around -3.37 nanoseconds and then quiet for over a nanosecond until the next scattering center (the pyramid base) appears. The time domain response of the absorber test body shows the tip return around -3.5 nanoseconds, but no quiet zone. This figure clearly shows the scattering from inhomogeneities in the absorber. The

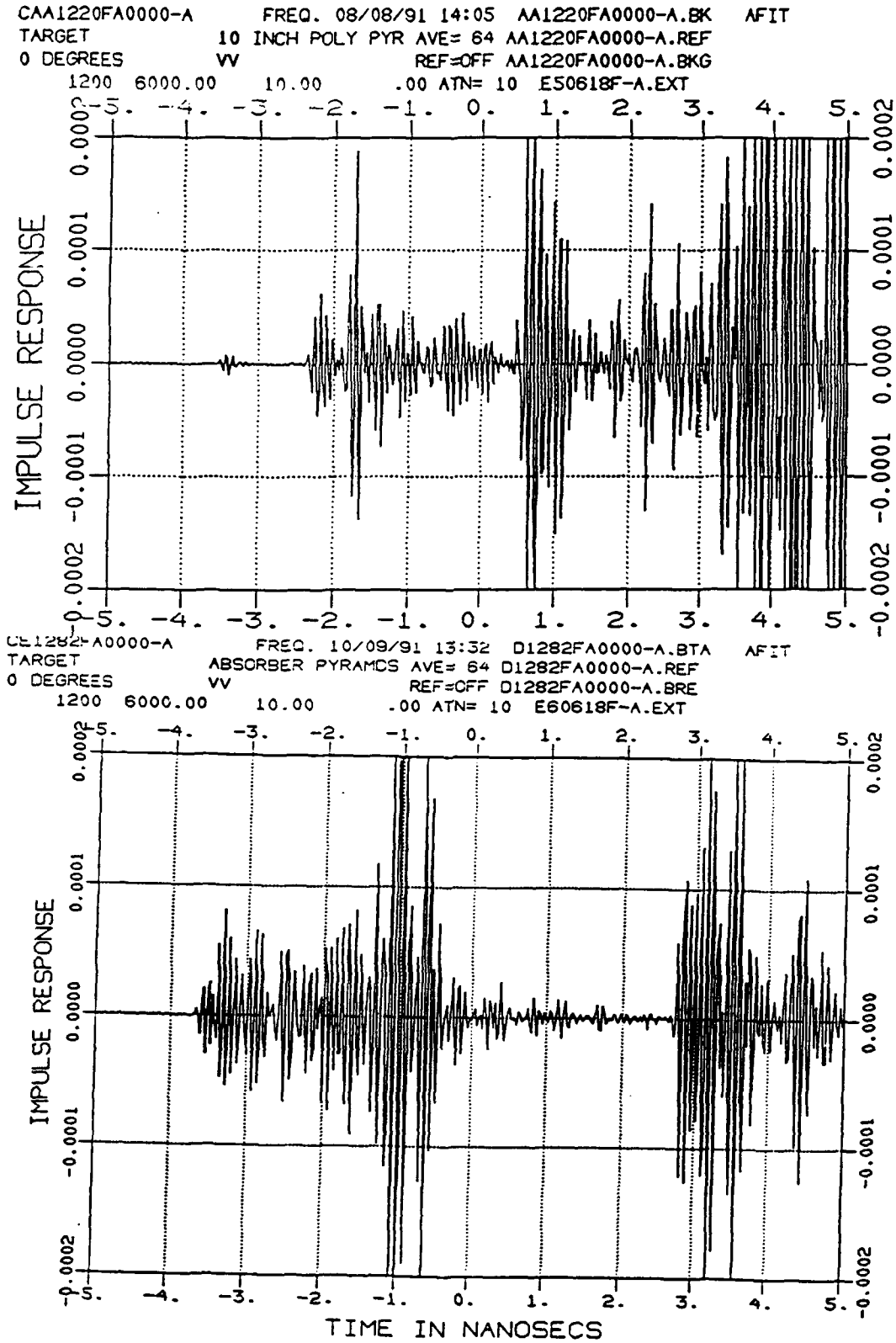

Figure 59. Time Domain Responses of 10-inch Poly Test Body and Absorber Test Body at Nose-on Azimuth (VV Pol.).

level of the scattering from inhomogeneities is nearly double that of the tip scattering, and the level of scattering is sustained (no quiet zone) for the entire length of the absorber pyramid. Combined with the fact that the predicted tip backscatter is least at nose-on incidence, the scattering from inhomogeneities is able to dominate in this region.

Next consider the pyramid at a 40 degree azimuth angle. The dielectric corner solution predicts the tip scattering will be increased 10 decibels for horizontally polarized fields (see Figure 55 and Figure 56) or 13 decibels for vertically polarized fields (see Figure 57 and Figure 58). If we assume that the inhomogeneities in the absorber are randomly distributed, then the level of scattering will remain essentially unchanged as the aspect angle varies. (Actually, there should be *some* change as the bulk of the material is shifted in orientation, but this effect is trivial compared to the order-of-magnitude changes in the predicted tip scattering.) Figure 60 shows that, at 40 degree azimuth incidence, the scattering by the pyramid tip is on an order with the scattering by the absorber inhomogeneities and the two sources of scattering are easily isolated from each other. This explains the poor performance of the absorber predictions in the nose-on regions and the fairly good agreement for the 40 degree measurements.

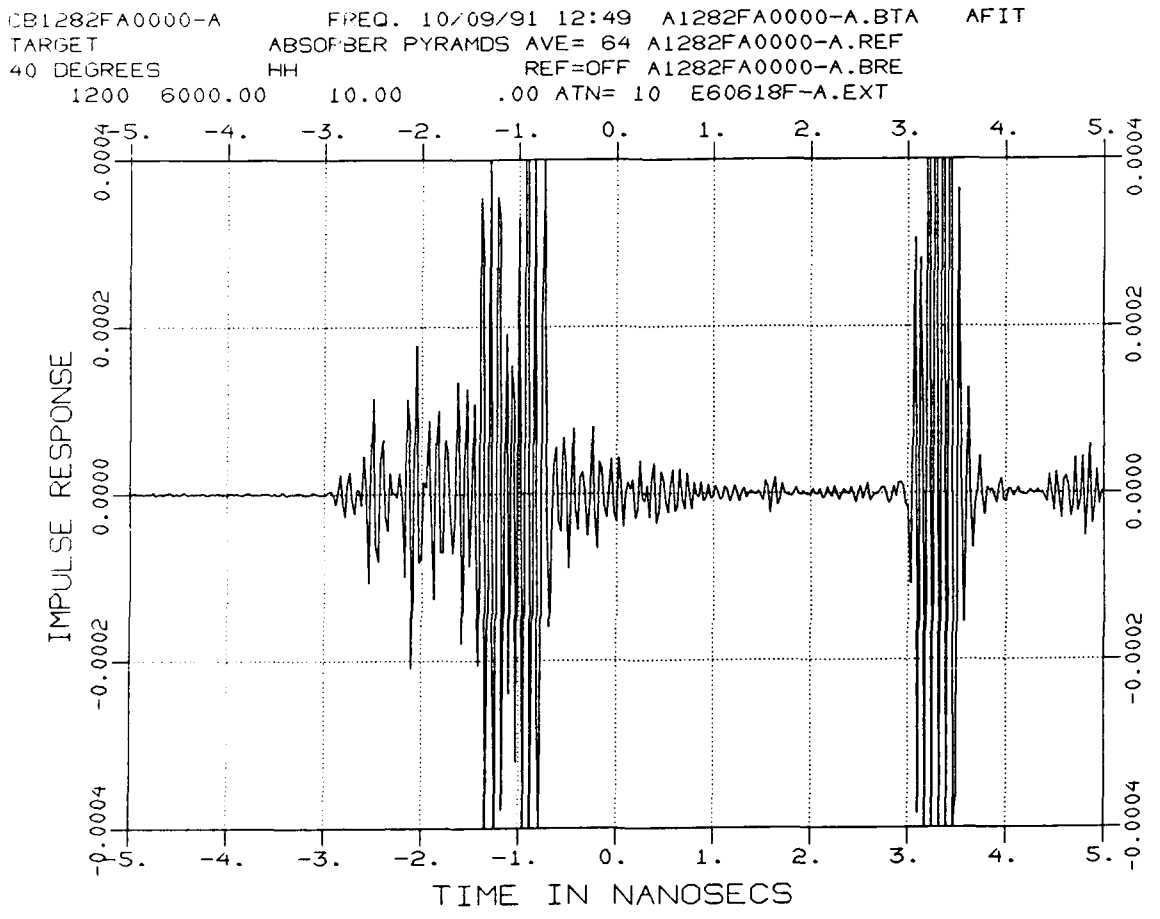

Figure 60. Time Domain Response of Absorber Test Body at 40 Degrees Azimuth (HH Pol.).

4.5 Conclusions

A number of conclusions concerning the applicability and validity of the approximate dielectric corner diffraction solution are reached as a result of this study.

The accuracy of the corner diffraction solution is dependent on the polarization of the incident field on the corner. It was discovered that the solution was much more accurate for a horizontally polarized electric field than for a vertically polarized field. In particular, as a pyramid tip rotated in the horizontal plane away from nose-on aspect, the prediction for horizontal polarization became more accurate and the prediction for vertical polarization became less accurate.

The accuracy of the approximate corner diffraction solution depends on the direction of the incident field. There are two distinct regions which determine the accuracy of the corner diffraction solution for a pyramid. Within a cone of 20 to 25 degrees half-angle around the nose-on direction, the solution gives a nominally correct prediction. This prediction will typically be within 3 to 5 decibels above the measured scattering levels for either polarization. Outside of the 'nose-on cone,' the solution becomes more or less accurate, depending on the polarization of the incident field (see preceding paragraph).

The accuracy of the corner diffraction solution when applied to a dielectric is primarily a function of the acuteness of the corner angles. For the broadest angle measured (35 degrees between adjacent edges), the solution was reasonably accurate. As the angle between adjacent edges decreased, the solution became less and less accurate. This dependence on angle is not apparent for conducting corners. The effect of corner angle is less pronounced for fields incident within the 'nose-on cone.'

The approximate dielectric corner solution is not well suited for prediction of backscatter from absorber materials in the nose-on region. It is apparent that scattering from internal inhomogeneities is the dominant scatterer around nose-on incidence. Time domain plots show that scattering from internal sources in typical pyramidal material at nose-on incidence is at a level approximately double that of tip scattering. Moreover, the higher level of scattering is maintained over the entire volume of the absorber. At incidences away from nose-on, the dielectric corner solution is fairly accurate.

V. Summary

The purpose of this study was to determine the validity and applicability of Joseph's [2] approximate UTD dielectric corner diffraction solution and to study the scattering by absorber pyramids. Towards this end the necessary theory for the use of a prediction code was presented, procedures for obtaining experimental data were developed, and this data was compared and contrasted with predictions.

The results of this study showed that the approximate solution worked nominally well for both conducting pyramids and lossless dielectric pyramids when the incident field was within a 25 degree cone about the nose-on direction. Outside of that cone the accuracy of the solution depended on the polarization of the incident field and the incidence aspect on the pyramid. It was found that the solution worked fairly well for predicting the relative frequency response of a conducting corner.

The angles between adjacent edges play a critical role in determining the accuracy of the solution for lossless dielectric corners. Very sharp lossless dielectric corners give extremely poor predictions. Broader angles give fairly accurate predictions depending on the incident field polarization and incident direction as was determined for conducting pyramids. Fields incident in the nose-on region are less affected by the acuteness of the corner angles.

Application of the corner diffraction solution to lossy dielectric (absorber) pyramid tips showed that scattering from internal inhomogeneities is the dominant mechanism for aspect angles around nose-on incidence. At incidences away from nose-on, the level of tip scattering increases significantly and becomes the dominant scatterer.

There are a number of situations where the approximate solution may be used with fair to excellent accuracy. However, the UTD dielectric corner diffraction solution is an approximate solution. It is well suited for order of magnitude engineering predictions on conducting and lossless and lossy homogeneous dielectric corners.

Bibliography

1. DeWitt, B. T. Analysis and Measurement of Electromagnetic Scattering by Pyramidal and Wedge Absorber. PhD Dissertation. The Ohio State University, Columbus, OH, 1986.

2. Joseph, Philip J. A UTD Scattering Analysis of Pyramidal Absorber for Design of Compact Range Chambers. PhD Dissertation, AFIT/CI/NR 88-193. The Ohio State University, Columbus, OH, 1988.

3. Joseph, Philip J., R. J. Mariano, W. D. Burnside and I. J. Gupta. "Analysis of Absorber Scattering in Compact Range Measurement Systems," Proceedings of the Twelfth Annual AMTA Symposium (Oct 1990).

4. Brumley, Stephen A. Evaluation of Microwave Anechoic Chamber Absorbing Materials. MS Thesis. Arizona State University, Tempe, AZ, 1988 (AD-A198055).

5. DeWitt, Brian T. and Walter D. Burnside. "Electromagnetic Scattering by Pyramidal and Wedge Absorber," IEEE Transactions on Antennas and Propagation, AP-36: 971-984 (July 1988).

6. Kouyoumjian, Robert G., and Prabhakar H. Pathak. "A Uniform Geometrical Theory of Diffraction for an Edge in a Perfectly Conducting Surface," Proceedings of the IEEE, 62: 1448-1461 (November 1974).

7. Sikta, Fathi A., et al. "First-Order Equivalent Current and Corner Diffraction Scattering from Flat Plate Structures," IEEE Transactions on Antennas and Propagation, AP-31: 584-589 (July 1983).

8. Burnside, W. D., N. Wang and E. L. Pelton. "Near-Field Pattern Analysis of Airborne Antennas," IEEE Transactions on Antennas and Propagation, AP-28: 318-327 (May 1983).

9. Burnside, W. D. and K. W. Burgener. "High Frequency Scattering by a Thin Lossless Dielectric Slab," IEEE Transactions on Antennas and Propagation, AP-31: 584-589 (January 1983).

December 1991 Master's Thesis

Electromagnetic Scattering from Dielectric Pyramidal Tips

Albert D. Tyson, IV, Captain, USAF

Air Force Institute of Technology
WPAFB, OH 45433-6583

AFIT/GE/ENG/91D-56

Approved for public release; distribution unlimited

This thesis investigated the electromagnetic scattering from conducting, lossless dielectric, and lossy dielectric (absorber) pyramids. The backscatter from pyramids was measured and a time gate was applied to isolate the scattering from the tips. The measured results were compared to predictions from an approximate Uniform Theory of Diffraction (UTD) solution for scattering by a dielectric corner. The accuracy of the corner diffraction solution was found to be dependent on the polarization of the incident electric field. The accuracy of the UTD solution was also dependent on the aspect angle to the pyramid: the UTD solution gave a nominally correct answer within 25 degrees of nose-on incidence; at other angles the accuracy was better or worse depending on field polarization. The accuracy of the corner diffraction solution when applied to a dielectric was primarily dependent on the tip angle of the pyramid, with more acute angles giving the least accurate results. At incidence angles near nose-on to absorber pyramids, scattering from internal inhomogeneities was the dominant scattering mechanism. At incidence angles away from nose-on, the UTD solution provided reasonably accurate results. The approximate UTD dielectric corner solution was found to be accurate for many engineering applications.

Electromagnetic Scattering, Diffraction, Uniform Theory of Diffraction (UTD), Pyramids, Absorbers (Materials), Dielectrics, Geometry

15. NUMBER OF PAGES: 120

16. PRICE CODE

17. SECURITY CLASSIFICATION OF REPORT	18. SECURITY CLASSIFICATION OF THIS PAGE	19. SECURITY CLASSIFICATION OF ABSTRACT	20. LIMITATION OF ABSTRACT
Unclassified	Unclassified	Unclassified	UL

Standard Form 298

GENERAL INSTRUCTIONS FOR COMPLETING SF 298

The Report Documentation Page (RDP) is used in announcing and cataloging reports. It is important that this information be consistent with the rest of the report, particularly the cover and title page. Instructions for filling in each block of the form follow. It is important to **stay within the lines to meet optical scanning requirements.**

Block 1. Agency Use Only (Leave Blank)

Block 2. Report Date. Full publication date including day, month, and year, if available (e.g. 1 Jan 88). Must cite at least the year.

Block 3. Type of Report and Dates Covered. State whether report is interim, final, etc. If applicable, enter inclusive report dates (e.g. 10 Jun 87 - 30 Jun 88).

Block 4. Title and Subtitle. A title is taken from the part of the report that provides the most meaningful and complete information. When a report is prepared in more than one volume, repeat the primary title, add volume number, and include subtitle for the specific volume. On classified documents enter the title classification in parentheses.

Block 5. Funding Numbers. To include contract and grant numbers; may include program element number(s), project number(s), task number(s), and work unit number(s). Use the following labels:

C	- Contract	**PR**	- Project
G	- Grant	**TA**	- Task
PE	- Program Element	**WU**	- Work Unit Accession No.

Block 6. Author(s). Name(s) of person(s) responsible for writing the report, performing the research, or credited with the content of the report. If editor or compiler, this should follow the name(s).

Block 7. Performing Organization Name(s) and Address(es). Self-explanatory.

Block 8. Performing Organization Report Number. Enter the unique alphanumeric report number(s) assigned by the organization performing the report.

Block 9. Sponsoring/Monitoring Agency Names(s) and Address(es). Self-explanatory.

Block 10. Sponsoring/Monitoring Agency. Report Number. (If known)

Block 11. Supplementary Notes. Enter information not included elsewhere such as: Prepared in cooperation with...; Trans. of ..., To be published in .... When a report is revised, include a statement whether the new report supersedes or supplements the older report.

Block 12a. Distribution/Availablity Statement. Denote public availability or limitation. Cite any availability to the public. Enter additional limitations or special markings in all capitals (e.g. NOFORN, REL, ITAR)

DOD - See DoDD 5230.24, "Distribution Statements on Technical Documents."
DOE - See authorities
NASA - See Handbook NHB 2200.2.
NTIS - Leave blank.

Block 12b. Distribution Code.

DOD - DOD - Leave blank
DOE - DOE - Enter DOE distribution categories from the Standard Distribution for Unclassified Scientific and Technical Reports
NASA - NASA - Leave blank
NTIS - NTIS - Leave blank.

Block 13. Abstract. Include a brief (Maximum 200 words) factual summary of the most significant information contained in the report.

Block 14. Subject Terms. Keywords or phrases identifying major subjects in the report.

Block 15. Number of Pages. Enter the total number of pages.

Block 16. Price Code. Enter appropriate price code (NTIS only).

Blocks 17. - 19. Security Classifications. Self-explanatory. Enter U.S. Security Classification in accordance with U.S. Security Regulations (i.e., UNCLASSIFIED). If form contains classified information, stamp classification on the top and bottom of the page.

Block 20. Limitation of Abstract. This block must be completed to assign a limitation to the abstract. Enter either UL (unlimited) or SAR (same as report). An entry in this block is necessary if the abstract is to be limited. If blank, the abstract is assumed to be unlimited.